

AD-A273 400

NPS-MR-93-003



2

# NAVAL POSTGRADUATE SCHOOL Monterey, California

**S** DTIC  
ELECTE  
NOV 29 1993  
**A**



Observed and Navy Operational Global Model  
Climatologies of Synoptic Disturbances over the  
Tropical Western Pacific during Winter 1991-92

C.-P. Chang  
*Department of Meteorology, Naval Postgraduate School*

Liana Zambresky  
*Fleet Numerical Oceanography Center*

October 1993

Approved for Public Release; Distribution Unlimited

93-29107



11/96

93 11 26 1 37

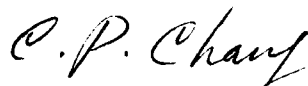
Naval Postgraduate School  
Monterey, California 93943-5000

Rear Admiral T. A. Mercer  
Superintendent

H. Shull  
Provost

This report is the result of a cooperative study between the Department of Meteorology, Naval Postgraduate School, and the Fleet Numerical Oceanography Center. The work at NPS was funded in part by the Naval Research Laboratory, Marine Meteorology Division and by the National Science Foundation, Division of Atmospheric Sciences.

Reproduction of all or part of the report is authorized.



---

C.-P. Chang  
Professor of Meteorology

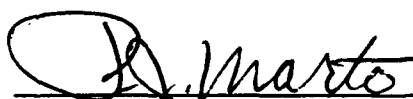
Reviewed by:

Released by:



---

Robert L. Haney, Chairman  
Department of Meteorology



---

Paul J. Marto,  
Dean of Research

UNCLASSIFIED

SECURITY CLASSIFICATION OF THIS PAGE

REPORT DOCUMENTATION PAGE				Form Approved OMB No 0704 0188	
1a REPORT SECURITY CLASSIFICATION <b>UNCLASSIFIED</b>			1b RESTRICTIVE MARKINGS		
7a SECURITY CLASSIFICATION AUTHORITY			3 DISTRIBUTION/AVAILABILITY OF REPORT Approved for public release; distribution unlimited		
2b DECLASSIFICATION/DOWNGRADING SCHEDULE			5 MONITORING ORGANIZATION REPORT NUMBER(S)		
4 PERFORMING ORGANIZATION REPORT NUMBER(S) NPS-MR-93-003			7a NAME OF MONITORING ORGANIZATION		
6a. NAME OF PERFORMING ORGANIZATION Naval Postgraduate School		6b OFFICE SYMBOL (If applicable) MR	7b ADDRESS (City, State, and ZIP Code)		
6c. ADDRESS (City, State, and ZIP Code) Monterey, CA 93943-5000			9. PROCUREMENT INSTRUMENT IDENTIFICATION NUMBER		
8a. NAME OF FUNDING/SPONSORING ORGANIZATION		8b OFFICE SYMBOL (If applicable)	10 SOURCE OF FUNDING NUMBERS		
8c. ADDRESS (City, State, and ZIP Code)			PROGRAM ELEMENT NO	PROJECT NO	TASK NO
					WORK UNIT ACCESSION NO
11. TITLE (Include Security Classification) Observed and Navy Operational Global Model Climatologies of Synoptic Disturbances over the Tropical Western Pacific during Winter 1991-92					
12. PERSONAL AUTHOR(S) C.-P. Chang and Liana Zambresky					
13a. TYPE OF REPORT Final		13b TIME COVERED FROM 10/92 to 10/93	14. DATE OF REPORT (Year, Month, Day) 9310		15 PAGE COUNT 107
16 SUPPLEMENTARY NOTATION The views expressed in this report are those of the authors and do not reflect the official policy or position of the Department of Defense.					
17. COSATI CODES			18. SUBJECT TERMS (Continue on reverse if necessary and identify by block number)		
FIELD	GROUP	SUB-GROUP			
19 ABSTRACT (Continue on reverse if necessary and identify by block number)					
<p>This study compares the structure and characteristics of tropical synoptic timescale wave disturbances over the western Pacific, particularly around the Caroline Islands where six upper air stations are present, as contained in radiosonde observations and the initial analysis (<math>\tau 00</math>) and 48-h forecast (<math>\tau 48</math>) of the Navy Operational Global Atmospheric Prediction System (NOGAPS) during northern winter of 1991-1992. The observed, analyzed and forecast disturbance climatologies are all determined from power spectral and cross-spectral analyses focusing on the synoptic frequency band encompassing three adjacent period points: 4.6-, 5.3- and 6.4-day. The meridional wind at 850 hPa is used as the principal parameter for defining the disturbances.</p>					
(ABSTRACT Continued next page)					
20 DISTRIBUTION/AVAILABILITY OF ABSTRACT <input checked="" type="checkbox"/> UNCLASSIFIED/UNLIMITED <input type="checkbox"/> SAME AS RPT <input type="checkbox"/> DTIC USERS			21. ABSTRACT SECURITY CLASSIFICATION UNCLASSIFIED		
22a NAME OF RESPONSIBLE INDIVIDUAL C.-P. Chang			22b TELEPHONE (Include Area Code) (408) 656-2840		22c OFFICE SYMBOL MR

DD Form 1473, JUN 86

Previous editions are obsolete.

SECURITY CLASSIFICATION OF THIS PAGE

S/N 0102-LF-014-6603

UNCLASSIFIED

## 19. ABSTRACT (Continued)

The power spectra of the NOGAPS  $\tau 00$  analysis agree reasonably closely with the radiosonde observations, but the  $\tau 48$  forecast shows larger differences. Nevertheless, the observed horizontal structure of the disturbances are all well represented in both the analysis and the forecast at all levels. These include the westward propagation, a 850 hPa wavelength near  $33^\circ$  along  $10^\circ\text{N}$  and near  $38^\circ$  along the equator, a 200 hPa wavelength near  $50-60^\circ$ , and a northeast-southwest meridional tilt. In general, the analysis and the forecast produce a higher spatial coherency than that shown from the radiosonde observations.

Over the eastern part of the station network the disturbances show a strong westward tilt with height similar to that observed previously, but at lower levels there is little vertical tilt as compared to a significant eastward tilt with height observed during some previous summers. Over the western part the vertical tilt is eastward throughout the troposphere, which is opposite to that of the previously observed summer structure. These differences are consistent with the seasonal difference in vertical mean-wind shear due to pronounced monsoon changes. The observed zonal variation of the disturbance vertical structure is reproduced by the  $\tau 00$  analysis, but the forecast structure has a weaker vertical organization over areas where a well-organized structure is observed, and a strong organization to the west where it is not observed. It appears that the model's dynamics produces a downstream propagation that results in an artificial wave structure.

The observed warm core in the upper troposphere is similar to previously observed structure during summers and suggests that the disturbances are self-supporting energetically. This structure is reasonably reproduced by the analysis and forecast. On the other hand, the analyzed low-level thermal structure is warm core near the surface, opposite to the previously observed summer structure. The forecast shows a reverse of this structure, from a warm core to a cold core. It is surmised that the model's cumulus and planetary boundary layer parameterizations may be too strong, causing this reverse.

Over the northern tropics, the broad scale velocity potential shows a southward propagation at 850 hPa and a northward propagation at 200 hPa, a pattern consistent with the acceleration of the East Asian local Hadley cell observed previously during monsoon surges. However, the 48-h forecast climatology contains only the 850 hPa propagation.

Based on the study, a scheme to evaluate the model climatology of the disturbances using spectral and cross spectral quantities is proposed

## Table of Contents

Abstract..... 2

1. Introduction..... 4

2. Data and Methodology..... 5

3. Comparison of power spectral characteristics..... 8

4. Zonal structure of the synoptic wave disturbances.....19

5. Meridional structure of the synoptic wave disturbances.27

6. Vertical structure of the synoptic wave disturbances...29

7. Thermal structure of the synoptic wave disturbances....34

8. Velocity potential structure.....39

9. A proposed scheme to evaluate systematic errors in model  
analysis and forecast of tropical disturbances.....42

10. Summary and concluding remarks.....44

Acknowledgments.....49

References.....50

Figure Captions.....53

Figures 1-50.....57-106

Initial Distribution List.....107

**DTIC QUALITY INSPECTED 8**

Accession For	
NTIS CRA&I	<input checked="" type="checkbox"/>
DTIC TAB	<input type="checkbox"/>
Unannounced	<input type="checkbox"/>
Justification .....	
By .....	
Distribution / .....	
Availability Codes	
Dist	Avail and/or Special
A-1	

## Abstract

This study compares the structure and characteristics of tropical synoptic timescale wave disturbances over the western Pacific, particularly around the Caroline Islands where six upper air stations are present, as contained in radiosonde observations and the initial analysis (100) and 48-h forecast (148) of the Navy Operational Global Atmospheric Prediction System (NOGAPS) during northern winter of 1991-1992. The observed, analyzed and forecast disturbance climatologies are all determined from power spectral and cross-spectral analyses focusing on the synoptic frequency band encompassing three adjacent period points: 4.6-, 5.3- and 6.4-day. The meridional wind at 850 hPa is used as the principal parameter for defining the disturbances.

The power spectra of the NOGAPS 100 analysis agree reasonably closely with the radiosonde observations, but the 148 forecast shows larger differences. Nevertheless, the observed horizontal structure of the disturbances are all well represented in both the analysis and the forecast at all levels. These include the westward propagation, a 850 hPa wavelength near  $33^\circ$  along  $10^\circ\text{N}$  and near  $38^\circ$  along the equator, a 200 hPa wavelength near  $50-60^\circ$ , and a northeast-southwest meridional tilt. In general, the analysis and the forecast produce a higher spatial coherency than that shown from the radiosonde observations.

Over the eastern part of the station network the disturbances show a strong westward tilt with height similar to that observed previously, but at lower levels there is little vertical tilt as compared to a significant eastward tilt with height observed during some previous summers. Over the western part the vertical tilt is eastward throughout the troposphere, which is opposite to that of the previously observed summer structure. These differences are consistent with the seasonal difference in

vertical mean-wind shear due to pronounced monsoon changes. The observed zonal variation of the disturbance vertical structure is reproduced by the r00 analysis, but the forecast structure has a weaker vertical organization over areas where a well-organized structure is observed, and a strong organization to the west where it is not observed. It appears that the model's dynamics produces a downstream propagation that results in an artificial wave structure.

The observed warm core in the upper troposphere is similar to previously observed structure during summers and suggests that the disturbances are self-supporting energetically. This structure is reasonably reproduced by the analysis and forecast. On the other hand, the analyzed low-level thermal structure is warm core near the surface, opposite to the previously observed summer structure. The forecast shows a reverse of this structure, from a warm core to a cold core. It is surmised that the model's cumulus and planetary boundary layer parameterizations may be too strong, causing this reverse.

Over the northern tropics, the broad scale velocity potential shows a southward propagation at 850 hPa and a northward propagation at 200 hPa, a pattern consistent with the acceleration of the East Asian local Hadley cell observed previously during monsoon surges. However, the 48-h forecast climatology contains only the 850 hPa propagation.

Based on the study, a scheme to evaluate the model climatology of the disturbances using spectral and cross spectral quantities is proposed.

## 1. Introduction

The analysis and prediction of tropical weather are major problems faced by meteorologists due to several reasons, one of which is the sparse coverage of radiosonde data, especially over tropical oceans. The advances of global NWP models have been very useful in alleviating these problems. To make up for the lack of observations, the four-dimensionally assimilated data from global models have been used extensively for tropical diagnostic studies (e.g., Liebmann and Hendon, 1990; Lau and Lau, 1990; Swett, 1993). The tropical forecasts from the global models have also shown useful skill in predicting day-to-day weather systems (e.g., Reed et al., 1988; Hogan and Rosmond, 1992). Both of these applications of the NWP products are extremely important for Navy operations. In the mean time, it has been recognized by many investigators that tropical analyses and forecasts remain amongst the toughest challenges faced by NWP modelers. It is well known that the difficulties in the tropical data analysis and initialization, and treatment of physical processes such as cumulus convection in the global models, continue to cause large errors in the tropics. For example, in the early 1980's the tropical divergent circulations in all major global operational models were known to be too weak. Recent revisions, while resulting in significant improvements, still contain large errors, with the ECMWF model often having too strong a divergent circulation (Trenberth, 1992).

Many of the error statistics for evaluating tropical analyses and forecasts are done in terms of monthly or seasonal mean motions where the results describe the distribution of errors of mean states. Evaluations of the global model's ability to represent tropical synoptic weather systems have been few and mostly through case studies by operational forecasters. This study is an attempt to evaluate statistically the tropical



synoptic disturbances in the NOGAPS analyses and 48-hour forecasts over the northwestern Pacific. The region of the Caroline Islands was chosen, where several routinely operating radiosonde stations allow an evaluation of the analyses and forecasts against observations. Spectral analysis was used to compare the structures of synoptic disturbances, with periodicity around 5 days, as they are deduced from the observed, analyzed and forecasted data. The period of study is the winter season of 1991-1992.

## 2. Data and Methodology

The data of this study are all retrieved from the FNOG archive and may be classified into three categories:

1) Radiosonde data ("RAOB"): These are reports received real-time through the Global Telecommunication System. They are the same observations that were used operationally in the objective analysis of NOGAPS. Six stations in the Caroline Islands and vicinity are used:

Majuro	7.1°N	171.4°E
Ponape	7.0°N	158.2°E
Truk	7.5°N	151.9°E
Guam	13.6°N	144.8°E
Yap	9.5°N	138.1°E
Koror	7.3°N	134.5°E

(These stations are identified in the first figure on a geographic map - Fig. 27.)

2) Analyzed data ("r00"): The objectively analyzed fields in NOGAPS. The data are on the 2.5° x 2.5° latitude-longitude grid.

3) Forecast data ("rhh"): The NOGAPS forecasted fields at hh hours. For most of the study the 48-h forecast (r48) is used. The data are on the 2.5° x 2.5° latitude-longitude grid.

All data are twice daily, from 12Z 11 November 1991 to 00Z 17 March 1992, a total of 128 days or 256 time points. Missing data are filled by linear interpolation of the nearest values. Time series of radiosonde with coverage less than 80% are not used.

Spectral and cross-spectral analysis are used to determine the characteristics and structure of synoptic timescale fluctuations contained in the data, as well as to compare the NOGAPS analyses and forecasts against radiosonde observations. The spectral analysis is done by partitioning each demeaned and detrended time series into seven ensembles with a cosine taper of 10% applied to each end before fast Fourier transformation. The resultant frequency resolution is 0.03125 cycles/day (32-day period), and the Nyquist frequency is 1 cycle/day. The (32 day)<sup>-1</sup> point is the lowest frequency resolved, and because of the detrending, a spectral peak at this frequency is considered to represent all variances beyond the monthly timescale, to include those of intraseasonal and possibly seasonal oscillations.

The determination of the disturbance structure is similar to the approach used in previous spectral studies on the easterly waves of the tropical western Pacific using radiosonde data (e.g., Wallace and Chang, 1969; Chang et al., 1970a; 1977b). Inspection of all spectral distributions revealed that significant variances often occur at seasonal, intraseasonal, quasi-biweekly and synoptic timescales. Cross-spectral analysis is then used to focus on the synoptic scale oscillations, whose variances are mostly concentrated in a frequency window centered at period 5.3 days. The cross spectra, in terms of coherence

squares and phase differences, of the three adjacent frequencies corresponding to 4.6, 5.3 and 6.4 day periods, are then averaged to represent the cross relationship between various pairs of variables of the synoptic scale. This frequency band will be called the synoptic band or the "5-day" band. The cross spectra are used to infer the horizontal, vertical and the dynamic and thermodynamic structures of the 5-day disturbances.

The degrees of freedom for the 5-day band is estimated to be 42, and the corresponding coherence squared threshold for the 95% significance level is estimated to be 0.14. Phase difference values with coherence squared above 0.14 will be considered significant and are used for inferring the disturbance structure. (When an individual frequency is considered, the degrees of freedom is about 14 and the 95% significance level is at coherence square  $\geq 0.43$ .)

The meridional wind oscillations are generally a better indicator of tropical synoptic-scale disturbance activities except at the equator. This is because, for the duration of a synoptic time period, the tropical winds are normally dominated by the zonal component with a high constancy, and the meridional wind tends to oscillate around a very small time mean. Based on previous spectral studies of westward propagating synoptic disturbances in the tropical western Pacific using radiosonde data, the meridional velocity at 850 hPa ( $v_{850}$ ) is used as the most important variable in detecting the synoptic disturbances. 850 hPa is the level where the structure of these disturbances has been found to be most clearly defined, and it is also the level of maximum data coverage in the lower troposphere because of the existence of many pilot balloon observations and cloud base satellite winds. In many cases  $v_{850}$  is used as the base time series to cross with other series in order to determine the structure of disturbances. In the upper troposphere, the meridional velocity at 200 hPa, where maximum amount of

upper-level satellite cloud winds and commercial aircraft wind data are located, is considered the base series.

The area of study covers the entire tropical western Pacific. All horizontal maps cover the region from 100°E-180°E and 10°S-30°N. Because of the wide longitudinal span of the region, the term "central-western Pacific" will occasionally be used to refer to the eastern half of the diagram (140°E-180°E). While the main focus of the study is the synoptic westward propagating disturbances in this region, the South China Sea is included in the diagrams because of its importance in the winter monsoon cold surge events that are known to dominate the synoptic scale fluctuations in the lower troposphere over the western Pacific. For brevity, the term "easterly waves," where "easterly" refers to propagation from the east, may be used occasionally to refer to the tropical westward propagating synoptic disturbances.

### 3. Comparison of power spectral characteristics

The power spectra of the  $v_{850}$  time series for all three categories of data are calculated first to compare the spectral characteristics of the NOGAPS analysis and 48-hour forecasts with those of the radiosonde observations. Overall, prominent oscillations (with large spectral power or power peak) usually belong to one of the following three timescales: the seasonal/intraseasonal, the 10-15 day period, and the synoptic (centered at 5-day) period. We will focus on the synoptic period in this study.

#### a. Meridional winds at 850 hPa

Figs. 1-6 show the comparisons of the  $v_{850}$  power spectra between RAOB,  $\tau_{00}$  analysis and  $\tau_{48}$  forecast at each of the six stations, arranged from the easternmost station (Majuro) to the

westernmost station (Koror). The  $\tau_{00}$  and  $\tau_{48}$  series are based on the grid point closest to the station. In each figure, the top panel (a) displays the power distributions of the RAOB (heavy solid),  $\tau_{00}$  (thin solid) and  $\tau_{48}$  (dashed) series, with all curves normalized with respect to the maximum value within the diagram. The middle panel (b) plots the coherence squares and phase difference between the RAOB and  $\tau_{00}$  series, while the lower panel (c) displays the coherence squares and phase difference between the RAOB and  $\tau_{48}$  series. We will discuss the  $\tau_{00}$ -RAOB comparisons in all six figures first, followed by the  $\tau_{48}$ -RAOB comparisons.

The spectral distribution in the RAOB's varies between stations, but in general two local spectra peaks may be identified. At the low frequency end, there is a peak near 32 days. Since the linear trend has been removed from the time series, this peak may represent both the seasonal trend and the intraseasonal oscillations, including possibly the Madden-Julian Oscillation. This low-frequency peak appears in all six stations except Majuro, where significant power is nevertheless indicated. At the synoptic frequency range, a local peak near five days is indicated in the RAOB data of all six stations, with Ponape, Guam and Koror showing substantial variance in the distribution. Between these two frequencies another power peak is often indicated, but the frequency location and the relative variances vary considerably from one station to another. At Majuro the RAOB's have a dominant peak near the 10-day period, significantly larger than the power near 5-day and overshadowing that of the the 32-day. At Truk, Guam and Yap, an indication of a peak is found near 8-day. At Ponape and Koror, the lower-frequency peak covers a broad band from 10- to 32-day.

i)  $v_{850}$ ,  $\tau_{00}$  vs RAOB

The shape of the  $r_{00}$  power spectra is in reasonably good agreement with the RAOB spectra at Ponape, Truk, Guam and Koror. At Ponape and Truk the NOGAPS analysis overestimates slightly the 5-day variance and underestimates slightly the lower frequency variances. At Guam the 5-day  $r_{00}$  variance is close to that of the RAOB's, and at Koror the analysis underestimates slightly the observed 5-day variance. The coherence squares at all four stations are mostly very high and the phase differences almost uniformly small throughout the synoptic and lower frequency range, indicating a good objective analysis climatology of the synoptic scale variabilities.

Large differences occur at the two other stations. At Majuro the  $r_{00}$  spectral distribution is quite different from the RAOB's, especially at the lower frequencies. Near the 5-day band the variance magnitudes are comparable but the shape is different, with the RAOB peak at 4.6-day but the analysis peak at 6.4-day. The coherence values are highest in the 4- to 5-day band, indicating that the  $r_{00}$  analysis is still reliable for representing the synoptic scale fluctuations. At other frequencies the coherences are lower than the four aforementioned stations, but they are all substantially above the significant threshold. The phase difference between the analysis and RAOB data is very small near 5-day, but non-negligible differences can be seen in adjacent frequencies. Near the 8-day point,  $r_{00}$  leads the RAOB oscillations by about  $45^\circ$ , indicating the analyzed disturbances move through this station at a speed  $1/8$  times faster than the observed. Near the 3-day point  $r_{00}$  lags RAOB slightly. These two points are also where the coherence squares fall off substantially.

At Yap the magnitude of the entire  $r_{00}$  spectrum is only a fraction of the observed. This is apparently because of the large RAOB variances with its maximum value nearly seven times (maximum  $v_{850}$  fluctuation amplitude nearly 2.5 times) that of

Koror, a station about five degrees to its southwest. This large fluctuation seemed to be ignored by NOGAPS as local anomalies, and the model chose to analyze towards the large scale flow, suppressing the RAOB fluctuations at Yap. Nevertheless, the two largest  $\tau_{00}$  peaks, at 32-day and 4.6-day, are in agreement with the RAOB. These are also the only frequency points where both the phase difference is small and the coherence squares is  $> 0.4$ .

ii)  $v_{850}$ ,  $\tau_{48}$  vs RAOB

Figs. 1-6 show that in all cases the correspondence between the  $\tau_{48}$  and RAOB  $v_{850}$  spectra is less than that between  $\tau_{00}$  and RAOB. At Majuro (Fig. 1a) the  $\tau_{48}$  synoptic peak occurs at 6.4-day rather than the observed 4.6-day. This is the same peak frequency as shown in the  $\tau_{00}$  spectrum, but unlike the  $\tau_{00}$  data where the magnitude of the 4-5 day variance is comparable to that of the RAOB, the  $\tau_{48}$  variance is less. The coherence squares (Fig. 1c) are mostly lower also, with larger phase differences. In fact, in the  $\tau_{00}$ -RAOB coherence distribution the values at the observed 4-5 day peak are close to the maximum in the entire frequency domain, but for  $\tau_{48}$ -RAOB the lower coherence values at this period band is relatively low within the frequency distribution. The maximum coherence between  $\tau_{48}$  and RAOB occurs at 6.4-day, which is the fictitious peak present in the NOGAPS analysis and forecast, but not in the radiosonde data.

At Ponape (Fig. 2) the good correspondence between  $\tau_{00}$  and RAOB spectral distributions is not reproduced by  $\tau_{48}$ . An increase in the power between 5- and 10-day occurs in the  $\tau_{48}$  spectrum, and the observed 4.6-day peak is shifted both directions to 4-day and 6.4-day. At Truk (Fig. 3) the observed 5.3-day peak is shifted to 6.4-day. At both Ponape and Truk the observed low-frequency power is substantially reduced. Thus a

substantial part of the observed seasonal trend is lost in the r48 forecast. The r48-RAOB cross spectra at both stations also indicate slightly lower coherence squares and slightly larger phase differences compared to the r00-RAOB cross spectra, although their values are still reasonable enough to indicate a fairly good agreement in the lower frequency and synoptic oscillations.

At Guam (Fig. 4) the power of the r48 spectrum around the 10-day frequency band is significantly larger than observed. Otherwise the spectral distribution is similar to the r00 spectrum. The good agreement of the synoptic peak around 5-day between r00 and RAOB is changed slightly, with a 20% decrease of power and a shift of the peak from the observed 5.2-day to 4.6-day. There is a reduction in coherence squares but the values remain significant throughout the lower- to synoptic frequency domain. Particularly, the coherence square around 5-day is very high, indicating very good agreement for the 5-day oscillations. The phase differences are again only slightly larger than the near zero r00-RAOB values.

As is the case with the r00 data at Yap (Fig. 5), the r48 oscillations have much smaller power compared to the very large RAOB fluctuations, and the coherence and phase data indicate almost no agreement. On the other hand, the r48 data show a predominant spectral peak at 10.7-day that is not present in the r00 analysis, where the peak power occurs at the lowest frequency (32-day).

The deterioration of the r48 spectrum from r00 at Koror (Fig. 6) is similar to that at Ponape, except it is somewhat more severe. The good agreement of the 5.2-day peak between r00 and RAOB spectra is totally lost, and is replaced by a forecasted 10.7-day peak. In the RAOB data, 10.7-day is not a peak but is on the edge of a broad low-frequency peak, with substantial



power. The coherence between  $\tau_{48}$  and RAOB is generally much reduced except around 11-16 days, and the phase difference is small only for these and lower frequencies. Since Koror and Yap are closely located to each other, it is possible that the 10.7-day peak present in Yap's  $\tau_{48}$  forecast is related to the one forecasted by Koror.

b. Zonal winds at 850 hPa

Comparisons of the RAOB,  $\tau_{00}$  and  $\tau_{48}$   $u_{850}$  spectra for the six stations are shown in Figs. 7-12. Again, the comparisons between RAOB and  $\tau_{00}$  will be discussed first, followed by the comparisons between RAOB and  $\tau_{48}$ .

The observed (RAOB)  $u_{850}$  power distributions are typically different from those of the corresponding  $v_{850}$ , and the magnitude of the  $u_{850}$  variances are generally larger than the  $v_{850}$  variances except at Majuro and Yap where the two are comparable. Table 1 lists the  $u_{850}$  and  $v_{850}$  spectral peaks in the lower-frequency band and the synoptic band (close to 5 days) observed in the RAOB data:

Table 1

<u>Station</u>	<u><math>v_{850}</math></u>		<u><math>u_{850}</math></u>	
	<u>low-freq</u>	<u>synoptic</u>	<u>low-freq</u>	<u>synoptic</u>
Majuro	10.7	4.6	$\geq 32$	weak
Ponape	16	4.6	$\geq 32$	6.4
Truk	$\geq 32$	5.3	$\geq 32$	4.2
Guam	$\geq 32$	5.3	$\geq 32$	4.6
Yap	$\geq 32$	4.6	16	weak
Koror	16	5.3	16	weak

Compared to the observed  $v$  spectra, the power in the  $u$  spectra is more concentrated in the lower frequencies. In the synoptic band, the peaks for  $u_{850}$  and  $v_{850}$  at each station are usually

different, and a relatively higher fraction of power is found in the v spectra than in the u spectra. This is consistent with previous findings (e.g., Wallace and Chang, 1969), and is an indication that the lower-frequency seasonal or intraseasonal oscillations are best represented by the u winds, and the synoptic timescale oscillations are best represented by the v winds. We will therefore use the v component as our primary time series to deduce the structure of synoptic scale disturbances in the RAOB, analysis and forecast data.

i)  $u_{850}$ ,  $\tau_{00}$  vs RAOB

In general, at most stations the agreements between the spectra of  $\tau_{00} u_{850}$  and its corresponding RAOB spectra (Figs. 6-12) are better than those of  $\tau_{00} v_{850}$  (Figs. 1-6), particularly the western stations of Truk, Guam, Yap and Koror. At these stations the spectra of  $\tau_{00} u_{850}$  are almost a reproduction of the respective RAOB spectra, which is not the case for the  $\tau_{00} v_{850}$  spectra. The phase differences between  $\tau_{00}$  and RAOB at these stations are near zero throughout the lower-frequency and the synoptic band, and are marked by very high coherence values. This is true even at Yap (Fig. 11), where, in contrast to the  $\tau_{00} v_{850}$  whose variance is only a fraction of the observed large fluctuations and the coherence and phase values show poor agreement with RAOB (Fig. 5), the  $\tau_{00} u_{850}$  is in good agreement with the observed  $u_{850}$  in spectral variance and distribution, and in coherence and phase values.

At the eastern end of the station network, Majuro (Fig. 7) shows the largest difference between  $\tau_{00} u_{850}$  and RAOB, but the general agreement is still somewhat better than the corresponding chart for  $v_{850}$  (Fig. 1). This is particularly true at the lower frequencies where the coherence square and phase difference are better also. The low-frequency spectral peak at Majuro occurs at 32-day for both RAOB and the  $\tau_{00}$  analysis,

indicating significant seasonal and/or intraseasonal power. However, the  $\tau_{00}$  peak is rather confined to the lowest frequency and does not indicate the significant spectral power at 16-day that is clearly seen in the RAOB. The synoptic band at Majuro is different: both  $\tau_{00}$  v and u at 850 hPa show peaks at a frequency different from the observed, but the magnitude of  $\tau_{00}$   $v_{850}$  power is comparable to that of RAOB while the  $\tau_{00}$   $u_{850}$  power is less. The coherence and phase values of the  $v_{850}$   $\tau_{00}$ -RAOB also show better agreement than the corresponding  $u_{850}$  values.

At Ponape the  $\tau_{00}$   $u_{850}$  spectral shape (Fig. 8) resembles RAOB better than the  $\tau_{00}$   $v_{850}$  (Fig. 2), especially at the lower frequency where the coherence square with RAOB for  $u_{850}$  is very high. However, similar to Majuro, the Ponape  $\tau_{00}$  spectrum fails to show the observed significant power at 16-day that is part of the broad low-frequency peak. At the synoptic band both  $\tau_{00}$   $u_{850}$  and  $v_{850}$  have the correct frequency for a spectral peak that is the same as the corresponding RAOB peak, with the former underestimating the observed variance, while the latter overestimates. The  $\tau_{00}$   $u_{850}$ -RAOB coherence square is also very high, showing a value close to 1 at the dominant synoptic peak of 6.4-day.

ii)  $u_{850}$ ,  $\tau_{48}$  vs RAOB

As expected, the comparison of spectra between  $\tau_{48}$   $u_{850}$  and the corresponding RAOB data in Fig. 7-12 show that there is some degradation from  $\tau_{00}$ , but the extent is generally small, and is less than the degradation of the  $v_{850}$   $\tau_{48}$  forecasts. At Majuro (Fig. 7) the  $\tau_{48}$   $u_{850}$  spectrum shows the same lowest frequency power at 32-day as  $\tau_{00}$ , but the variance is much higher than RAOB. The coherence is also much reduced. The entire  $\tau_{48}$  power spectrum appears similar to the RAOB spectrum. It now produces a peak with comparable magnitude to the RAOB peak at 8-day,

seemingly an improvement over the  $\tau_{00}$  spectrum. However, the coherence square with RAOB is very low, indicating that the relationship between the  $\tau_{48}$   $u_{850}$  forecasts and RAOB at Majuro is rather poor.

At Ponape (Fig. 8) the low-frequency power distribution is similar to  $\tau_{00}$  with power concentrated at the lowest frequency (32-day). Unlike the  $\tau_{00}$  data, the observed 6.4-day peak appears to be shifted to 8-day in the  $\tau_{48}$  spectrum. The coherence squares with RAOB for the band with frequency lower than the 5-day period are around 0.5, about half of the near perfect values given by the  $\tau_{00}$  data but still significant. The phase relationship shows small but discernible differences with RAOB, which is not the case for the  $\tau_{00}$  data.

At the western stations the  $\tau_{48}$   $u_{850}$  forecasts generally correspond fairly close to the  $\tau_{00}$  and the RAOB spectra. The exceptions are: at Truk the observed 6.4-day peak is shifted to 8-day in  $\tau_{48}$ , a feature similar to the neighboring station of Ponape; at Guam and Yap the low frequency variance is somewhat overforecasted; and at Koror the 16-day spectral peak is shifted to the lowest frequency of 32-day. In general the coherence squares with RAOB in the low-frequency and synoptic band is high or at least significant. The phase differences are similar to Ponape, small but more discernible than those shown by the  $\tau_{00}$  analyzed data.

#### c. Meridional winds at 200 hPa

The comparison between the RAOB and the  $\tau_{00}$  and  $\tau_{48}$   $v_{200}$  spectra for the stations are shown in Figs. 13-18. At all stations a dominant low-frequency spectral peak occurs at the 32-day period, which may or may not coincide with those observed at 850 hPa. The frequency locations of the synoptic peaks at the two

levels are more in agreement, although the magnitude of the relative and absolute variances may be different.

i)  $v_{200}$ ,  $\tau_{00}$  vs RAOB

At Majuro the observed 200 hPa peaks are at 32-day, 8-day and 4.6-day (Fig. 13). The 4.6-day peak is the same frequency as that found at 850 hPa, but the major 850 hPa peak of 10.7-day is missing at 200 hPa and is replaced by a power minimum. The  $\tau_{00}$  power spectrum simulates the 8-day peak very well and is supported by high coherence and near perfect in-phase relationship with RAOB. At the other two peak frequencies the  $\tau_{00}$  analysis underestimates the variances, and the lower coherence squares (and the small but noticeable phase difference at the lower frequency) indicate that the correspondence with RAOB are not good.

At Ponape (Fig. 14), the dominant peak occurs at the lowest frequency (32-day period), and relative to it all other peaks appear to be rather minor. The major  $v_{850}$  peak at 4.6-day is one of the minor ones and is not simulated well by the  $\tau_{00}$  analysis. The coherence and phase values between  $\tau_{00}$  and RAOB can only be considered as indicating a moderate correspondence between the two time series at this frequency. At Truk (Fig. 15) an 8-day peak is observed at 200 hPa and seems to correspond with one of the  $v_{850}$  spectral peaks, but the other synoptic  $v_{850}$  peak at 5.2 day is not observed. The  $\tau_{00}$  spectrum only simulates the observed 32-day peak, although the coherence square around the 8-day period is quite high. The phase difference throughout the synoptic and low-frequency bands is reasonably small.

At Guam, Yap and Koror (Figs. 16-18) two observed peaks occur: the commonly-seen 200 hPa peak at 32-day and another at 10.7-day. Both are detectable in the  $\tau_{00}$  analysis at all three

stations, although the signal for the 10.7-day peak is rather weak at Yap and Koror. The RAOB power spectrum over the synoptic band is fairly closely simulated by  $\tau_{00}$  also, although the minor peaks around 5-day are not exactly reproduced at Guam and Yap. For these two stations the coherence squares are very high at the 32-day and 10.7-day peaks, and are quite high elsewhere. At Koror the coherence square at 10.7-day, although still significant, is a minimum. The phase differences are reasonably small throughout the low and synoptic frequencies.

ii)  $v_{200}$ ,  $\tau_{48}$  vs RAOB

Compared to the  $\tau_{00}$  analysis, the  $\tau_{48}$  forecasts shown in Figs. 13-18 generally show a degradation in the loss of power and a deterioration of the coherence and phase values. The largest loss of power occurs in the eastern stations of Majuro (Fig. 13) and Ponape (Fig. 14). The only observed feature that is generally reproduced is the 32-day peak. At Majuro the  $\tau_{48}$   $v_{200}$  peak is too confined to the lowest frequency, and at Ponape it is substantially underestimated. At other stations the lowest frequency peak is rather well simulated by the  $\tau_{48}$  spectra. However, the good simulation of the spectrum does not guarantee a good cross-spectrum result. This is clearly seen at Yap (Fig. 17), where the 32-day coherence square between  $\tau_{48}$  and RAOB  $v_{200}$  is rather low even though the two spectral peaks at 32-day are almost identical. With the exception of Guam, the phase difference between  $\tau_{48}$  and RAOB time series at all other stations are large over the low-frequency and synoptic band.

d. Zonal winds at 200 hPa

i)  $u_{200}$ ,  $\tau_{00}$  vs RAOB

The observed spectra  $u_{200}$  at all stations (Figs. 19-24) shows power concentrating in the lowest frequency, and is well

represented by the  $\tau_{00}$  spectra at all stations with nearly identical powers, very high coherence squares and small phase differences in the  $\tau_{00}$ -RAOB cross-spectra. There is practically no spectral peak near the 5-day band, except a very slight indication at Truk. On the other hand, Guam and Yap (Figs. 22 and 23, respectively) show a secondary peak at 8-day. Only the Guam 8-day peak, which appears more significant than the one at Yap, is simulated by the  $\tau_{00}$  spectrum with an underestimate of the observed variance by about 1/3.

ii)  $u_{200}$ ,  $\tau_{48}$  vs RAOB

Except at Guam, the  $\tau_{48}$  power spectral distributions in Figs. 19-24 generally resemble the observed  $u_{200}$  spectra with power concentrated in the lowest frequency. However, the excellent reproduction of the magnitude of the variance by the  $\tau_{00}$  analysis no longer exists. At almost all stations the variance represented by  $\tau_{48}$   $u_{200}$  is substantially reduced, often by 50% or more. Only at Koror (Fig. 24) is the reduction less severe, which is probably a result of the overestimate of the variance in the  $\tau_{00}$  data. At Guam (Fig. 22) the  $\tau_{48}$  spectral shape is different, with a broad peak occupying the band between 8-32 day, which is not observed or analyzed. In general the  $\tau_{48}$ -RAOB coherence and phase values deteriorate significantly from the comparable  $\tau_{00}$  values.

4. Zonal structure of the synoptic wave disturbances

a. Longitudinal cross spectra of  $v_{850}$  along 7.5°N latitude

Because the  $v_{850}$  power spectra generally show the clearest signals of the synoptic (5-day) band disturbances, the zonal structure for these disturbances in terms of wavelength and phase velocity is determined by the cross spectra of  $v_{850}$  along the same latitude. The Caroline Islands stations are more or

less lined up longitudinally along the  $7.5^{\circ}\text{N}$  zone with Truk in the center. We therefore use Truk  $v_{850}$  as the base series to perform cross-spectral analysis with  $v_{850}$  at other stations to determine the observed zonal structure in this latitudinal zone. This is done at three frequencies corresponding to the periods of 4.6, 5.3 and 6.4 days. The results are shown in Fig. 25. In each of the panels the phase difference of  $v_{850}$  at a station with respect to Truk is plotted by the leading letter of the station name, and the coherence square is indicated by a star sign at the same longitude. In general the coherence falls out as the distance of a station from Truk increases, but the values all meet the 95% significance level test. The phase difference shows consistently a westward (easterly) propagation with a wavelength near twice the distance between Majuro and Ponape, or about 3300 km. This estimated wavelength increases with the period. It is somewhat shorter at 4.6-day and somewhat longer at 6.4-day, to give a easterly phase speed that is fairly steady. It may be interesting to note that this semi-nondispersive characteristic has been noted in longitude-time series of satellite cloud data over the tropical western Pacific (Chang and Lim, 1982).

The signals of the synoptic wave disturbances are most prominent in the  $v_{850}$  time series. Because of the vague signals in other parameters, the station RAOB data will not be used as the basis to determine the zonal structure. For these parameters the comparison will be restricted to the general characteristics obtained from the  $\tau_{00}$  and  $\tau_{48}$  data.

#### i) Comparison of $\tau_{00}$ vs. RAOB

Also plotted in Fig. 25 are the coherence squares and phase differences calculated from  $\tau_{00}$   $v_{850}$  at grid points along  $7.5^{\circ}\text{N}$ , with  $\tau_{00}$   $v_{850}$  at the point nearest Truk as the base series. It can be seen that the phase line of the  $\tau_{00}$  cross-spectra agrees



quite well with the phase points calculated from the station RAOB data at all three frequencies, particularly to the east of Truk. To the west, data from the grid point closest to the Guam longitude agrees well with RAOB, even though Guam is the farthest station from 7.5°N. Apparently the wave disturbance has sufficient meridional scale without a steep tilt to allow this result. At 4.6-day the grid point data near Yap has a smaller phase difference (implying shorter wavelength) than that indicated by the station RAOB, and at 6.4-day the grid point data near Koror has a larger phase difference (implying longer wavelength) than the RAOB data. Thus the  $r_{00}$  analysis minimizes the increase of the estimated wavelength as the wave period increases. Namely,  $r_{00}$  gives a more constant estimate of the zonal wavelength within the synoptic band than the station data. The  $r_{00}$  coherence squares also show a consistent fall off away from the base point near Truk. They are in general higher than the RAOB values, which can be expected because of the spatial objective analysis.

ii) Comparison of  $r_{48}$  vs. RAOB

Fig. 26 is similar to Fig. 25 except here the cross spectra are determined from the  $r_{48}$  time series. The agreement between these results and the station RAOB or  $r_{00}$  analysis time series are fairly good, except for regions west of Yap, where for both the 5.3- and 6.4-day periods the consistent westward propagation is lost in the  $r_{48}$  fields and the coherence squares are meaninglessly low. An examination of Figs. 11-12 indicate that the  $r_{48}$  forecast of  $v_{850}$  is very poor near Yap and Koror.

b. Longitudinal cross spectra of  $v_{850}$  as a function of latitude

The good agreement between  $r_{00}$  and RAOB  $v_{850}$  longitudinal structure suggests that an estimate of the phase propagation of

the synoptic wave disturbances based on  $\tau_{00} v_{850}$  is worthwhile, and that a comparison between  $\tau_{48}$  and  $\tau_{00} v_{850}$  may provide a meaningful evaluation of the model's performance of forecasting the propagation characteristics of the tropical synoptic waves in the vicinity of the Caroline Islands. In this section the zonal structure at each latitude will be calculated from the phase differences and coherence squares of the grid point data, for both  $\tau_{00}$  and  $\tau_{48}$ , with the  $150^\circ\text{E}$  data as the base series. The  $150^\circ\text{E}$  base longitude is chosen because it is close to the longitude of Truk, the base station used in the RAOB comparisons. These cross spectra will be referred to as the inter-x cross spectra, and are computed for different latitudes and presented on a two-dimensional horizontal map.

i) Inter-x  $\tau_{00} v_{850}$

Fig. 27a shows the inter-x cross spectra for  $\tau_{00}$ . Here at each grid point the cross spectra between the  $v_{850}$  time series and that at  $150^\circ\text{E}$  of the same latitude is plotted as a vector, whose direction indicates the phase difference and whose magnitude is proportional to the coherence square. For coherence squares less than the 95% significance level, the vector is not plotted. Zero phase difference is indicated by a vector pointing northward ( $0^\circ$ ), and as the vector rotates clockwise the positive phase difference increases. For vectors pointing to the east, the base series ( $v_{850}$  at  $150^\circ\text{E}$ ) lags, and for vectors pointing to the west the base series leads. Depending on the position of a grid point relative to the base longitude, the direction of propagation can be determined, and a zonal wavelength can be inferred from the phase differences.

In Fig. 27a the phase propagation characteristics of the synoptic band waves as a function of latitude is clearly depicted. At and north of  $17.5^\circ\text{N}$  eastward propagation can be found over a large longitudinal span, with a wavelength of about

60° longitude. This is apparently the signals generated by the winter monsoon synoptic systems (cyclones and anticyclones) as they move out of the Asian continent into the western Pacific (eg. Boyle and Chen, 1987). At and south of 15°N the easterly wave disturbances are fairly well defined by the westward phase propagation, although significant coherence values are limited to a more confined area within the tropical western Pacific east of 135°-140°E. The implied zonal wavelength also varies somewhat with latitude. The phase vectors to the east of the base longitude indicate a half-wavelength that changes from about 15° longitude at 10°N to about 17.5° longitude at the equator. The phase vectors to the west of the base longitude suggest a slightly longer half-wavelength, but the coherence values fade below the 95% significance level. Overall, the phase structure suggest a zonal wavelength of about 33° longitude at 10°N, in agreement with the results shown in the  $\tau_{00}$ -RAOB inter-x comparison (Fig. 25). Along the equator the wavelength is about 38° longitude. Immediately to the south of the equator the wavelength appears to be even longer, especially to the west of the 150°E base longitude, however the very low coherence prevents an estimate of the wavelength there.

ii) Inter-X  $\tau_{48}$   $v_{850}$

Fig. 27b shows the inter-x cross spectra for  $\tau_{48}$   $v_{850}$ , again with 150°E as the base longitude. The result is an excellent reproduction of the corresponding diagram of  $\tau_{00}$  (Fig. 27a). The entire latitudinal distribution of horizontal wavelength and coherences are very well represented by the 48-h forecast data, even including some of the details that are somewhat remote from the base longitude. For example, the cross spectral vectors to the south of Sumatra in the lower-left corner of the diagram are nearly identical to the results obtained in the  $\tau_{00}$  diagram.

There are a few above-significance level phase vectors in the  $\tau_{48}$   $v_{850}$  results that do not show up in the  $\tau_{00}$  results. These are in the  $130-140^{\circ}\text{E}$ ,  $10^{\circ}\text{S}$ -equator region southwest of New Guinea and indicate a westward propagation of rather long wavelength. (A half-wavelength of near  $40^{\circ}$  longitude can be inferred from the phase vectors). This long wavelength is in the range of the mixed Rossby-gravity wave that was observed in the equatorial upper-troposphere (Yanai and Maruyama, 196x). It is worth noting that this indication of the planetary-scale waves is undetectable in the  $\tau_{00}$  analysis (Fig. 27a).

### c. Longitudinal cross spectra of $u_{850}$

#### i) Inter-X $\tau_{00}$ $u_{850}$

Fig. 28a shows the inter-x cross spectra for the zonal wind at 850 hPa with  $150^{\circ}\text{E}$  as the base longitude. In the northern domain the eastward propagation characteristics, including the coherence and phase values and their inferred wavelength, are very similar to the meridional wind results (Fig. 27a). However, the domain of eastward propagation here covers all latitudes north of  $12.5^{\circ}\text{N}$ , five degrees to the south of the lowest latitude of eastward propagation determined from the  $v_{850}$  inter-x cross spectra. Thus it appears that the signals of tropical easterly wave disturbances are mainly in the  $v$  component, and are masked by the subtropical westerly propagating systems whose  $u$  fluctuations remain strong in the  $12.5^{\circ}-17.5^{\circ}\text{N}$  zone.

In the equatorial latitudes the  $u$  results are more different than the  $v$  results found in Fig. 27a. There is an indication of westward propagation, but the coherence squares are significantly lower between the equator and  $10^{\circ}\text{N}$ , except in the immediate vicinity and slightly to the east of the base longitude. Based on this partial wave structure, the implied

wavelength should be longer than that shown in the meridional wind results. At the equator and southward, the results suggest an even longer wavelength in the westward propagation over Indonesia. The wavelength is about  $120^\circ$  longitude, or wavenumber three. This clear planetary-scale wave propagation in the u cross-spectra contrasts sharply with the lack of a coherent propagation signal in the v cross spectra in the equatorial zone.

ii) Inter-X  $\tau_{48}$   $u_{850}$

The  $\tau_{48}$   $u_{850}$  inter-x cross spectra shown in Fig. 28b resemble closely the  $\tau_{00}$  results (Fig. 28a), with eastward propagating synoptic-scale waves north of  $12.5^\circ\text{N}$ , and partial structure of westward propagating wave south of  $10^\circ\text{N}$ . The near wavenumber three planetary wave is again found in the latitudes south of the equator.

d. Longitudinal cross spectra of  $v_{200}$

i) Inter-X  $\tau_{00}$   $v_{200}$

At 200 hPa the  $\tau_{00}$   $v_{200}$  inter-x cross spectra with  $150^\circ\text{E}$  as the base longitude again displays the eastward propagation in the northern latitudes and westward propagation at and south of  $10^\circ\text{N}$  (Fig. 29a). However, the westward propagating wavelength is close to  $50^\circ$  longitude to the east of  $150^\circ\text{E}$ , and somewhat longer and less well defined to the west. Thus, the upper tropospheric wavelength is longer than that at 850 hPa. A longer upper tropospheric wavelength has been reported by many previous observations based on radiosonde data (e.g., Chang et al, 1970; Chang and Miller, 1977), and suggests that the vertical wave structure may be complex. The lower and upper tropospheric westward propagating disturbances may be far from tightly coupled.

ii) Inter-X  $\tau_{48}$   $v_{200}$

Fig. 29b shows the inter-x cross spectra for  $\tau_{48}$   $v_{200}$ . In general, it is in good agreement with the patterns of  $\tau_{00}$  (Fig. 29a). The difference occurs mainly east of the  $150^\circ\text{E}$  base longitude, where between  $10^\circ\text{N}$ - $20^\circ\text{N}$  the eastward propagating waves show better organization than the  $\tau_{00}$  results with higher coherence values. South of  $10^\circ\text{N}$  the westward propagating waves are less organized than the  $\tau_{00}$  results, having lower coherences.

e. Longitudinal cross spectra of  $u_{200}$

i) Inter-X  $\tau_{00}$   $u_{200}$

Fig. 30a shows that the  $\tau_{00}$  analyzed  $u_{200}$  again indicates eastward propagation in the north and westward propagation in the south. However, the tropical westward propagation, which is evident at  $15^\circ\text{N}$  and southward, has a much longer wavelength than that indicated by the  $\tau_{00}$   $v_{200}$  inter-x cross spectra (Fig. 29a). Based on the few significant phase vectors over Borneo, Sumatra and Java (in the lower-left corner of the diagram), the quarter-cycle phase difference may be placed near  $120^\circ\text{E}$ , which gives an estimate of a wavelength of  $120^\circ$  longitude. This is the same estimate as the 850 hPa  $u$  results.

ii) Inter-X  $\tau_{48}$   $u_{200}$

The  $\tau_{48}$   $u_{200}$  inter-x cross spectra are shown in Fig. 30b. Compared to the  $\tau_{00}$  diagram (Fig. 30a), the gross patterns are roughly similar, with some notable differences. East of  $150^\circ\text{E}$  the coherence is higher between  $12.5^\circ\text{N}$ - $20^\circ\text{N}$ , and lower in the equatorial belt and to the south. The eastward propagating signals also expand southward from that indicated in the  $\tau_{00}$

chart, to  $12.5^{\circ}\text{N}$ . This result is similar to the comparison of the  $\tau_{48}$  vs  $\tau_{10}$   $v_{200}$  inter-x spectra. It seems that in the area of forecasted eastward propagation the forecasted field has better inter-x organization downstream. To the south the reverse appears true. Here the waves are propagating westward, and upstream from the base longitude the wave structure is less organized than indicated by the  $\tau_{00}$  analysis.

Also in Fig. 30b the inter-x cross spectra in the entire equatorial zone show a tendency towards westward phase propagation but very small phase differences over all longitudes. Thus a zonal scale much larger than the wavenumber three shown in the  $\tau_{00}$   $u_{200}$  is indicated. This is a poorer performance compared to that of  $u$  at 850 hPa (Figs. 28a,b), where the 48-h forecast successfully reproduces the  $120^{\circ}$  longitude wavelength found in the  $\tau_{00}$  inter-x cross spectra.

## 5. Meridional structure of the synoptic wave disturbances

In this section the meridional structure for each field is examined by comparing the cross spectra between time series at a grid point and that at  $10^{\circ}\text{N}$  of the same longitude. Here  $10^{\circ}\text{N}$  is chosen to be the base latitude. The results will be referred to as the inter-y cross spectra, and are plotted as vectors representing the phase differences and coherence squares in the same way as the inter-x cross spectra.

### a. Meridional cross spectra of $v_{850}$

Fig. 31a displays the inter-y cross spectra for  $\tau_{00}$   $v_{850}$ . South of  $10^{\circ}\text{N}$ , most vectors rotate clockwise with increasing phase difference southward. This phase characteristic is especially prominent in the western Pacific east of  $140^{\circ}\text{E}$ . The positive phase angle indicates that the  $v$  fluctuations at  $10^{\circ}\text{N}$  lags those

at latitudes to the south. Because the waves propagate westward over this area, a northeast-southwest tilt is indicated. The phase difference approaches a quarter-cycle between  $10^{\circ}\text{S}$  and  $10^{\circ}\text{N}$ . To the north of  $10^{\circ}\text{N}$  most of the vectors in the western tropical Pacific show an opposite phase difference, which again implies a northeast-southwest tilt. While there are no direct meridional cross-spectra in the RAOB data available to verify this result, this structure is consistent with all previously observed meridional structure of the easterly waves in the northern tropics (Chang et al., 1970, 1977; Reed and Recker, 1971; Burpee, 1972, 1974; Reed et al, 1977). The  $\tau_{48}$   $u_{850}$  inter-y cross spectra are shown in Fig. 31b. They resemble the patterns of Fig. 31a very closely. The only difference is that the northeast-southwest tilt in the equator- $15^{\circ}\text{N}$  band is somewhat less prominent compared to  $\tau_{00}$ .

#### b. Meridional cross spectra of $u_{850}$

The  $\tau_{00}$   $u_{850}$  meridional structure (Fig. 32a) also indicate a tendency of the northeast-southwest tilt in the tropical western Pacific, but the phase difference is less prominent or even changes direction south of  $10^{\circ}\text{N}$ . The tilt cannot be traced continuously south of the equator, and in the region east of  $150^{\circ}\text{E}$  the phase is about a half-cycle out of phase with the northern tropics. The out-of-phase relationship indicates that  $u_{850}$  is anti-symmetric about the equator, a structure that is consistent with the mixed Rossby-gravity wave mode. Coupled with the result of a longer zonal wavelength in the equatorial belt particularly in the  $u$  field, it seems that in the equatorial belt the 5-day  $u$  fluctuations are mainly manifestations of the mixed Rossby-gravity waves.

The inter-y cross spectra for  $\tau_{48}$   $u_{850}$  are shown in Fig. 32b. Compared to  $\tau_{00}$ , the coherence squares south of  $10^{\circ}\text{N}$  decrease over most of the longitudes except between  $150^{\circ}\text{E}$ - $160^{\circ}\text{E}$ .



### c. Meridional cross spectra of $v_{200}$

In the  $\tau_{00} v_{200}$  inter-y structure (Fig. 33a) the northeast-southwest tilt between the equator-15°N is seen, but with a notable exception. Between 130°E-145°E the meridional tilt is northwest-southeast. The  $\tau_{48} v_{200}$  results (Fig. 33b), however, show a northeast-southwest tilt throughout the equatorial western Pacific.

### d. Meridional cross spectra of $u_{200}$

Fig. 34a shows the northeast-southwest tilt throughout the western Pacific in the  $\tau_{00} u_{200}$  inter-y cross spectra. In the  $\tau_{48} u_{200}$  results, shown in Fig. 34b, this tilt is much less prominent.

## 6. Vertical structure of the synoptic wave disturbances

The vertical structure of the synoptic wave disturbances is determined from cross-spectral analyses between different vertical levels. Figs. 35-38 show the results at the 5-day band (averaged over 4.6-, 5.3- and 6.4-day) with  $v$  at 850 hPa as the base time series and  $v$  at 700, 500, 300 and 200 hPa, respectively, as the other series. Each of these figures have two panels, panel a is for  $\tau_{00}$  and panel b is for  $\tau_{48}$ . For these cross spectra a positive phase difference indicates that  $v_{850}$  lags the other series.

Fig. 35a shows that the coherence squares are generally high between  $\tau_{00} v_{850}$  and  $v_{700}$  for the 5-day band, apparently due to the closeness of the two levels. North of 20°N where the waves propagate eastward, the phase difference is negative and indicates that  $v_{850}$  leads  $v_{700}$ . This means that there is a

westward tilt with height, as may be expected for the midlatitude baroclinic systems. In the tropical westward propagating region most of the phase difference is small, indicating a rather small tilt. The main exception is over the equatorial region east of  $150^{\circ}\text{E}$ , where the phase differences indicate a eastward tilt with height. Fig. 35b shows that  $r_{48}$  reproduces the  $r_{00}$  structure very well.

Fig. 36a shows the vertical tilt between  $v_{850}$  and  $v_{500}$  at  $r_{00}$ . The westward tilt north of  $15^{\circ}\text{N}$  is more prominent, and the eastward tilt is visible in the southern equatorial region east of  $150^{\circ}\text{E}$ . In addition, west of  $140^{\circ}\text{E}$  and east of the Philippines an eastward tilt of up to 0.1 cycle can be found as far south as  $10^{\circ}\text{N}$  and slightly beyond. This is the region of Yap and Koror where previous spectral analysis found a westward vertical tilt in the easterly waves during summer (Chang et al, 1970, 1977). Holton (1970) has proposed in a numerical simulation that the vertical shear of the tropical easterly waves are related to the vertical shear of the time-mean flow. The difference in the vertical tilt between the present study and the previous ones may be attributable to the difference in the vertical shear, which changes from a easterly shear during the northern-summer southwest monsoon to a westerly shear during the northern-winter northeast monsoon. The coherence squares are below the significant level southwest of  $10^{\circ}\text{N}$ ,  $140^{\circ}\text{E}$  and in the South China Sea. The lack of coherence between 850 hPa and 500 hPa in the latter region is expected, as this is the period where synoptic timescale fluctuations are heavily influenced by winter monsoon surge events whose vertical structure is limited to below 700 hPa (Chang et al., 1983; Boyle and Chen, 1987).

Fig. 36b shows that again the  $r_{48}$  results simulate the  $r_{00}$  structure very well. It may be noticed that between the equator and  $10^{\circ}\text{N}$ , the coherence values for  $r_{48}$  are slightly higher than  $r_{00}$  to the west of  $160^{\circ}\text{E}$  and slightly lower to the east.

Namely, west of 160°E the vertical structure of the 5-day waves in the 500-850 hPa layer is somewhat more clearly defined in the r48 forecast field than the r00 analysis, and east of 160°E it is somewhat less clearly defined in the r48 field than the r00 field. As will be discussed in the following paragraphs, this westward shifting of the area of vertical coherence from r00 to r48 in the equatorial central-western Pacific becomes more prominent when the cross spectra between v<sub>850</sub> and upper tropospheric v are examined.

Fig. 37a shows the r00 vertical structure between v<sub>850</sub> and v<sub>300</sub>. Unlike previous diagrams (Figs. 35-36) that show significant vertical coherence over a large longitudinal span in the lower troposphere over the equatorial western Pacific, the vertical coherence between lower and upper troposphere is restricted to just east of 160°E. Between the equator and 10°N, the westward propagating 5-day waves show a westward tilt with height of around one quarter cycle phase shift between 850 and 300 hPa. As the waves propagate westward across 160°E, signals of vertical coupling disappear. Fig. 37b shows the v<sub>850</sub> - v<sub>300</sub> structure as represented by the r48 forecast fields. A strong contrast can be seen between Figs. 37a and 37b. East of 160°E, the significant vertical coupling signals analyzed by r00 data in the equatorial region (Fig. 37a) weaken somewhat in the r48 forecasts (Fig. 37b). On the other hand, west of 160°E the r48 data generate a significant vertical structure that closely couple the two levels. The structure is a westward tilt with a phase shift that increases progressively toward west. This vertical coupling is not present in the r00 data.

The difference in the lower-upper troposphere vertical coupling over the equatorial Pacific between the r00 analysis and r48 forecast is seen even more clearly in the v<sub>850</sub> - v<sub>200</sub> cross spectra (Fig. 38). In the equator-10°N band the r00 result (Fig. 38a) shows a weak vertical coupling east of 160°E, with

some grid points having marginally significant coherence values indicating a westward tilt. West of this longitude, between 140°E-160°E, the two levels are basically not coupled. West of 140°E the northern equatorial region shows a limited area of high coherence and large out-of-phase tilt between  $v_{850}$  and  $v_{200}$ . For  $r_{48}$  (Fig. 38b) this variation with respect to the 160°E longitude is reversed. East of 160°E the weak vertical coupling signals in the  $r_{00}$  analysis is now even weaker, with no significant coherence on either side of the equator. West of 160°E where the  $r_{00}$  data show no vertical coupling,  $r_{48}$  shows large coherence values and a clear westward tilt with height. As is shown in the  $r_{48}$   $v_{850} - v_{300}$  results, this tilt also increases progressively as the waves propagate toward the west, and becomes nearly one half cycle out of phase at 150°E.

The vertical structure within the upper troposphere can be determined from Fig. 39, which shows the vertical cross spectra between  $v_{300} - v_{200}$ , with  $v_{200}$  as the base series. Here both  $r_{00}$  (Fig. 39a) and  $r_{48}$  (Fig. 39b) show a significant westward tilt structure between the two levels in the equatorial central-west Pacific. While the two diagrams resemble each other reasonably well, it may still be seen that the  $r_{48}$  data appear to move the maximum coherence westward from near 170°E in the  $r_{00}$  diagram to around 152.5°E. The very modest vertical tilt in the latter area is also replaced by the westward tilt seen in the upstream region of the  $r_{00}$  result.

To summarize, Figs. 37-38 indicate that in the equatorial central-western Pacific the  $r_{48}$  forecasts appear to generate artificial vertically-organized wave structure that couples the lower and upper troposphere downstream from where a weakly coupled structure is contained in the  $r_{00}$  analyses. The artificial vertical structure gives rise to a progressively larger westward tilt with height from 160°E westward to 150°E and beyond. Figs. 36 and 39 indicate that this tendency of

downstream propagation of the wave structure by the  $\tau_{48}$  forecast can also be detected within the lower troposphere (850-500 hPa) and within the upper troposphere (300-200 hPa), respectively. The location of the Caroline Island stations along  $7^{\circ}$ - $7.5^{\circ}$ N allows an evaluation of this result by comparing the  $\tau_{00}$  and  $\tau_{48}$  vertical cross spectra with those from the RAOB's to the west and to the east of the  $160^{\circ}$ E longitude. Fig. 40 shows the coherence squares between  $v_{850}$  and  $v$  at 700, 500, 400, 300 and 200 hPa for the frequency of  $(5.3 \text{ day})^{-1}$  for RAOB,  $\tau_{00}$  and  $\tau_{48}$ , respectively, at the stations Majuro, Ponape and Truk. Here Majuro ( $7.1^{\circ}$ N,  $171.4^{\circ}$ E) is east of the  $160^{\circ}$ E longitude, and Ponape ( $7^{\circ}$ N,  $158.2^{\circ}$ E) and Truk ( $7.5^{\circ}$ N,  $151.9^{\circ}$ E) are to the west of  $160^{\circ}$ E. At all three stations the  $v_{850}$ - $v_{700}$  coherence values are high, and at each station the  $\tau_{48}$  and  $\tau_{00}$  coherence squares are nearly identical. For cross spectra between  $v_{850}$  and  $v$  at 500 hPa and higher levels, the  $\tau_{48}$ - $\tau_{00}$  coherence comparisons show the same anomalous patterns east and west of  $160^{\circ}$ E as found in Figs. 36-38. At Majuro, the  $\tau_{48}$  values are either comparable to or less than the  $\tau_{00}$  values, indicating that the  $\tau_{48}$  data forecast a slightly less degree of organization for the 5-day oscillations. The reverse is true at Ponape and Truk, where the coherence values indicate, in general, a significantly higher degree of deep tropospheric coupling in the  $\tau_{48}$  data that are not present in the  $\tau_{00}$  analysis.

At all three stations and levels the  $\tau_{00}$  coherence square is always larger than the corresponding RAOB value, which may be expected due to the model's three-dimensional objective analysis. The "ground truth", or observed, degree of coupling between lower and upper troposphere may be represented by the RAOB coherence squares of  $v_{850}$ - $v_{200}$  and  $v_{850}$ - $v_{300}$ . These values are higher for Majuro than for Ponape and Truk, to the extent that for  $v_{850}$ - $v_{300}$  the coherence is above significance level at Majuro but below it at Ponape and Truk. Thus the RAOB confirms

the  $\tau_{00}$  result that the vertical coupling is significant only east of  $160^\circ\text{E}$ .

If the vertical structure difference across  $160^\circ\text{E}$  between  $\tau_{48}$  and  $\tau_{00}$  is indeed a result of an artificial downstream propagation by the forecast model, we may expect that an intermediate structure will show in the  $\tau_{24}$  data. Fig. 41 shows the  $\tau_{24}$  vertical cross spectra between  $v_{850}$  as the base series and  $v$  at (a) 300 hPa and (b) 200 hPa, respectively. A comparison of Fig. 41a with Figs. 37a,b readily shows that, in the region east of  $160^\circ\text{E}$  between equator- $10^\circ\text{N}$ , the  $v_{850}$ - $v_{300}$  coherence values at  $\tau_{24}$  are higher than those at  $\tau_{00}$  and lower than those at  $\tau_{48}$ . The vertical phase shift for  $\tau_{24}$ , an increasingly larger westward tilt with height, is consistent with that at  $\tau_{48}$ . The same conclusions can be drawn in the comparison of the vertical cross spectra at  $\tau_{24}$  (Fig. 41b) with those at  $\tau_{00}$  (Fig. 38a) and  $\tau_{48}$  (Fig. 38b).

## 7. Thermal structure of the synoptic wave disturbances

The thermal structure of the 5-day disturbances may be examined by a cross-spectral analysis between the meridional velocity and temperature (T) at various levels. However, because of the smallness of the temperature fluctuations for tropical synoptic scale motions, the temperature signals are often too weak to produce cross spectra that are significant (Chang et al., 1970). Due to the uncertainties involved, we will only look at the  $v$ -T cross spectra at the six grid points that are closest to a RAOB station in the Caroline Islands network. Table 2 shows the coherence squares and phase differences between  $v_{850}$  and temperature at 925, 850, 700, 500, 400, and 300 hPa. Here only those results with a coherence square  $\geq 0.14$  (95% significance level) are formally included, but those with a coherence square  $\geq 0.11$  are also listed. It is seen that only the three eastern stations, Majuro, Truk and Ponape, produce substantial numbers

of significant results, and they are mainly for the upper-tropospheric temperatures.

Table 2. Coherence square and phase difference between  $v_{850}$  as the base series and temperature at different levels for the Caroline Islands region. Values associated with  $CH^2 \geq .14$  (95% significant level) are shown as regular types. Values associated with  $.11 \leq CH^2 < .14$  are shown in italics. Values associated with  $CH^2 < .11$  are not shown.

	Truk (152°E, 7.5°N)			Ponape (158°E, 7°N)			Majuro (171°E, 7.1°N)		
	RAOB	$\tau_{00}$	$\tau_{48}$	RAOB	$\tau_{00}$	$\tau_{48}$	RAOB	$\tau_{00}$	$\tau_{48}$
	T <sub>300</sub> CH <sup>2</sup>	-	.26	.52	-	.53	.42	.15	.11
Phase	-	101°	101°	-	96°	107°	44°	75°	-
T <sub>400</sub> CH <sup>2</sup>	-	.17	.73	.18	.36	.62	.35	.24	.13
Phase	-	86°	74°	60°	101°	77°	24°	61°	28°
T <sub>500</sub> CH <sup>2</sup>	-	.34	.64	.14	.38	.55	.31	.33	.12
Phase	-	60°	50°	83°	63°	49°	22°	77°	84°
T <sub>700</sub> CH <sup>2</sup>	-	.11	-	.29	-	-	-	-	-
Phase	-	-31°	-	-143°	-	-	-	-	-
T <sub>850</sub> CH <sup>2</sup>	-	-	-	-	.14	-	.12	-	.48
Phase	-	-	-	-	74°	-	88°	-	-145°
T <sub>925</sub> CH <sup>2</sup>	-	.28	.19	-	.28	-	-	-	.39
Phase	-	113°	-106°	-	69°	-	-	-	-103°

Table 2. (continued)

	Koror			Yap			Guam		
	(134°E, 7.3°N)			(138°E, 9.5°N)			(145°E, 13.6°N)		
	RAOB	$\tau_{00}$	$\tau_{48}$	RAOB	$\tau_{00}$	$\tau_{48}$	RAOB	$\tau_{00}$	$\tau_{48}$
T <sub>300</sub> CH <sup>2</sup>	-	-	-	-	-	-	-	-	-
Phase	-	-	-	-	-	-	-	-	-
T <sub>400</sub> CH <sup>2</sup>	-	-	-	-	-	-	-	-	-
Phase	-	-	-	-	-	-	-	-	-
T <sub>500</sub> CH <sup>2</sup>	-	-	-	-	.11	.11	-	-	-
Phase	-	-	-	-	55°	76°	-	-	-
T <sub>700</sub> CH <sup>2</sup>	-	.17	-	-	.14	-	-	-	-
Phase	-	60	-	-	86	-	-	-	-
T <sub>850</sub> CH <sup>2</sup>	-	-	-	.62	-	-	-	.12	-
Phase	-	-	-	63	-	-	-	62°	-
T <sub>925</sub> CH <sup>2</sup>	-	-	-	-	-	.11	-	.20	-
Phase	-	-	-	-	-	-104°	-	53°	-

At Ponape and Truk both the  $\tau_{00}$  and  $\tau_{48}$  results show an approximate one-quarter cycle phase difference between  $v_{850}$  and temperature at the 300 and 400 hPa levels. This phase difference is somewhat smaller (about 1/6 cycle) with respect to T<sub>500</sub>. The positive phase indicates that maximum temperature leads maximum  $v_{850}$ , thus placing the upper-tropospheric warm core in the 850 hPa trough region. Therefore the model analysis and forecast data both show a "warm core" structure for the 5-day disturbances, and this agrees with previous results based on station data (Chang et al, 1970, 1977). However, the RAOB



$v_{850}$ -T cross spectra give significant results only at Ponape. Here the phase differences indicate a warm core structure around 500 hPa, but the result for  $T_{200}$  is below the significance level. The warm core structure would, hydrostatically, suggest a weakening of the wave trough with height. Compared to the vertical cross spectra between  $v$  at different levels, which shows very little tilt below 500 hPa and a westward tilt above, we may sketch a schematic diagram of the vertical cross section of the 5-day disturbances as shown in Fig. 42a. At Majuro  $r_{48}$  data do not give significant  $v_{850}$ -T results in the middle-upper troposphere. The  $r_{00}$  results in the middle levels are consistent with Truk and Ponape, but the RAOB data indicate that while the disturbances are still warm core, the phase difference between  $v_{850}$  and middle-upper level temperature is slightly smaller. The schematic structure shown in Fig. 42a is basically applicable at Majuro, except that the upper warm core is slightly shifted to the east and that the upper tropospheric westward tilt is slightly stronger according to the vertical cross spectra between  $v$  at different levels shown earlier (Fig. 37a).

At the three eastern stations, evidences of a model that is trying to organize the middle-upper tropospheric wave structure downstream in the direction of propagation can again be found. Basically, west of  $160^{\circ}\text{E}$  at Majuro the  $r_{48}$  coherence is weaker than  $r_{00}$ , while east of  $160^{\circ}\text{E}$  at Truk and Ponape the reverse is true.

At the lower levels the few significant cross spectral results give a confusing picture of the thermal structure near the surface. For  $r_{00}$ , both Ponape and Truk give a positive quarter-cycle phase difference between  $v_{850}$ - $T_{925}$ , indicating a temperature maximum that is approximately in-phase with the low-level trough. This warm core at 925 hPa would place the maximum amplitude of the wave trough near the surface in order

to satisfy hydrostatic balance. On the other hand, the  $\tau_{48}$  results at Majuro, Truk and Yap indicate that the phase of  $v_{850}-T_{925}$  is about  $-1/4$  cycle, or a cold core at 925 hPa. Unfortunately, the corresponding RAOB information is not available because 925 hPa is not a standard data level. Although previous observational studies by Chang et al (1970) suggests that the tropical easterly waves over the western Pacific tend to have a cold core structure, mainly during summer, near the surface, we will have to view the present result as showing an artificial model effect that converts the analyzed low-level warm core to cold core in the  $\tau_{48}$  forecast. There are several possible mechanisms that may cause a low-level cold core structure. If forced lifting such as CISK is present below a cloud base that is too high, adiabatic cooling will occur. If precipitation is intense through an unsaturated environment near the surface, the re-evaporation of the falling rain will cause cooling. Another possibility is that frictional damping is too strong and dissipates too much kinetic energy near the surface, resulting in a weaker wave amplitude there and the hydrostatic constraint will produce a cold-core trough.

At the other three stations, only a few cross-spectra of  $v_{850}-T$  above the significance level are obtained in the lower troposphere, and none in the upper troposphere. At Yap and Koror the  $\tau_{00}$  data show a positive phase of about  $1/5$  cycle for  $T_{700}$ , suggesting that the middle tropospheric warm core over the 850 hPa trough extends to lower levels at these western stations. This seems to be supported by the RAOB result for  $T_{850}$  at Yap. The  $v_{850}-T_{925}$  result for  $\tau_{00}$  at Guam, and the less significant result for  $\tau_{48}$  at Yap, are consistent with the difference between model analysis and forecast at the three eastern stations. Even though the upper tropospheric temperature signals are not discernible, a schematic diagram for the vertical structure at these western stations is given in Fig. 42b for comparison with the other stations.

## 8. Velocity potential structure

It would be interesting to determine the propagating structure of the divergence field associated with the 5-day oscillations. However, the divergence itself normally contains substantial small-scale, often very noisy, features, so the velocity potential is used in the analysis. The velocity potential is computed following the procedure discussed by Boyle and Chang (1984). Because it is equivalent to a field that is approximately proportional to the spatially-smoothed divergence, it may only represent scales that are larger than the synoptic disturbances. Since the divergent component of the motion is usually not well observed, the divergence contained in the objective analysis of NWP systems is normally heavily influenced by the model forecast through the four-dimensional data assimilation (Trenberth, 1992). Comparison with a non-NWP assimilated data set indicates that the assimilated data tends to smear out smaller scale features in the velocity potential field (Chang et al 1991). Thus the divergence field associated with the tropical synoptic scale disturbances is under-represented in the velocity potential. Nevertheless, the horizontal structure of the velocity potential is determined using the inter-x and inter-y cross spectral analyses mainly to compare the  $\tau_{48}$  forecasts with the  $\tau_{00}$  analyses within the 5-day band, which should be relevant to the evaluation of the forecast for the planetary scale that seems to dominate the equatorial region. The  $150^{\circ}\text{E}$  and  $10^{\circ}\text{N}$  are again used as the base longitude and base latitude, respectively.

### a. Longitudinal cross spectra of velocity potential

The 850 hPa velocity potential inter-x cross spectra shown in Fig. 43a shows a planetary scale eastward propagation pattern

extending from the northern boundary southward to cover most of the northern tropics. Westward propagation, with a very large zonal scale, can only be seen at the equator and to the south. Thus any divergence field associated with the 5-day synoptic easterly wave disturbances observed in the  $v_{850}$ , which shows westward propagation at and south of  $15^{\circ}\text{N}$  (Fig. 27a), is apparently masked by the midlatitude-based eastward propagating divergence system north of the equator. The southern equatorial westward propagating velocity potential pattern also possesses a much larger zonal scale than the wavenumber-three waves observed in the  $u_{850}$  time series there.

Fig. 43b shows the inter-x structure of the  $\tau_{48}$  velocity potential at 850 hPa. It is a good reproduction of  $\tau_{00}$ , probably more a result of the fact that  $\tau_{00}$  is substantially influenced by the model forecast than a good 48-h forecast of the actual field. The difference between Figs. 43a and 43b is mainly in the equatorial latitudes, where the coherence over the South China Sea is increased. A larger (quarter-cycle) phase difference between the western Indonesia region and  $150^{\circ}\text{E}$  indicates that the westward propagating waves have a wavenumber two zonal scale, which is shorter than that indicated by the  $\tau_{00}$  analysis in Fig. 43a.

The inter-x structure of the  $\tau_{00}$  velocity potential at 200 hPa is shown in Fig. 44a. Here the indicated zonal scales are comparable to those shown at 850 hPa, but the westward propagating pattern is identifiable in the tropical band south of  $15^{\circ}\text{N}$ . Thus at the 5-day frequency band, the region between the equator and  $15^{\circ}\text{N}$  is dominated by an eastward propagating midlatitude divergence system in the lower troposphere, and by a westward propagating tropical divergence system in the upper troposphere. Fig. 44b, which is the inter-x structure of  $\tau_{48}$  velocity potential at 200 hPa, indicates that the upper tropospheric pattern is well forecasted north of the equator

only. In the southern equatorial region, the westward propagation is poorly represented, particularly toward the east of  $150^{\circ}\text{E}$  where the phase vector indicates a slight eastward propagation.

#### b. Meridional cross spectra of velocity potential

The  $\tau_{00}$  velocity potential inter- $y$  cross spectra at 850 hPa (Fig. 45a) demonstrate high coherence values throughout the domain, indicating that the 5-day fluctuations are of a very large north-south scale. Again, this is characteristic of four-dimensional assimilated data where the divergence field is significantly affected by the numerical model forecast. Over the tropical western Pacific between the equator and  $20^{\circ}\text{N}$ , the fluctuations are in phase. Outside of this region, the meridional tilt is predominately northeast-southwest. This is true in the southern equatorial region also, where the negative phase vectors imply a northeast-southwest tilt because the zonal propagation is westward (Fig. 43a). Another view of this is simply that there is a phase propagation southward throughout the domain. Since this is occurring at the synoptic timescale, it may be a manifestation of the southward cold surges from the East Asian continent observed in the northeast monsoon region (Chang et al, 1983, Chang and Chen, 1992, Chang et al. 1993). The fact that the southward propagation can be found south of the equator indicates that the cold surge associated convergence can penetrate into the southern hemisphere. This general structure is reproduced by the  $\tau_{48}$  850 hPa velocity potential (Fig. 45b).

The  $\tau_{00}$  velocity potential at 200 hPa (Fig. 46a) shows a meridional structure that is different from that at 850 hPa. In the northern eastward-propagation region east of  $120^{\circ}\text{E}$ , the tilt is predominantly northwest-southeast, which is opposite to the 850 hPa structure. South of  $10^{\circ}\text{N}$  in the westward-propagation

region east of 120°E, the tilt is northeast-southwest, again opposite to the 850 hPa structure. The two regions combine to show a northward propagation throughout the domain. Previous studies of winter monsoon cold surges (Chang and Lau, 1982, Chang and Chen, 1992) reported enhancement of upper tropospheric northward divergent wind following each cold surge event. The present result indicates that the divergence field itself is propagating northward at the synoptic timescale.

The meridional tilts or propagation almost disappear entirely in the r48 time series (Fig. 46b). This difference between the r48 and r00 200 hPa velocity potential is somewhat surprising, since one would expect that the four-dimensional assimilation process would strongly influence the divergence field of the model forecast. It appears that in this case the analyzed r00 divergence field contains observed information in the meridional structure that is independent from the model forecast, and that the forecast divergence is unable to reproduce this information.

#### **9. A proposed scheme to evaluate systematic errors in model analysis and forecast of tropical disturbances**

The previous sections show that time series analysis may be used to evaluate a model's ability to represent tropical disturbances during a season. In order to simplify the evaluations, we propose a scheme to use spectral characteristics to measure the systematic errors of a NWP model with respect to the climatology of the tropical oscillations within a given season. The scheme includes three error parameters, all for a pre-selected frequency band. The model output climatology may be the analysis or the forecast, and the verification climatology may be the radiosonde observations or the analysis.

1) Coherence square (Coh2): This is simply the coherence square between the model output time series (analysis or forecast) and

the verification time series. The higher the Coh2, the more correlation between model output and verification.

2) Variance difference (VDif): This measures the errors in estimating the amplitude of the oscillations:

$$VDif = 2\pi \times \Delta f \times 2^{\frac{1}{2}} [(\Sigma V_m)^{\frac{1}{2}} - (\Sigma V_v)^{\frac{1}{2}}] / n,$$

Here  $\Delta f$  is the frequency interval in the spectral analysis,  $\Sigma V_m$  is the summation of variance (power) at each frequency point within the frequency band for the model output time series,  $\Sigma V_v$  is the summation of variance at each frequency point for the verification time series, and  $n$  is the number of frequency points within the frequency band. A positive VDIF indicates that the model output overestimates, and vice versa. A smaller VDIF indicates a more accurate amplitude estimate of the oscillations.

3) Phase shift (PS): This measures the phase shift between the model output and the verification:

$$PS = \Delta\phi \times \bar{P}$$

Here  $\Delta\phi$  is the phase difference in cycles ( $^{\circ}/360^{\circ}$ ), and  $\bar{P}$  is the averaged period within the frequency band. Thus PS gives the phase difference in time units. A smaller PS is more accurate.

The scores for u and v components for the 5-day band at 200 hPa and 850 hPa are computed at each grid point closest to a verifying radiosonde station. Figs. 47-50 show the results from  $\tau_{00}$  to  $\tau_{72}$  at 24 h intervals for each of the stations in the Caroline Island region, with the averages computed using root mean squares. In general, the coherence squares show clearly a degradation with time. At 200 hPa the average CH2 decreases from about 0.6-0.7 at  $\tau_{00}$  to less than 0.2 for both u (Fig. 47)

and v (Fig. 48), with the largest decline occurring during the first 24 hrs. At 850 hPa the values are generally higher, with the average CH2 declining from 0.8 to near 0.5 for both u and v (Figs. 49-50, respectively), indicating that the model analysis and forecast retain much more the observed synoptic oscillation climatology in the lower troposphere than the upper troposphere.

Because root mean squares are used, the average variance difference and phase shift are both positive. (Yap is excluded from the average VDif due to the large discrepancies between r00 and RAOB v<sub>850</sub>.) Individual station VDif scores show that at 200 hPa there is a tendency of decreasing variance in the model outputs such that by r72 the u and v model climatology has an amplitude about 1.5 m/s less than observed. The change at 850 hPa is less systematic. The phase shift varies greatly among the stations. At 200 hPa the u results (Fig. 47) show that the two western stations (Koror and Yap) have a positive phase error at r48 and r72 of around 0.5 day, while the four eastern stations show negative phase errors average about -0.5 day. Other diagrams have less systematic patterns.

#### 10. Summary and concluding remarks

In this study we use spectral analysis to diagnose the structure of synoptic timescale wave disturbances over the tropical western North Pacific during the 1991-1992 winter with three data sets. The data are the radiosonde observations in the vicinity of the Caroline Islands, and the initial (r00) analyzed and the 48-h (r48) forecast fields from the Navy Operational Global Atmospheric Prediction System (NOGAPS). The primary purpose is to evaluate the ability of the model analysis and forecast to represent the characteristics of the tropical synoptic disturbances within a frequency band centered at (5 day)<sup>-1</sup>. This is done through a comparison of the wave climatologies produced by the r00 and r48 model data with that



determined from radiosonde data. The comparison of the r00 and r48 model climatologies also allows a study of the model's systematic errors in representing tropical synoptic disturbances.

As is the case with many previous time series analyses of tropical synoptic disturbances, oscillations in the meridional wind component, especially at 850 hPa, are used as the main indicator of disturbance activity. In many cases two spectral power "peaks" are found in the v850 radiosonde data: a low-frequency concentration of power encompassing the seasonal and intra-seasonal oscillations, and a synoptic peak centered around five days that is the focus of this study. While the r00 data, in general, resemble reasonably well the spectral distribution of the radiosonde results, the r48 forecast often has markedly larger discrepancies. On the other hand, cross-spectral analysis of the meridional wind time series in the horizontal domain demonstrates good agreement on the general structure of the synoptic waves among the r00 analysis, the r48 forecast and the radiosonde observations. As examples:

- 1) Based on the time series of meridional wind component at 850 hPa, the synoptic easterly (westward propagating) waves are well defined in the 135°E-180° region in both the radiosonde and the model data. The wavelength is  $\approx 33^\circ$  along 10°N and somewhat longer (38°) along the equator. These observed characteristics are very well represented by both the r00 analysis and the r48 forecast.

- 2) For regions south of 20°N in the western Pacific, the easterly waves exhibit a northeast-southwest tilt in the r00 v850 field, a feature frequently observed by previous studies based on radiosonde data. This is well reproduced by the r48 v850 time series.

3) The  $r_{00} v$  at 200 hPa shows an easterly propagating wavelength of 50-60° longitude, which is reasonably reproduced by the  $r_{48} v_{200}$  data.

The horizontal cross spectra in both the  $u$  component and the velocity potential are different from the  $v$  component results. The synoptic wave structure is not clear in the  $u$  time series, which has longer zonal scales. The  $r_{00}$  data show a westward-propagating wavelength near wavenumber three for the 5-day oscillations in the equatorial zone at both 850 and 200 hPa. This wavelength is reproduced by  $r_{48} u$  only at 850 hPa. At 200 hPa, the  $r_{48} u$  gives an almost in-phase relationship across all longitudes in the equatorial belt. Similarly, at the 5-day time scale, the analyzed velocity potential field is of a larger spatial scale than the synoptic scale shown by the  $v$  data. The implied large-scale divergence propagates southward at 850 hPa and northward at 200 hPa, both of which appear to be manifestations of the winter monsoon cold surges observed by Chang and Chen (1992). The  $r_{48}$  forecast can reproduce only the southward propagation at 850 hPa. It is unable to reproduce the northward propagation of the upper-level divergent flow. Since the synoptic timescale upper-level divergent return flow has been found to be related to the acceleration of the East Asian jet streak (Chang and Lau, 1982; Chang and Lum, 1984), this inability may cause the model to underforecast the strengthening of midlatitude baroclinic systems.

The vertical structure of the 5-day wave disturbances in the Caroline Islands determined from the  $r_{00}$  data is in good agreement with that determined from the radiosonde reports. In the eastern part of the station network the disturbances have very little vertical tilt in the lower troposphere, in agreement with the structure observed there previously by Wallace and Chang (1969). In the upper troposphere they show a westward tilt with height, which is in agreement with the

upper-tropospheric structure observed in the central Pacific during the northern summer by Chang et al. (1970), although these central Pacific waves have a strong eastward tilt with height in the lower troposphere. In the western part of the station network near Yap and Koror there is a eastward tilt with height from lower to upper troposphere. This is opposite to the vertical tilt observed by Chang et al. (1970) for these stations during summer of 1964. However, the effect of the vertical shear of the time-mean zonal wind (Holton, 1970; Chang and Miller, 1977; and Shapiro et al, 1988) can be used to interpret this difference consistently as a result of the difference between the winter-northeast and summer-southwest monsoons. This difference is most pronounced in the lower troposphere, and over the western part of the western Pacific.

West of  $160^{\circ}\text{E}$  between the equator and  $10^{\circ}\text{N}$ , the r48 times series tend to produce too strong a wave structure downstream from a region where vertically-organized oscillation is observed. This may be due to the equatorial dynamics contained within the model that in some way propagates the observed wave structure downstream into a region where it does not exist. It is fortunate that we have reliable radiosonde stations in the Caroline Island region to verify the analysis. Namely, we can ascertain that 1) the forecast climatology is artificial, and 2) the analysis climatology incorporates observed data to correct the model forecast first guess. In fact, the r00 to r48 westward shift of the maximum coherence between  $v_{200} - v_{300}$  is approximately  $17.5^{\circ}$  longitude (Fig. 39). This is only slightly slower than the phase propagation speed indicated by the  $v_{200}$  zonal cross spectra, which is  $50^{\circ}$  longitude per five days, or about  $20^{\circ}$  per 48 h. For the lower levels the westward shift is about one-third less, corresponding to the fact that the propagation speed at 850 hPa is slower, at  $33^{\circ}$  per five days.

It is possible that this problem of artificial generation or propagation of equatorial waves by the numerical models may occur elsewhere in the tropics and during other seasons. Because of lack of conventional data, many tropical studies use four-dimensionally assimilated data that are analyzed by operational NWP models. This use of model analysis as real data is especially risky over a data void region, since any model-generated equatorial wave structure will most likely be present in the analysis data as they cannot be corrected by real observations.

The 5-day wave is shown to be warm core above the 850 hPa trough in the middle upper troposphere. Therefore it may be self-sustaining energetically if synoptic-scale rising motion is in phase with the low-level trough. However, the  $\tau 00$  analysis and the  $\tau 48$  forecast climatologies give different thermal structures near the surface, with the former showing a warm core and the latter showing a cold core. This rather dramatic difference is perhaps due to the model's cumulus and boundary layer parameterizations that produce a cold core near the surface. Several model mechanisms that may be involved are suggested. They include a higher level of cloud base formed by a large-scale process and thus some artificial adiabatic cooling below, over-intense rainfalls that re-evaporate in the boundary layer, or too strong a lower boundary dissipation effect.

The zonal velocity component and velocity potential both show a much larger wavelength for the 5-day oscillations than that deduced from  $v_{850}$ , so the synoptic spatial-scale disturbances are masked by the planetary scales in these fields. For  $\tau 00$ , the velocity potential over the northern tropical western Pacific and the Southeast Asia shows a southward propagation at 850 hPa and a northward propagation at 200 hPa. The low-level propagation can be traced to the southern tropics. This pattern appears to be related to the acceleration of the East Asian

local Hadley cell during winter monsoon cold surges suggested by Chang and Lau (1982). In the r48 forecast climatology, the low-level propagation is represented, but the upper level poleward propagation is missing.

Based on the study of the spectral and cross-spectral characteristics, a scheme to quantify the systematic errors in tropical oscillations in the NWP analysis and forecast is proposed. The scheme uses three scores to measure the errors: the coherence square, the variance difference, and the phase shift, between the oscillation climatology of the model output (analysis or forecast) and that of the verification (radiosonde observation or analysis). For the period of study the loss of coherence with time is most visible, especially at 200 hPa where the coherence square with radiosonde observations decreases from around 0.7 at r00 to less than 0.2 at r72. At 850 hPa the model climatology has considerably higher coherence square with the observations, decreasing from about 0.8 at r00 to 0.5 at r72.

#### **Acknowledgments**

This work was supported in part by the Naval Research Laboratory, Marine Meteorology Division, and by the National Science Foundation, Division of Atmospheric Sciences. The second author is supported by the Fleet Numerical Oceanography Center. We wish to thank Drs. Tom Rosmond, Teddy Holt, Pat Harr and J.M. Chen for discussions.

## REFERENCES

- Boyle, J. S. and C.-P. Chang, 1984: Monthly and seasonal climatology over the global tropics and subtropics for the decade 1973 to 1983. Vol. I. 200 mb winds. *Naval Postgrad. Sch. Tech. Rept. 63-84-006*, 172pp.
- Burpee, R. W., 1972: The origin and structure of easterly waves in the lower troposphere of north Africa. *J. Atmos. Sci.*, **29**, 7-90.
- \_\_\_\_\_, R. W., 1974: Characteristics of north African waves during the summers of 1968 and 1969. *J. Atmos. Sci.*, **31**, 1556-1570.
- Chang, C.-P., V. F. Morris and J. M. Wallace, 1970: A statistical study of easterly waves in the western Pacific, July-December 1964. *J. Atmos. Sci.*, **31**, 1556-1570.
- \_\_\_\_\_, C. R. Miller, 1977: Comparison of easterly waves in the tropical Pacific during two contrasting periods of sea surface temperature anomalies. *J. Atmos. Sci.*, **34**, 615-628.
- \_\_\_\_\_, and K. M. Lau, 1982: Short-term planetary scale interactions over the tropics and midlatitude during northern winter. Part I: Contrasts between active and inactive periods. *Mon. Wea. Rev.*, **110**, 933-946.
- \_\_\_\_\_, and H. Lim, 1982: On the effects of viscous damping on equatorial Rossby waves. *J. Atmos. Sci.*, **39**, 1726-1733.
- \_\_\_\_\_, and K. G. Lum, 1985: Tropical-midlatitude interactions over Asia and the western Pacific during the 1983-84 northern winter. *Mon. Wea. Rev.*, **113**, 1345-1358.
- \_\_\_\_\_, M. S. Peng and J. S. Boyle, 1991: Interannual variations of tropical upper tropospheric divergence and Pacific teleconnections during northern winter. *Terrestr., Atmos. Ocean. Sci.*, **1**, 337-362.
- \_\_\_\_\_, and J.M. Chen, 1992: A statistical study of winter monsoon cold surges over the South China Sea and the

- large-scale equatorial divergence. *J. Meteor Soc. Japan*, 70, 287-302 .
- Liebmann B. and H. H. Hendon, 1990: Synoptic-scale disturbances near the equator. *J. Atmos. Sci.*, 47, 1463-1479.
- Hogan T. F. and T. E. Rosmond, 1991: The description of the Navy Operational Global Atmospheric Prediction System's spectral forecast model. *Mon. Wea. Rev.*, 119, 1786-1815.
- Holton, J. R. 1971: A diagnostic model for equatorial wave disturbances: The role of vertical shear of the mean zonal wind. *J. Atmos. Sci.*, 29, 55-64.
- Lau, K.-H. and N.-G. Lau, 1990: Observed structure and propagation characteristics of tropical summertime synoptic scale disturbance. *Mon. Wea. Rev.*, 118, 1888-1913.
- Reed, R. J. and E. E. Recker, 1971: Structure and properties of synoptic-scale wave disturbances in the equatorial western Pacific. *J. Atmos. Sci.*, 28, 1117-1133.
- \_\_\_\_\_, D. C. Norquist, and E. E. Recker, 1977: The structure and properties of African wave disturbances in the equatorial western Pacific. *Mon. Wea. Rev.*, 105, 317-333.
- \_\_\_\_\_, E. Klinker and A. Hollingsworth, 1988: The structure and characteristics of African easterly wave disturbances as determined from the ECMWF operational analysis/forecast system. *Meteor. Atmos. Phys.*, 38, 22-33.
- Shapiro, L. J., D. E. Stevens and P. E. Clesielski, 1988: A comparison of observed and model-derived structures of Caribbean easterly waves. *Mon. Wea. Rev.*, 116, 921-938.
- Swett, C.W., 1993: Spectral analysis of synoptic time scale disturbances over the tropical eastern Pacific during summer 1989, 1990 and 1991. *M.S. thesis*, Dept. of Meteorology, Navy Postgraduate School, 85pp.
- Trenberth, K. E., 1992: Global analysis from ECMWF. *NCAR Technical Note*, TN-373, 191pp.

Wallace, J. M. and C.-P. Chang, 1969: Spectrum analysis of large-scale wave disturbances in the tropical lower troposphere. *J. Atmos. Sci.*, **26**, 1010-1025.

Yanai, M., T. Maruyama, T. Nitta and Y. Hyashi, 1968: Power spectra of large-scale disturbances over the tropical Pacific. *J. Meteor Soc. Japan*, **46**, 308-323.



## Figure Captions

Fig. 1. Comparison of  $v_{850}$  spectra at Majuro: a) relative power spectra for RAOB (thick), NOGAPS  $\tau_{00}$  (thin) and NOGAPS  $\tau_{48}$  (dashed), b) phase difference (line) and coherence square (square) between RAOB and  $\tau_{00}$ , c) phase difference (line) and coherence square (square) between RAOB and  $\tau_{48}$ .

Fig. 2. Same as Fig. 1 except for Ponape.

Fig. 3. Same as Fig. 1 except for Truk.

Fig. 4. Same as Fig. 1 except for Guam

Fig. 5. Same as Fig. 1 except for Yap.

Fig. 6. Same as Fig. 1 except for Koror.

Fig. 7. Comparison of  $u_{850}$  spectra at Majuro: a) relative power spectra for RAOB (thick),  $\tau_{00}$  (thin) and  $\tau_{48}$  (dashed), b) phase difference (line) and coherence square (square) between RAOB and  $\tau_{00}$ , c) phase difference (line) and coherence square (square) between RAOB and  $\tau_{48}$ .

Fig. 8. Same as Fig. 7 except for Ponape.

Fig. 9. Same as Fig. 7 except for Truk.

Fig. 10. Same as Fig. 7 except for Guam

Fig. 11. Same as Fig. 7 except for Yap.

Fig. 12. Same as Fig. 7 except for Koror.

Fig. 13. Comparison of  $v_{200}$  spectra at Majuro: a) relative power spectra for RAOB (thick),  $\tau_{00}$  (thin) and  $\tau_{48}$  (dashed), b) phase difference (line) and coherence square (square) between RAOB and  $\tau_{00}$ , c) phase difference (line) and coherence square (square) between RAOB and  $\tau_{48}$ .

Fig. 14. Same as Fig. 13 except for Ponape.

Fig. 15. Same as Fig. 13 except for Truk.

Fig. 16. Same as Fig. 13 except for Guam

Fig. 17. Same as Fig. 13 except for Yap.

Fig. 18. Same as Fig. 13 except for Koror.

Fig. 19. Comparison of  $u_{200}$  spectra at Majuro: a) relative power spectra for RAOB (thick),  $\tau_{00}$  (thin) and  $\tau_{48}$  (dashed), b) phase difference (line) and coherence square (square) between RAOB and  $\tau_{00}$ , c) phase difference (line) and coherence square (square) between RAOB and  $\tau_{48}$ .

Fig. 20. Same as Fig. 19 except for Ponape.

Fig. 21. Same as Fig. 19 except for Truk.

Fig. 22. Same as Fig. 19 except for Guam

Fig. 23. Same as Fig. 19 except for Yap.

Fig. 24. Same as Fig. 19 except for Koror.

Fig. 25. Phase difference (line) and coherence square (square) of  $\tau_{00}$   $v_{850}$  between Truk as the base series and Majuro (M), Ponape (P), Guam (G), Yap (Y) and Koror (K) for: a) 4.6-day, b) 5.3-day, and c) 6.4-day periods.

Fig. 26. Same as Fig. 25 except for  $\tau_{48}$   $v_{850}$ .

Fig. 27. Inter-longitude cross spectra for the synoptic band (averaged period 5.3 days) for  $v_{850}$  with the  $150^\circ\text{E}$  data as the base series longitude. The phase difference and coherence square between each grid point and the base series at the same latitude are plotted as a vector, with the direction indicating phase difference (northward pointing =  $0^\circ$ , increasing clockwise), and the magnitude indicating coherence square: a)  $\tau_{00}$ , and b)  $\tau_{48}$ . The location of the Caroline Island radiosonde stations are indicated with the first letter of the station name.

Fig. 28. Inter-longitude cross spectra, same as Fig. 27 except for  $u_{850}$ .

Fig. 29. Inter-longitude cross spectra, same as Fig. 27 except for  $v_{200}$ .

- Fig. 30. Inter-longitude cross spectra, same as Fig. 27 except for  $u_{200}$ .
- Fig. 31. Inter-latitude cross spectra for the synoptic band (averaged period 5.3 days) for  $v_{850}$  with the  $10^{\circ}N$  data as the base series latitude. The phase difference and coherence square between each grid point and the base series at the same longitude are plotted as a vector, with the direction indicating phase difference (northward pointing =  $0^{\circ}$ , increasing clockwise), and the magnitude indicating coherence square: a)  $\tau_{00}$ , and b)  $\tau_{48}$ .
- Fig. 32. Inter-latitude cross spectra, same as Fig. 31 except for  $u_{850}$ .
- Fig. 33. Inter-latitude cross spectra, same as Fig. 31 except for  $v_{200}$ .
- Fig. 34. Inter-latitude cross spectra, same as Fig. 31 except for  $u_{200}$ .
- Fig. 35. Inter-level cross spectra for the synoptic band (averaged period 5.3 days) between  $v_{850}$  (base series) -  $v_{700}$ . The phase difference and coherence square between the two series at each grid point are plotted as a vector, with the direction indicating phase difference (northward pointing =  $0^{\circ}$ , increasing clockwise), and the magnitude indicating coherence square: a)  $\tau_{00}$ , and b)  $\tau_{48}$ .
- Fig. 36. Inter-level cross spectra, same as Fig. 35 except for  $v_{850}$  -  $v_{500}$ .
- Fig. 37. Inter-level cross spectra, same as Fig. 35 except for  $v_{850}$  -  $v_{300}$ .
- Fig. 38. Inter-level cross spectra, same as Fig. 35 except for  $v_{850}$  -  $v_{200}$ .
- Fig. 39. Inter-level cross spectra, same as Fig. 35 except for  $v_{200}$  (base series) -  $v_{300}$ .

Fig. 40. Comparisons between RAOB, r00 and r48 inter-level coherence squares ( $v_{850}$  as the base series vs.  $v$  at other levels) for the 5.3-day synoptic band. See text for details.

Fig. 41. Inter-level cross spectra, same as Fig. 35 except for r24: a)  $v_{850} - v_{300}$ , and b)  $v_{850} - v_{200}$ .

Fig. 42. Schematic diagram for the vertical structure of the 5.3-day synoptic wave at a) eastern stations: Majuro, Ponape and Truk; and b) western stations: Guam, Yap and Koror. R-ridge axis, T-trough axis, W-warm, C-cold.

Fig. 43. Inter-longitude cross spectra, same as Fig. 27 except for the velocity potential at 850 hPa.

Fig. 44. Inter-longitude cross spectra, same as Fig. 27 except for the velocity potential at 200 hPa.

Fig. 45. Inter-latitude cross spectra, same as Fig. 31 except for the velocity potential at 850 hPa.

Fig. 46. Inter-latitude cross spectra, same as Fig. 31 except for the velocity potential at 200 hPa.

Fig. 47. The coherence square, variance difference and phase shift error scores band between RAOB and model outputs (r00, r24, r48, r72) for the 5.3-day synoptic band  $u_{200}$  at grid points closest to each of the radiosonde stations. The averages of these points are also plotted.

Fig. 48. Same as Fig. 47 except for  $v_{200}$ .

Fig. 49. Same as Fig. 47 except for  $u_{850}$ , and the averages do not include Yap.

Fig. 50. Same as Fig. 47 except for  $v_{850}$ , and the averages do not include Yap.

MAJURO ( 7.1N,171.4E)  
 PARAMETER = 850 MB MERIDIONAL WIND  
 91111200 - 92031812  
 COVERAGE = 90%

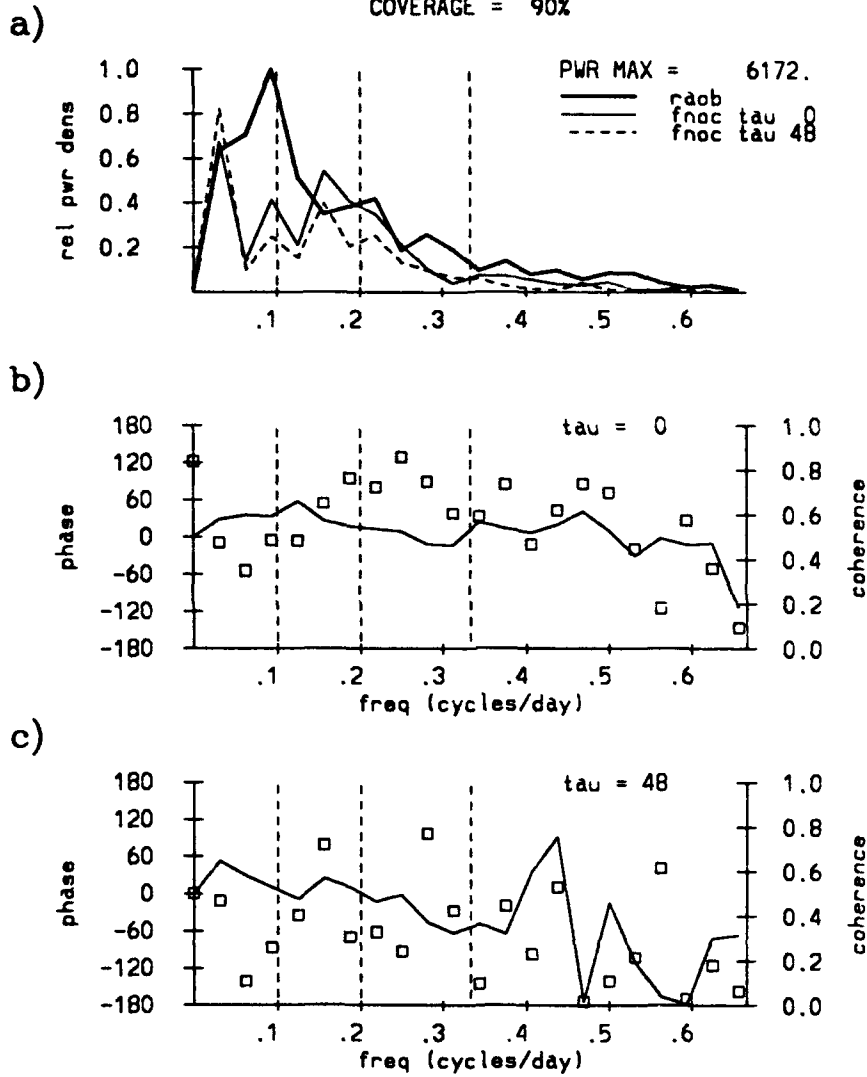


Fig. 1. Comparison of  $v_{850}$  spectra at Majuro: a) relative power spectra for RAOB (thick), NOGAPS  $\tau_{00}$  (thin) and NOGAPS  $\tau_{48}$  (dashed), b) phase difference (line) and coherence square (square) between RAOB and  $\tau_{00}$ , c) phase difference (line) and coherence square (square) between RAOB and  $\tau_{48}$ .

PONAPE ( 7.0N,158.2E)  
 PARAMETER = 850 MB MERIDIONAL WIND  
 91111200 - 92031812  
 COVERAGE = 84%

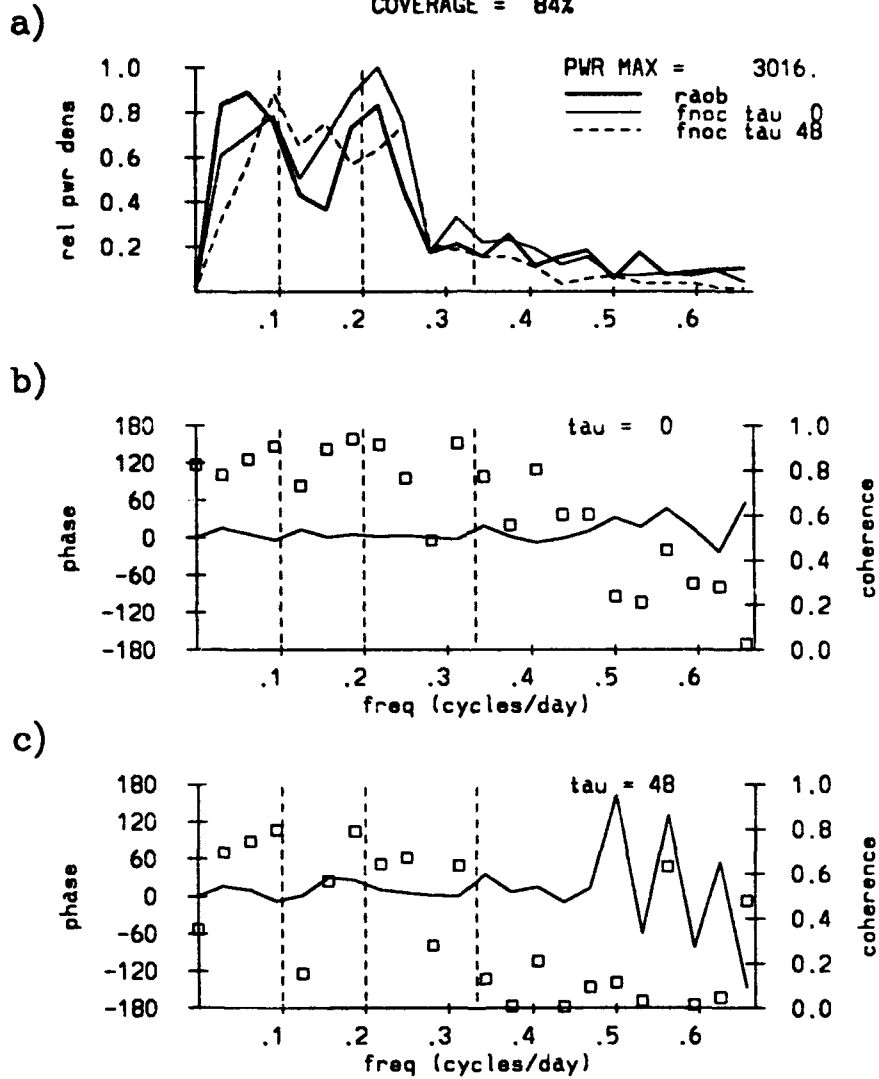


Fig. 2. Same as Fig. 1 except for Ponape.

TRUK ( 7.5N,151.9E)  
 PARAMETER = 850 MB MERIDIONAL WIND  
 91111200 - 92031812  
 COVERAGE = 91%

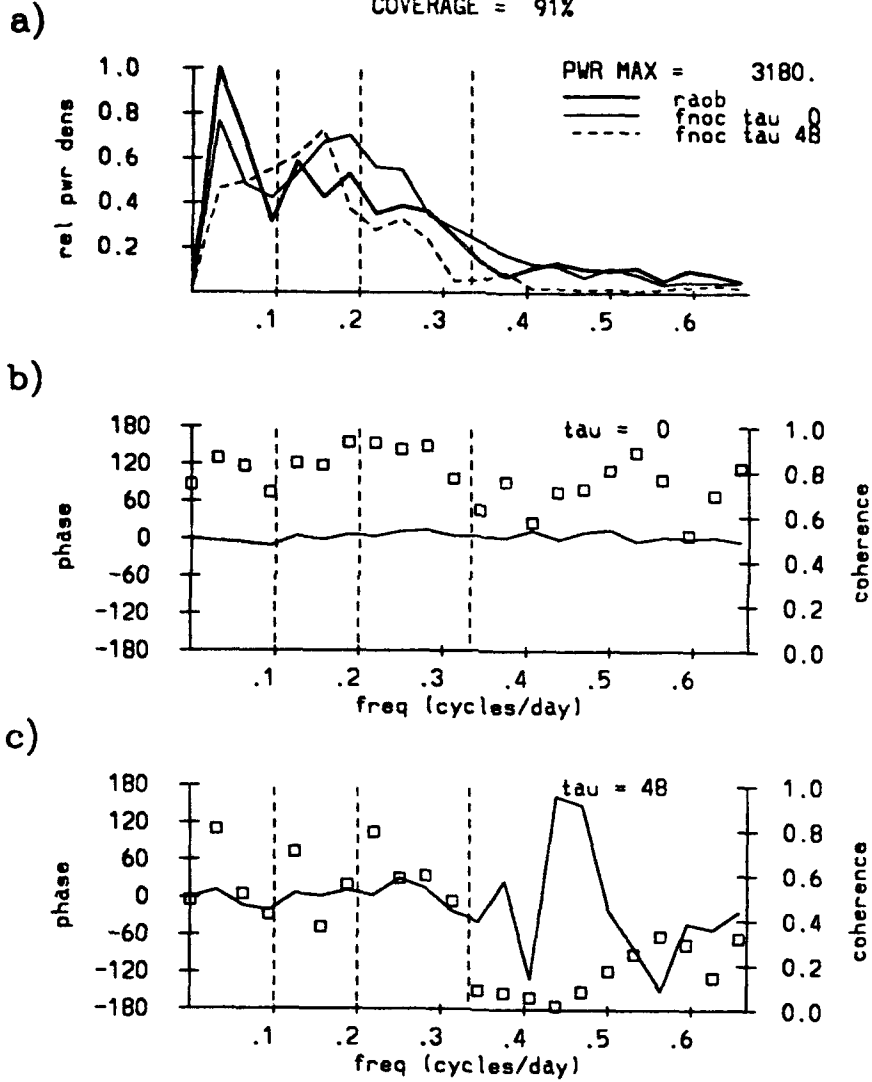


Fig. 3. Same as Fig. 1 except for Truk.

GUAM (13.6N,144.8E)  
 PARAMETER = 850 MB MERIDIONAL WIND  
 91111200 - 92031812  
 COVERAGE = 90%

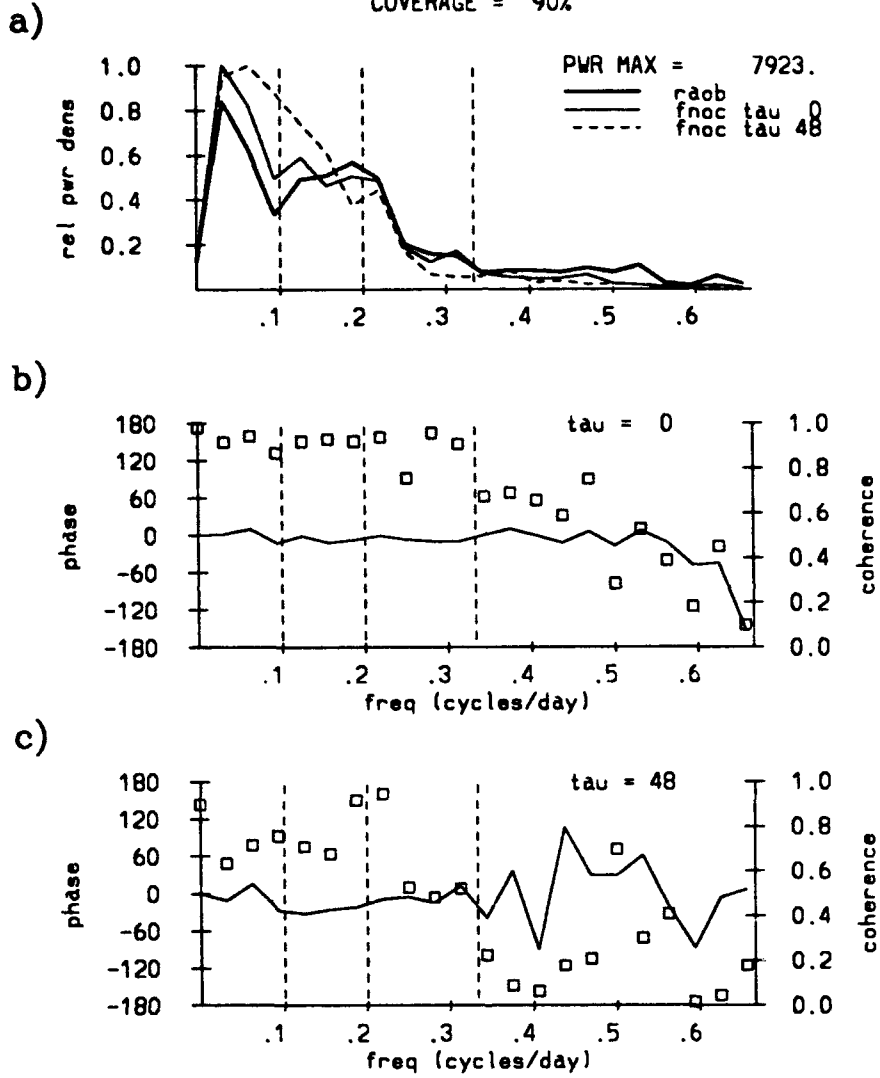


Fig. 4. Same as Fig. 1 except for Guam



YAP ( 9.5N,138.1E)  
 PARAMETER = 850 MB MERIDIONAL WIND  
 91111200 - 92031812  
 COVERAGE = 90%

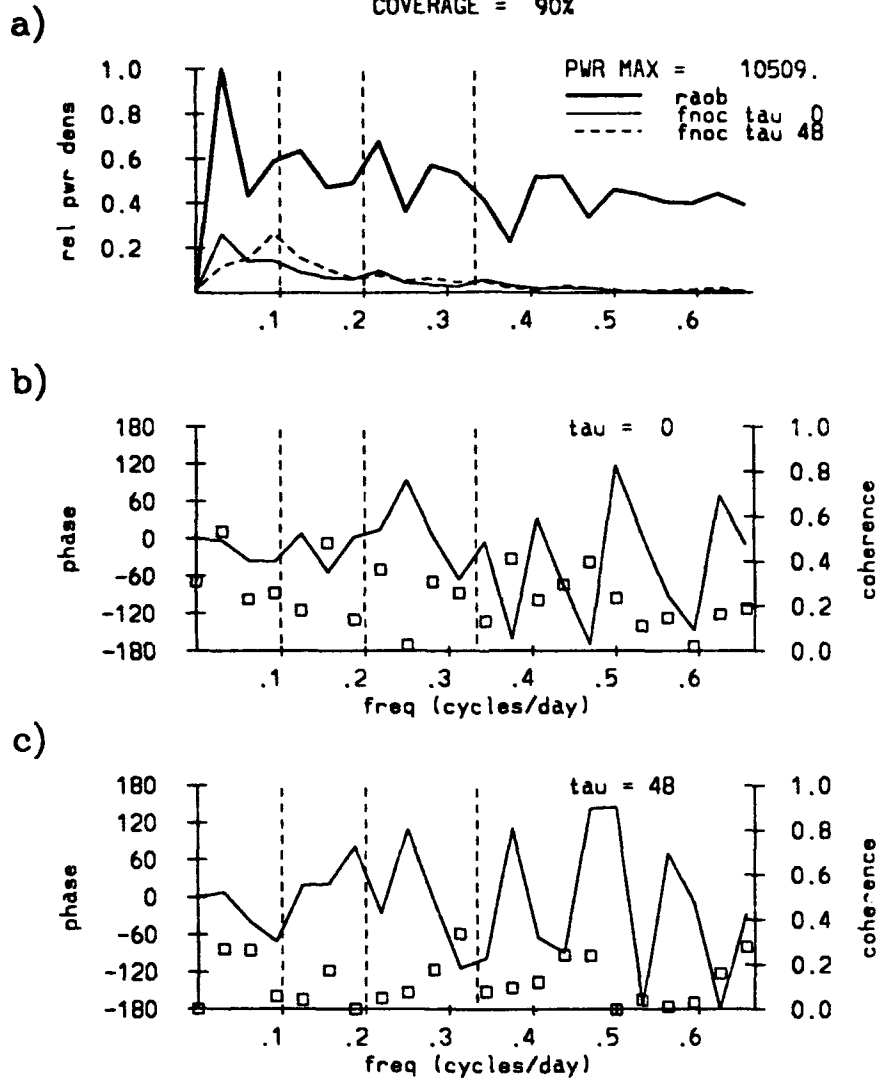


Fig. 5. Same as Fig. 1 except for Yap.

KOROR ( 7.3N,134.5E)  
 PARAMETER = 850 MB MERIDIONAL WIND  
 91111200 - 92031812  
 COVERAGE = 82%

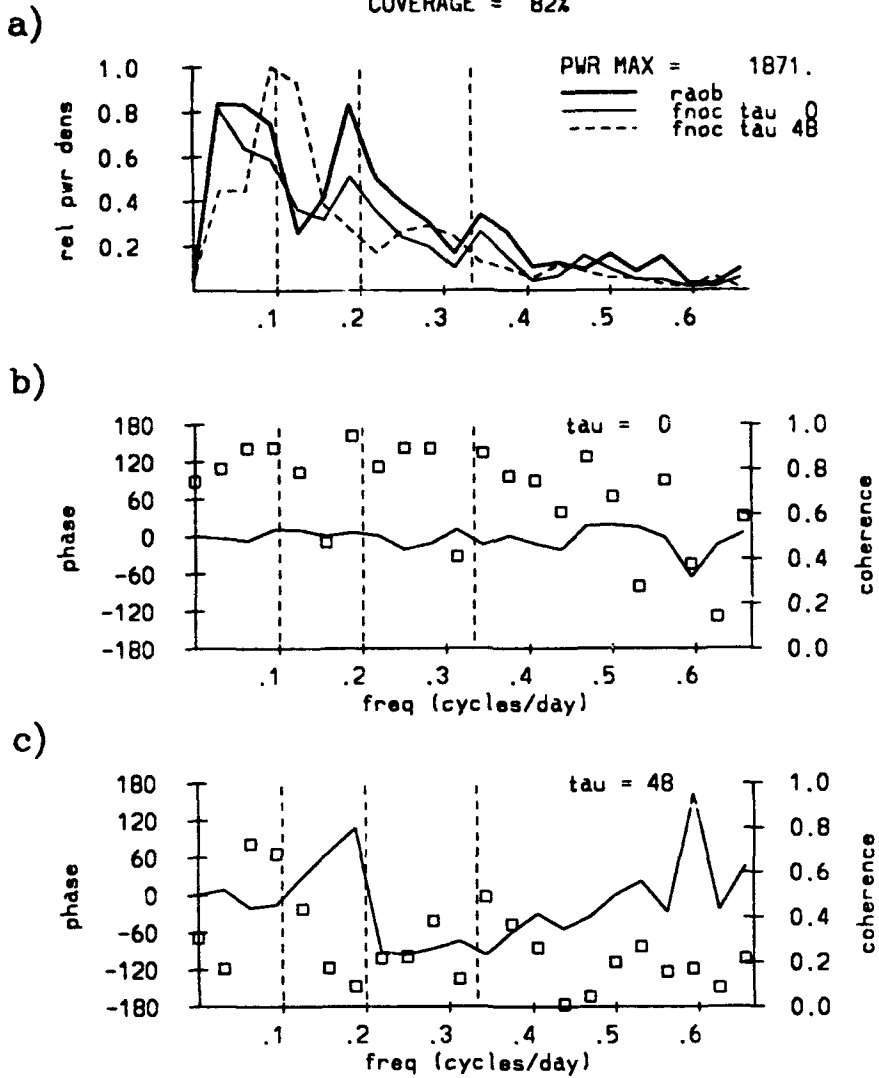


Fig. 6. Same as Fig. 1 except for Koror.

MAJURO ( 7.1N,171.4E)  
 PARAMETER = 850 MB ZONAL WIND  
 91111200 - 92031812  
 COVERAGE = 90%

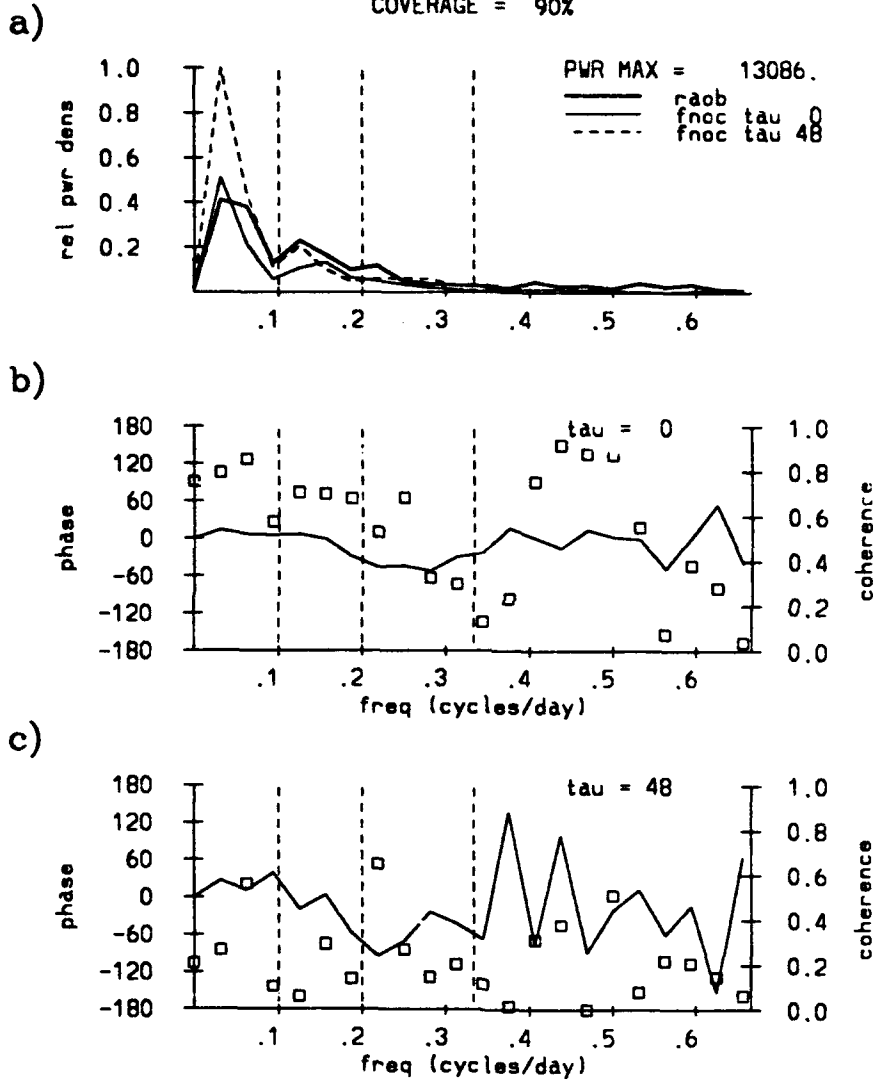


Fig. 7. Comparison of  $u_{850}$  spectra at Majuro: a) relative power spectra for RAOB (thick),  $\tau_{00}$  (thin) and  $\tau_{48}$  (dashed), b) phase difference (line) and coherence square (square) between RAOB and  $\tau_{00}$ , c) phase difference (line) and coherence square (square) between RAOB and  $\tau_{48}$ .

PONAPE ( 7.0N,158.2E)  
 PARAMETER = 850 MB ZONAL WIND  
 91111200 - 92031812  
 COVERAGE = 84%

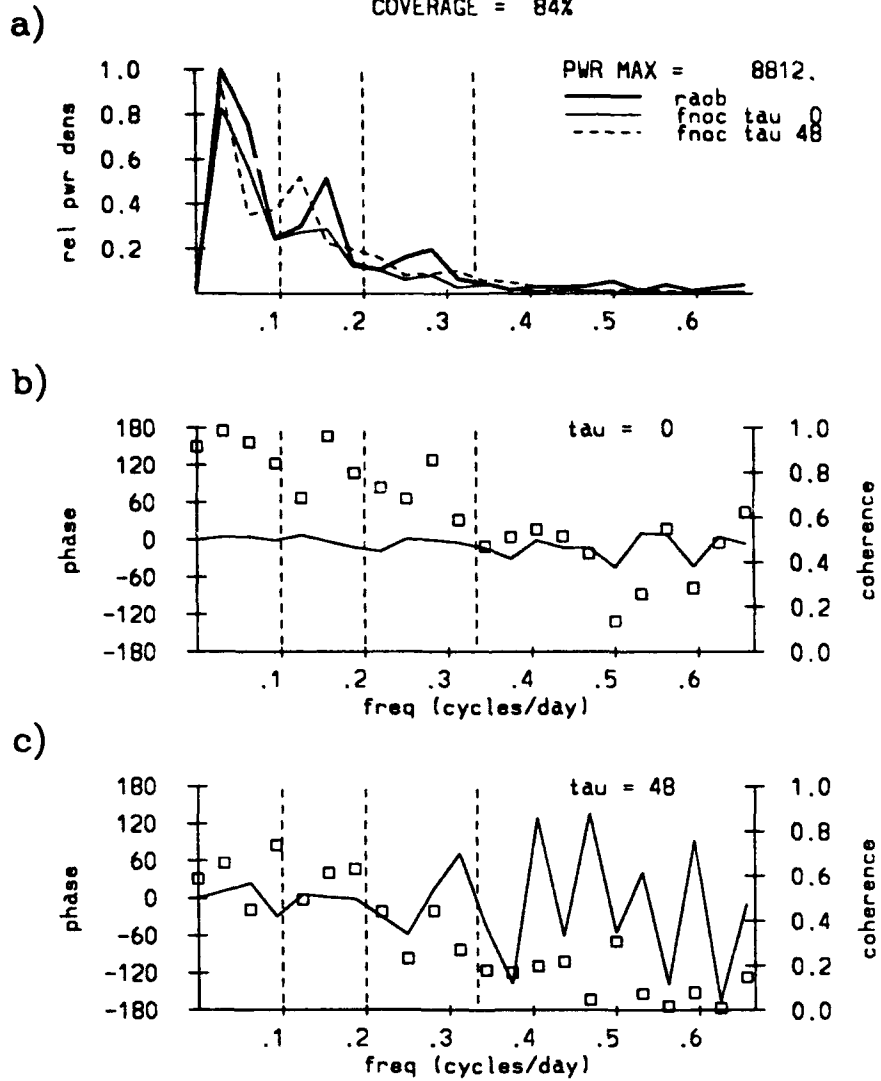


Fig. 8. Same as Fig. 7 except for Ponape.

TRUK ( 7.5N,151.9E)  
 PARAMETER = 850 MB ZONAL WIND  
 91111200 - 92031812  
 COVERAGE = 91%

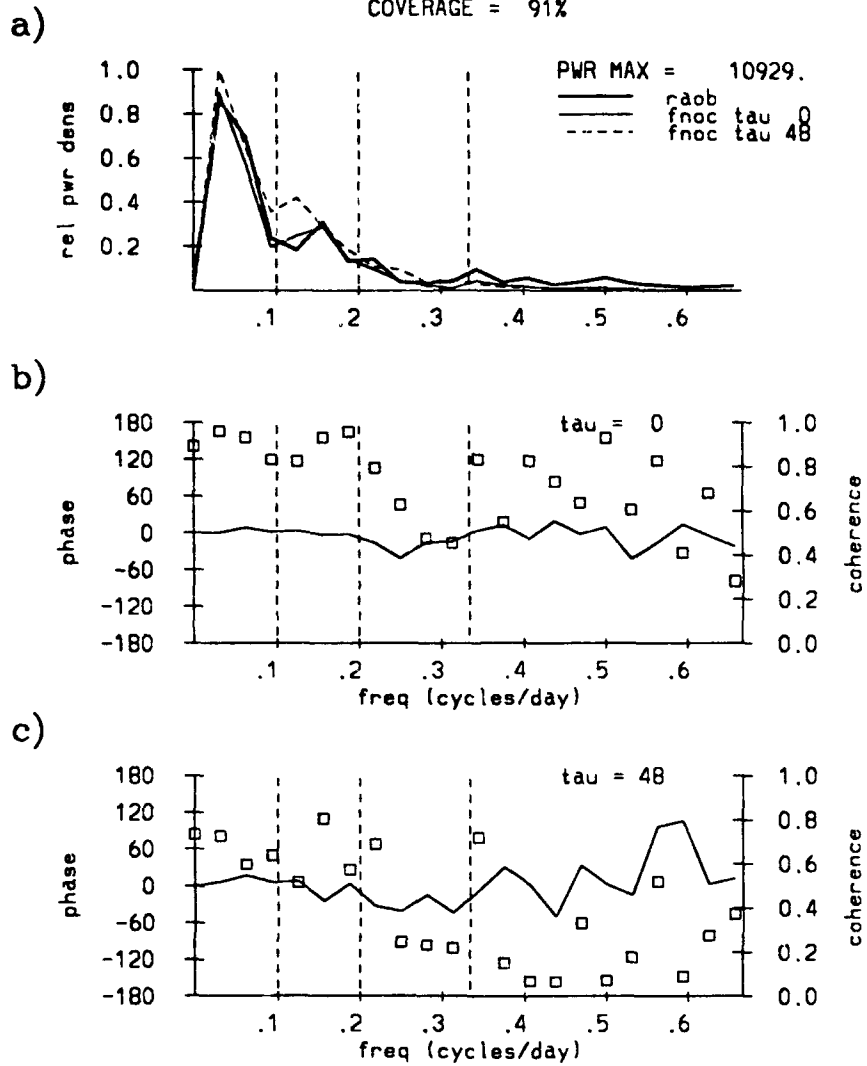


Fig. 9. Same as Fig. 7 except for Truk.

GUAM (13.6N,144.8E)  
 PARAMETER = 850 MB ZONAL WIND  
 9111200 - 92031812  
 COVERAGE = 90%

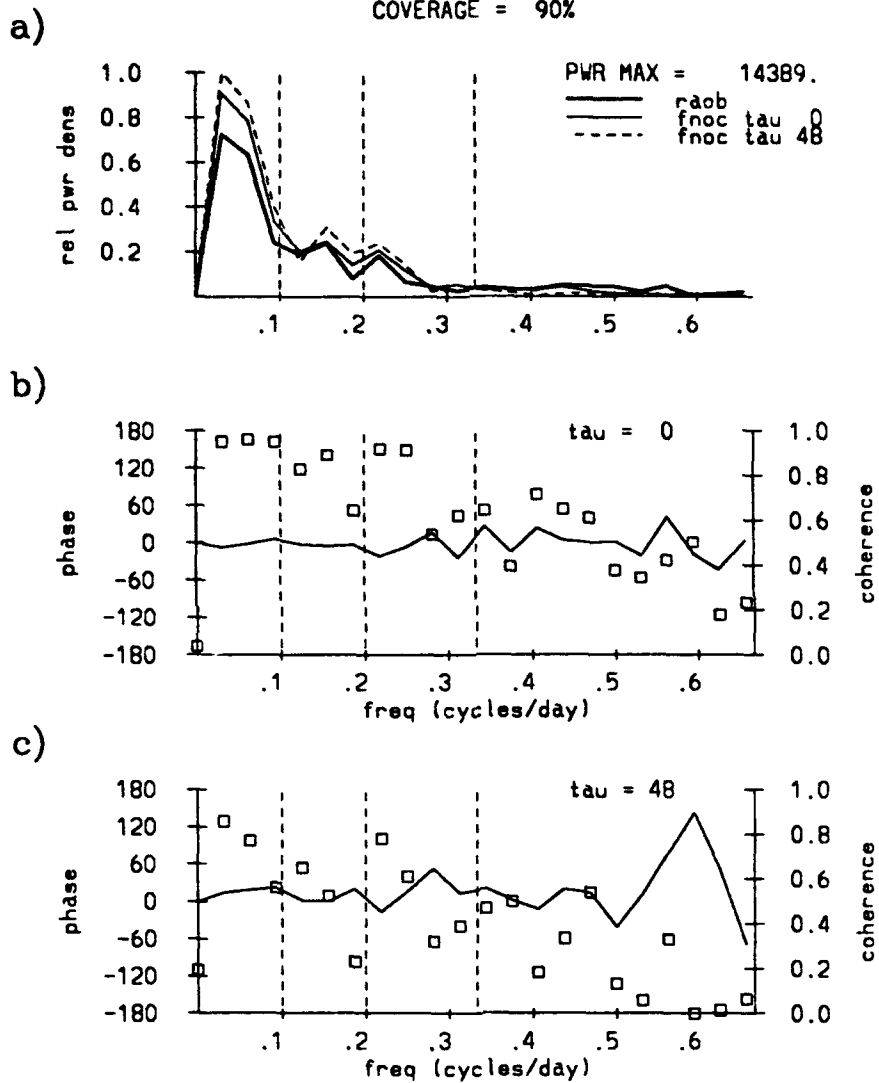


Fig. 10. Same as Fig. 7 except for Guam

YAP ( 9.5N,138.1E)  
 PARAMETER = 850 MB ZONAL WIND  
 91111200 - 92031812  
 COVERAGE = 90%

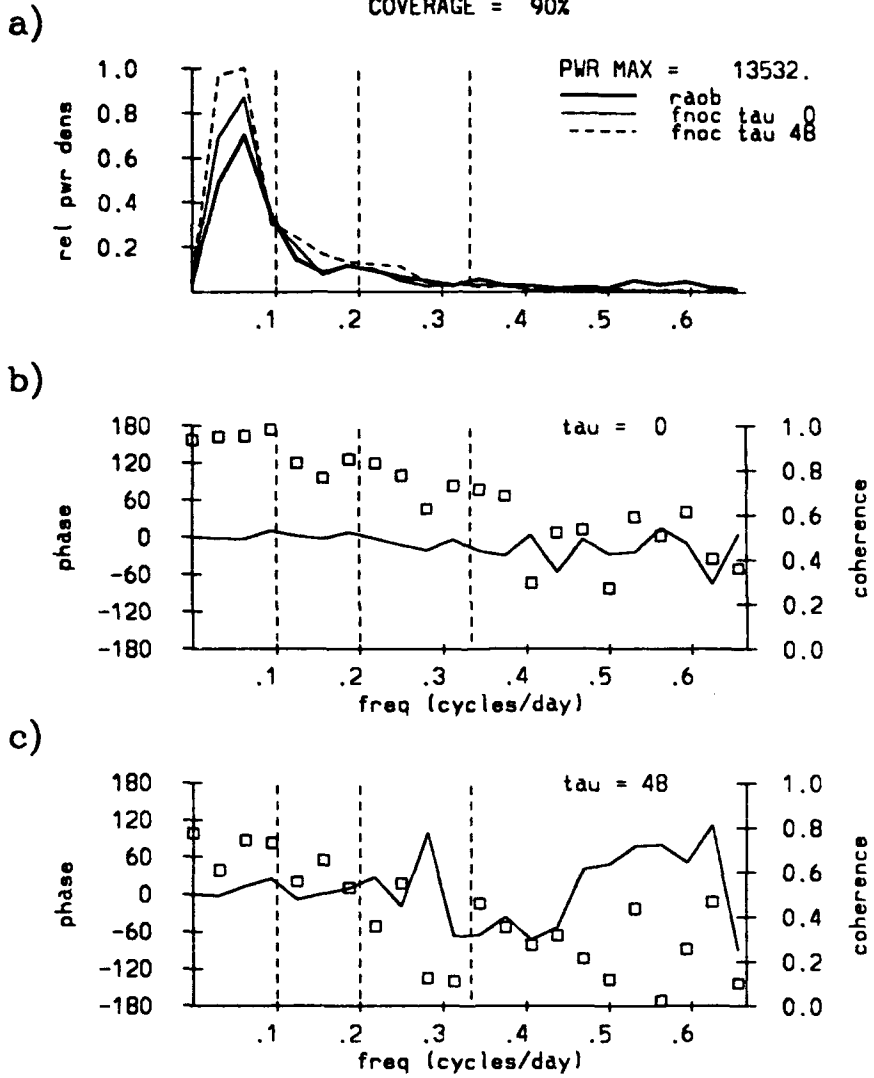


Fig. 11. Same as Fig. 7 except for Yap.

KOROR ( 7.3N,134.5E)  
 PARAMETER = 850 MB ZONAL WIND  
 91111200 - 92031812  
 COVERAGE = 82%

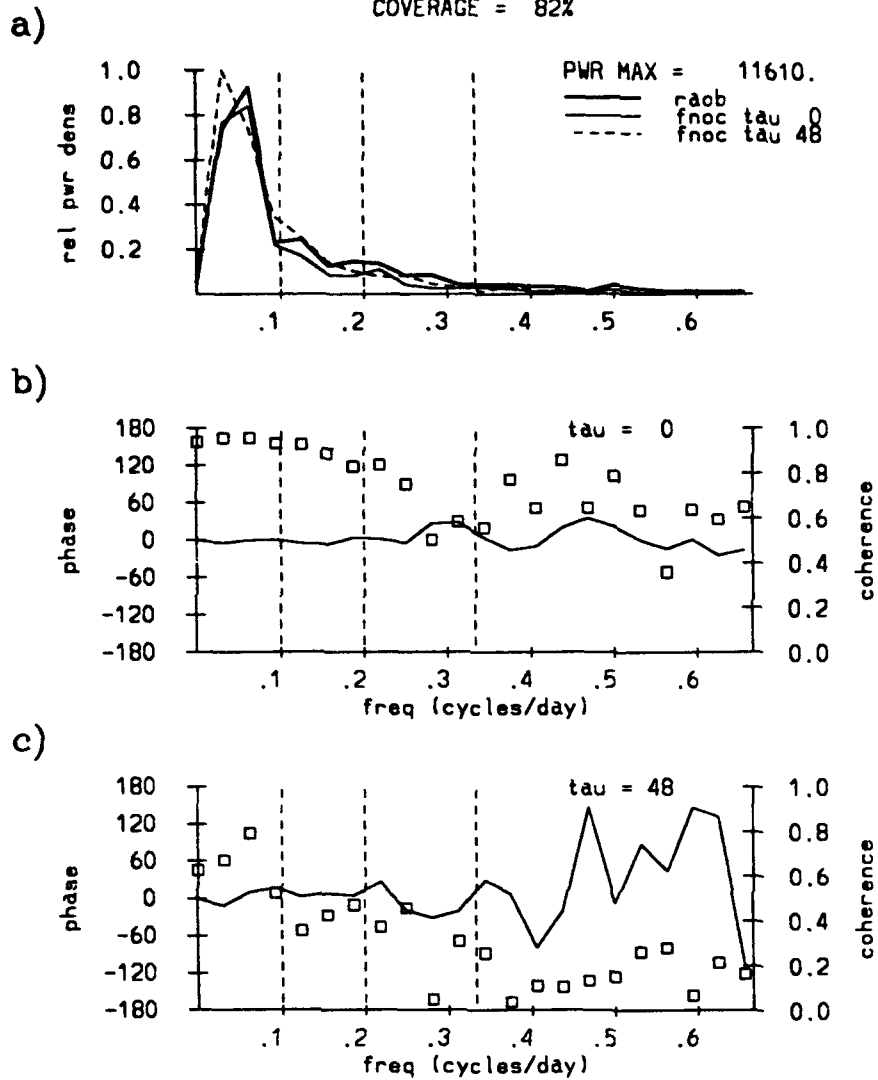


Fig. 12. Same as Fig. 7 except for Koror.



MAJURO ( 7.1N,171.4E)  
 PARAMETER = 200 MB MERIDIONAL WIND  
 91111200 - 92031812  
 COVERAGE = 87%

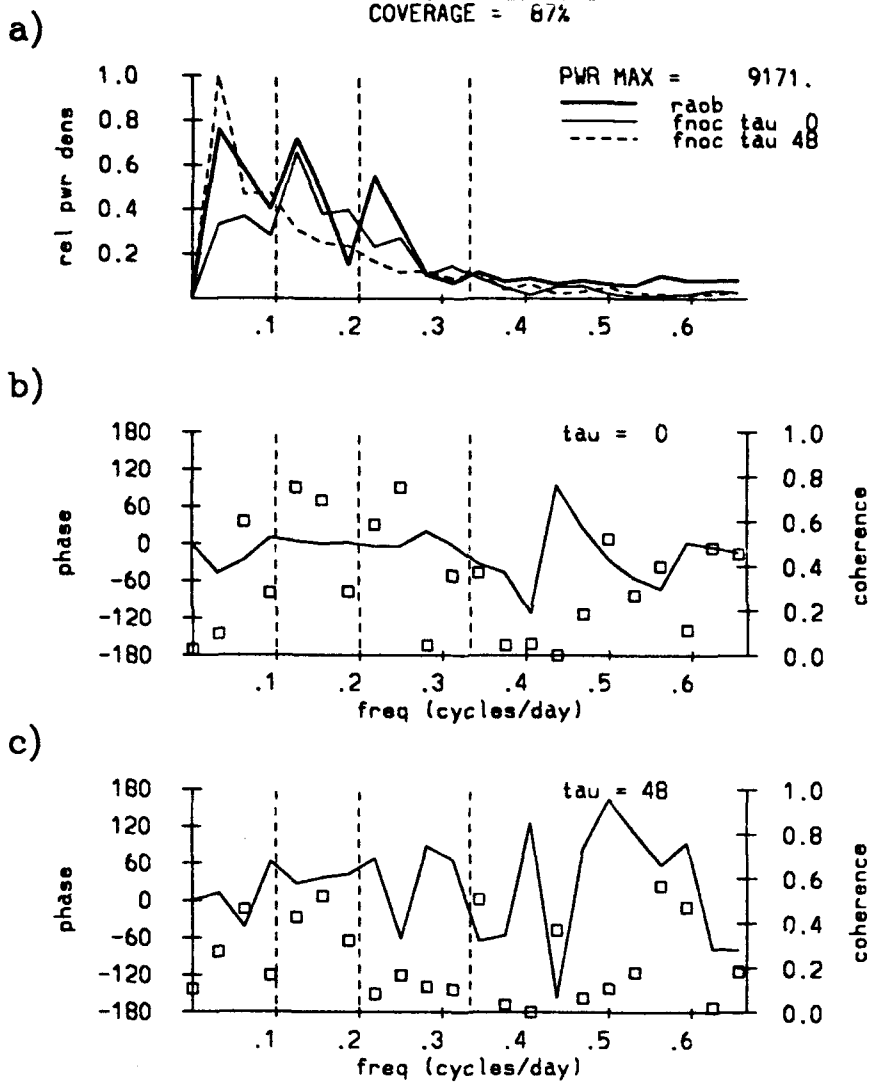


Fig. 13. Comparison of  $v_{200}$  spectra at Majuro: a) relative power spectra for RAOB (thick),  $\tau_{00}$  (thin) and  $\tau_{48}$  (dashed), b) phase difference (line) and coherence square (square) between RAOB and  $\tau_{00}$ , c) phase difference (line) and coherence square (square) between RAOB and  $\tau_{48}$ .

PONAPE ( 7.0N,158.2E)  
 PARAMETER = 200 MB MERIDIONAL WIND  
 91111200 - 92031812  
 COVERAGE = 86%

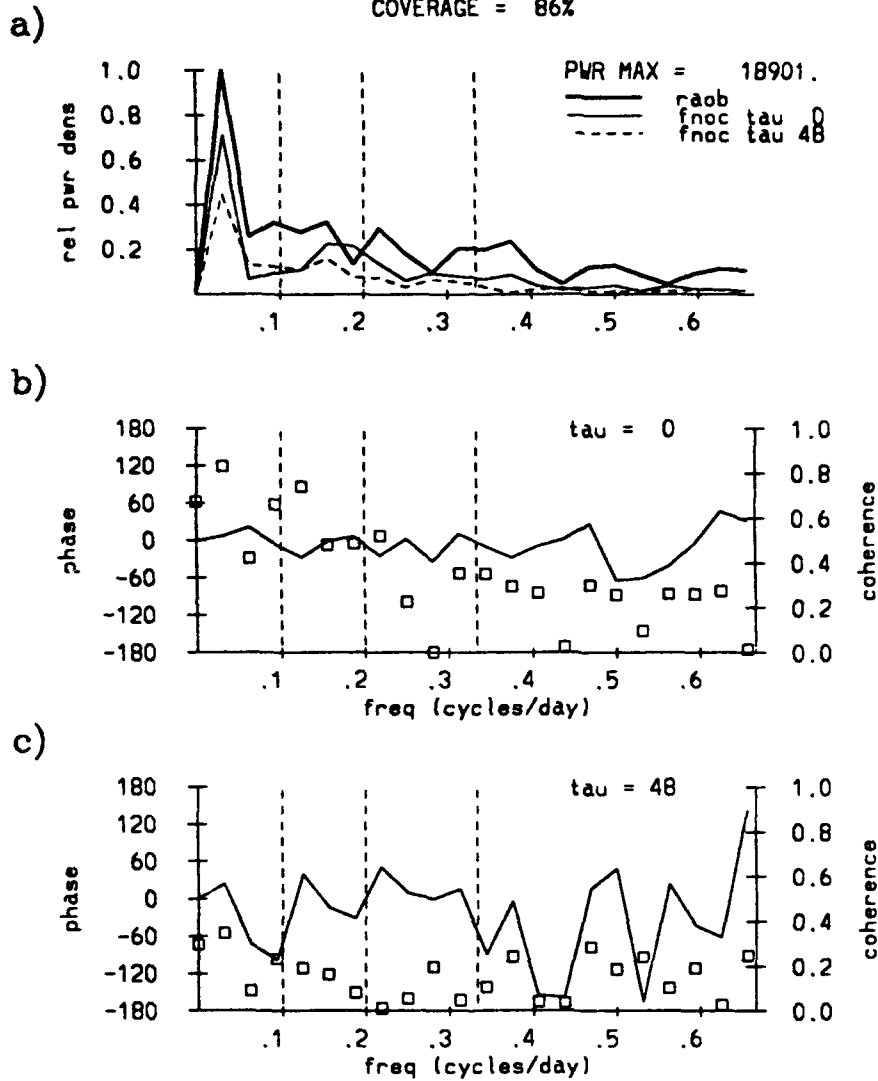


Fig. 14. Same as Fig. 13 except for Ponape.

TRUK ( 7.5N,151.9E)  
 PARAMETER = 200 MB MERIDIONAL WIND  
 91111200 - 92031812  
 COVERAGE = 86%

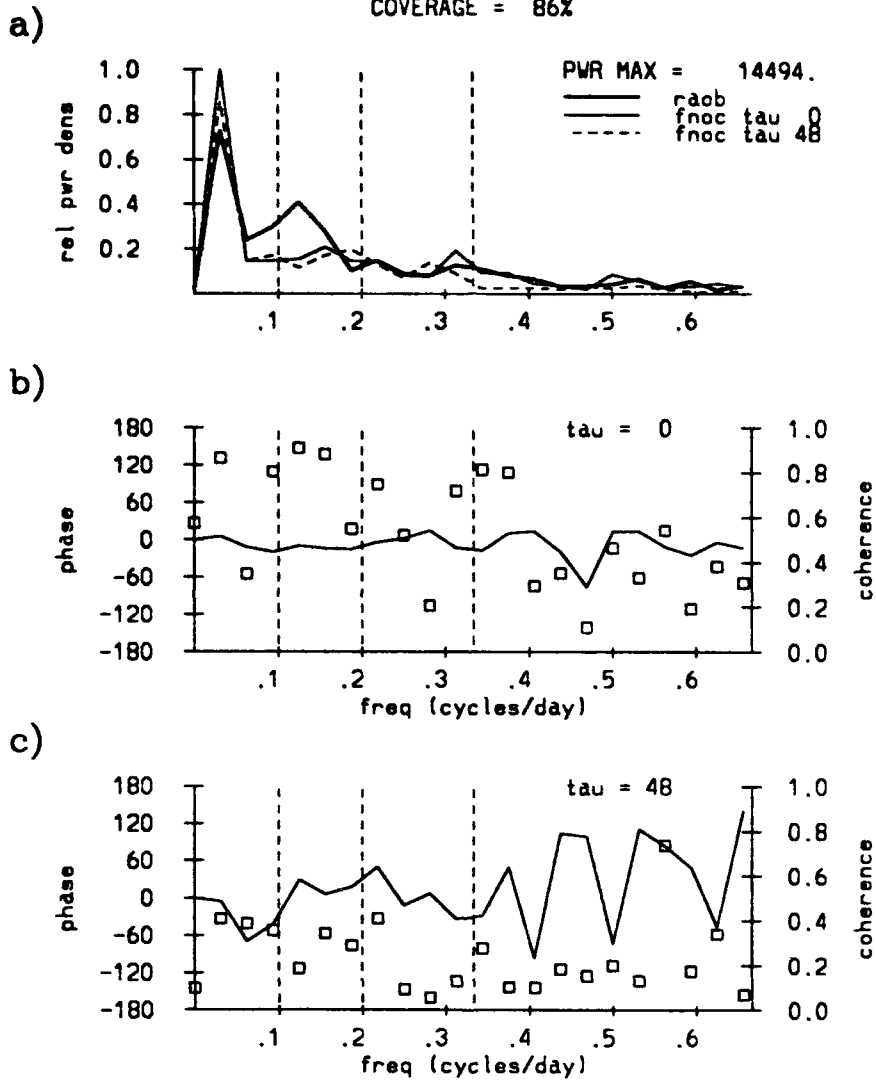


Fig. 15. Same as Fig. 13 except for Truk.

**GUAM (13.6N,144.8E)**  
 PARAMETER = 200 MB MERIDIONAL WIND  
 9111200 - 92031812  
 COVERAGE = 89%

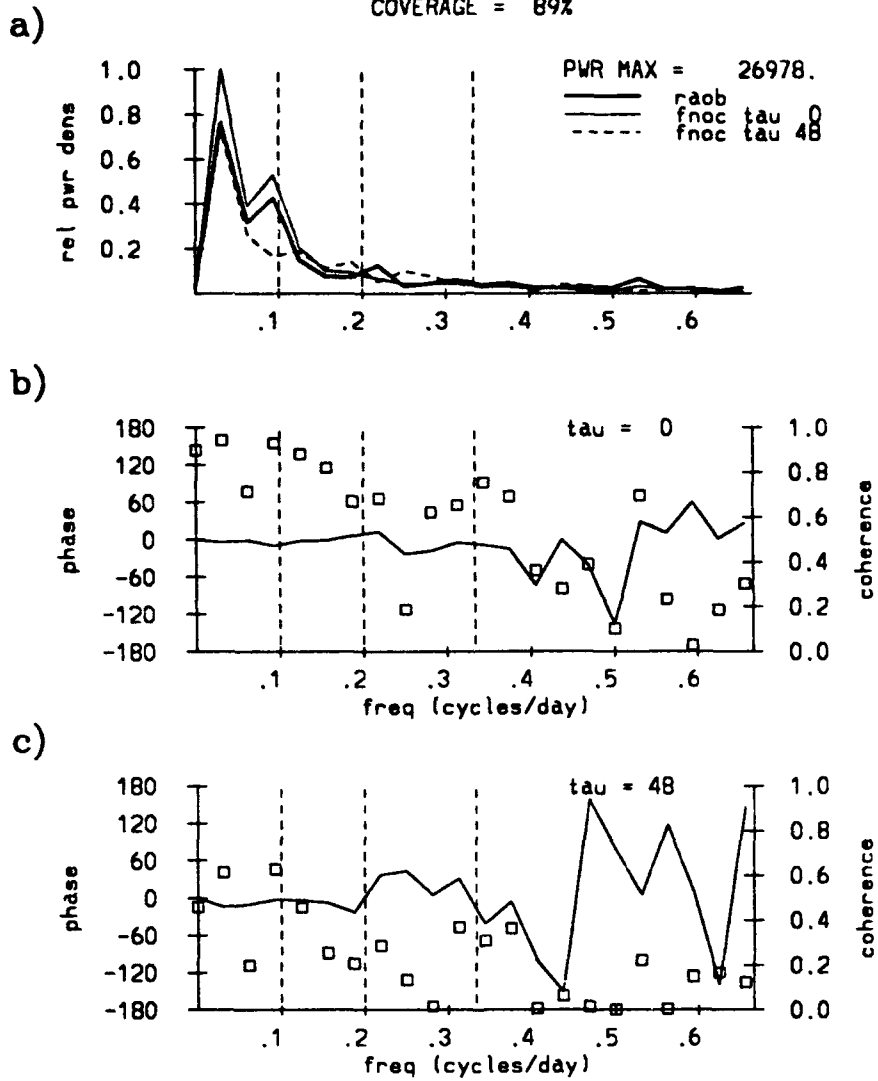


Fig. 16. Same as Fig. 13 except for Guam

YAP (9.5N,138.1E)  
 PARAMETER = 200 MB MERIDIONAL WIND  
 91111200 - 92031812  
 COVERAGE = 88%

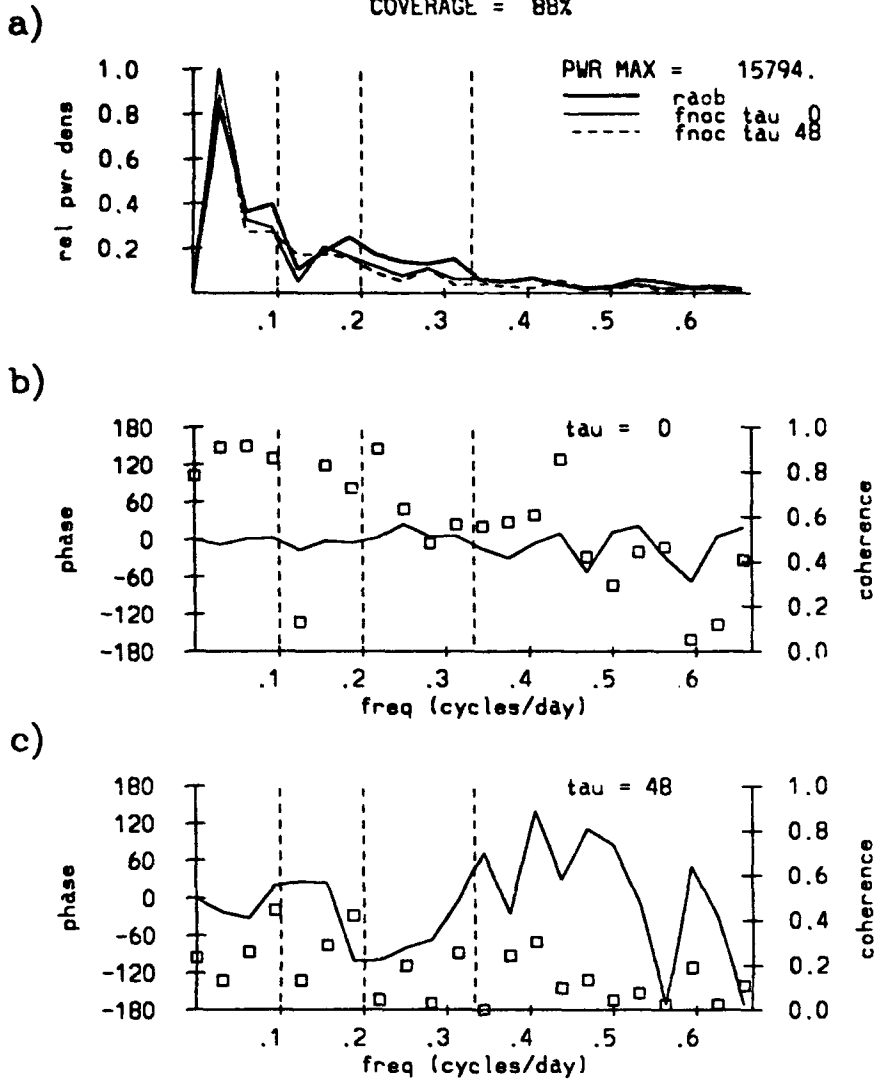


Fig. 17. Same as Fig. 13 except for Yap.

KOROR ( 7.3N,134.5E)  
 PARAMETER = 200 MB MERIDIONAL WIND  
 91111200 - 92031812  
 COVERAGE = 78%

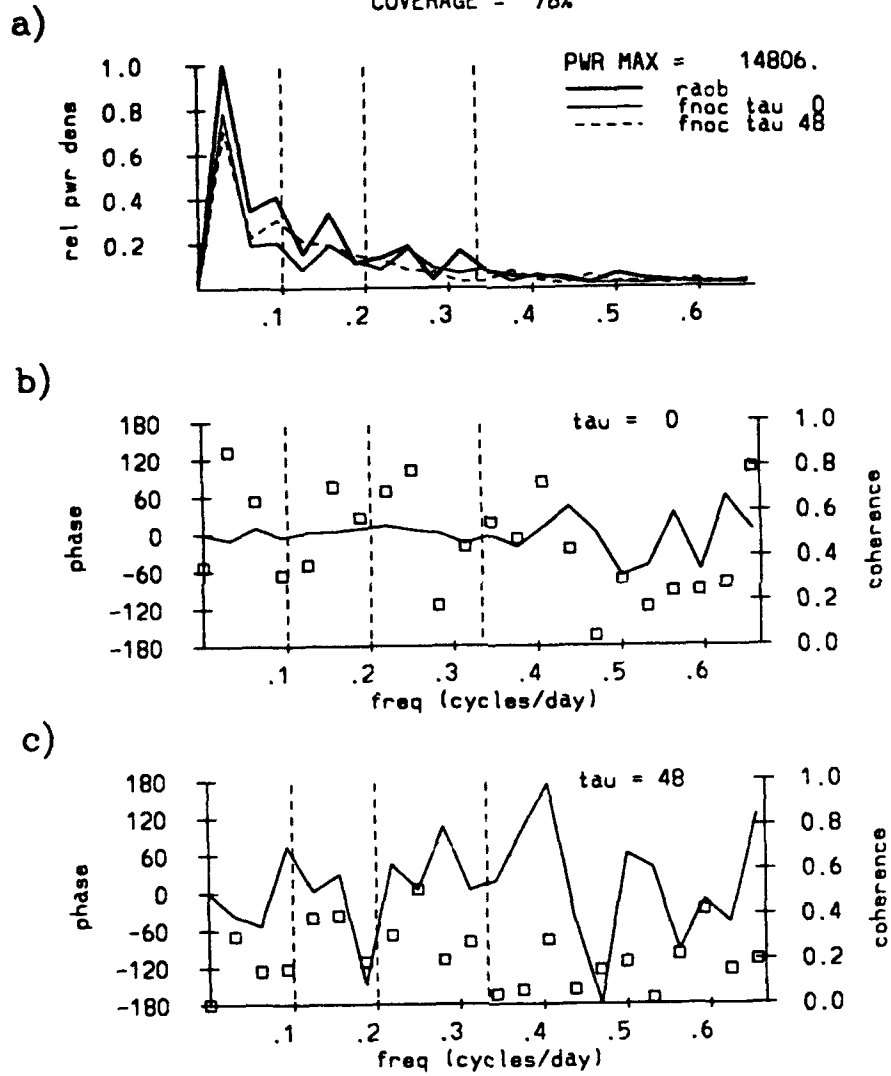


Fig. 18. Same as Fig. 13 except for Koror.

MAJURO ( 7.1N,171.4E)  
 PARAMETER = 200 MB ZONAL WIND  
 91111200 - 92031812  
 COVERAGE = 87%

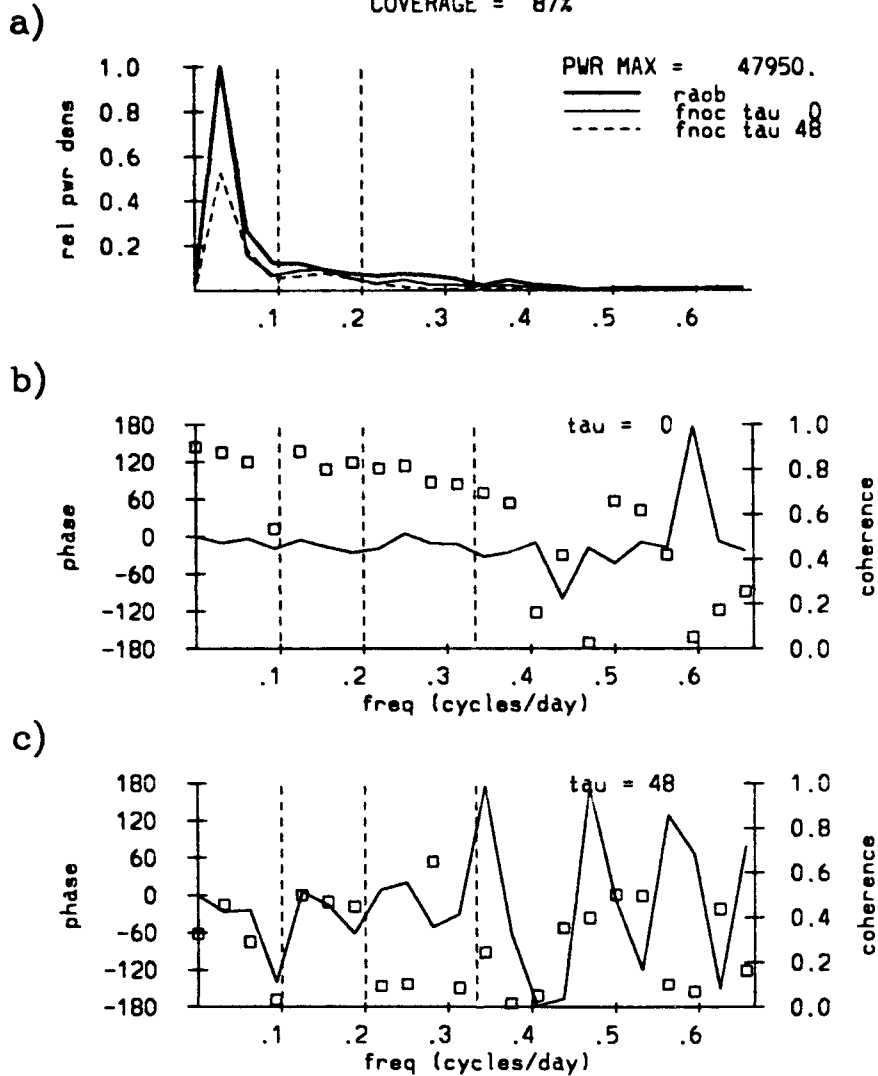


Fig. 19. Comparison of  $u_{200}$  spectra at Majuro: a) relative power spectra for RAOB (thick),  $\tau_{00}$  (thin) and  $\tau_{48}$  (dashed), b) phase difference (line) and coherence square (square) between RAOB and  $\tau_{00}$ , c) phase difference (line) and coherence square (square) between RAOB and  $\tau_{48}$ .

PONAPE ( 7.0N,158.2E)  
 PARAMETER = 200 MB ZONAL WIND  
 9111200 - 92031812  
 COVERAGE = 86%

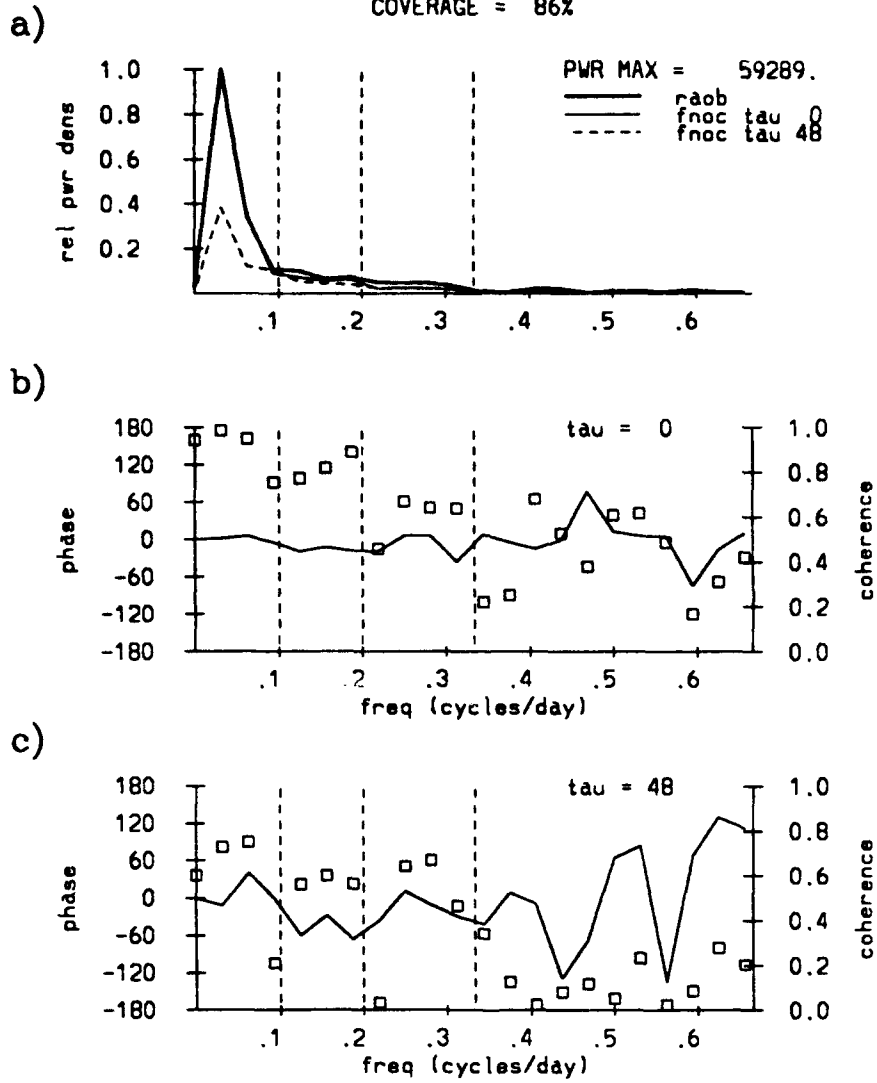


Fig. 20. Same as Fig. 19 except for Ponape.



TRUK ( 7.5N,151.9E)  
 PARAMETER = 200 MB ZONAL WIND  
 91111200 - 92031812  
 COVERAGE = 86%

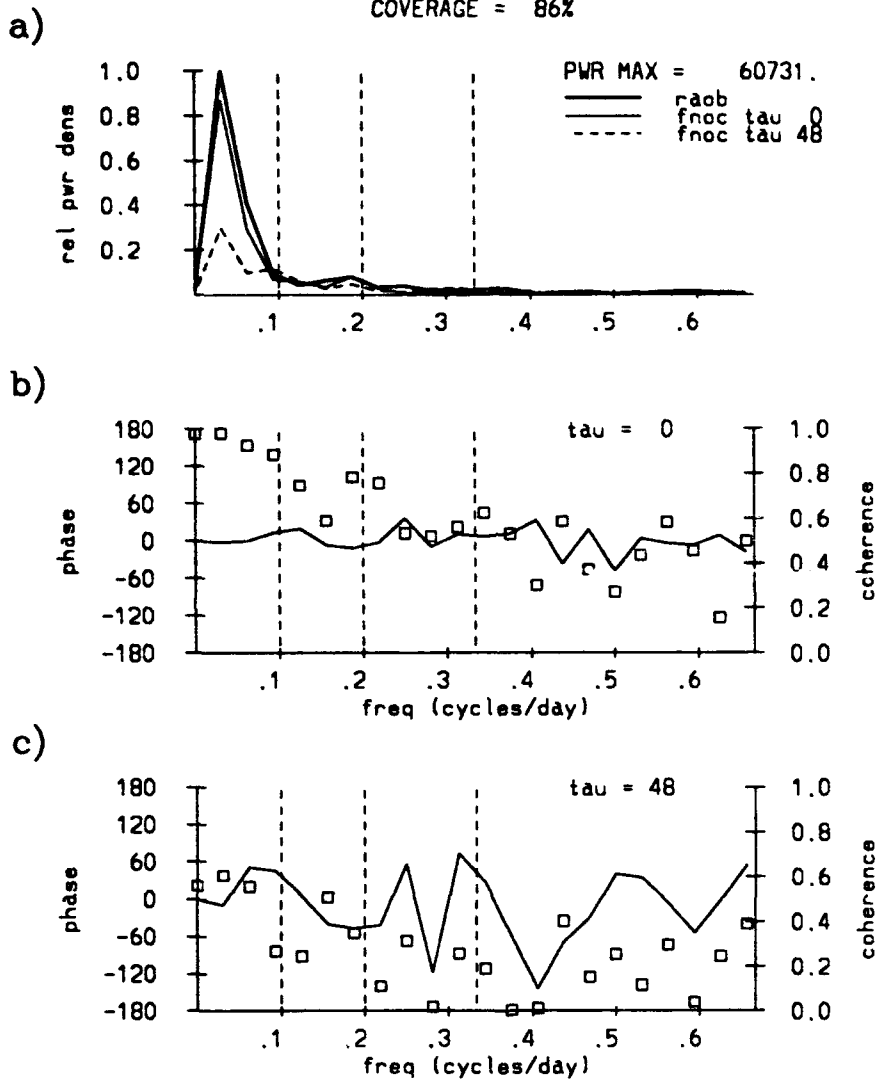


Fig. 21. Same as Fig. 19 except for Truk.

GUAM (13.6N,144.8E)  
 PARAMETER = 200 MB ZONAL WIND  
 91111200 - 92031812  
 COVERAGE = 89%

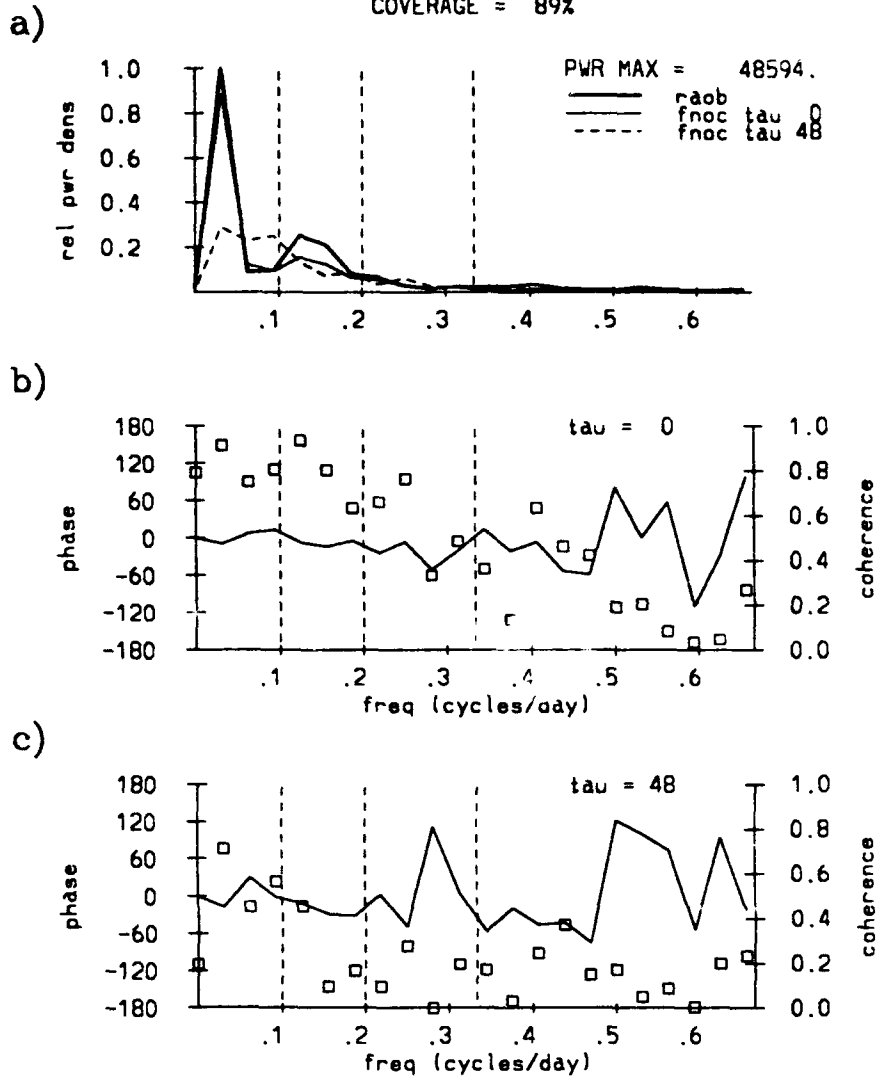


Fig. 22. Same as Fig. 19 except for Guam

YAP ( 9.5N,138.1E)  
 PARAMETER = 200 MB ZONAL WIND  
 91111200 - 92031812  
 COVERAGE = 88%

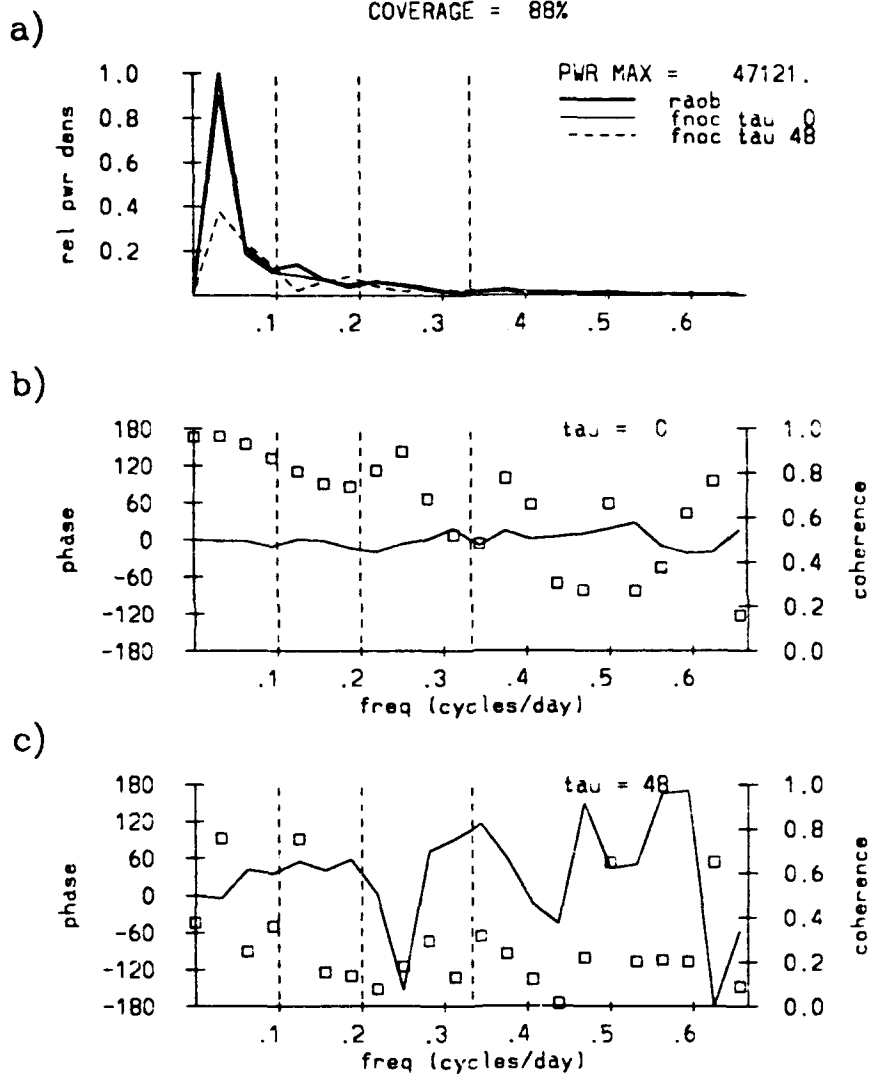


Fig. 23. Same as Fig. 19 except for Yap.

KOROR ( 7.3N,134.5E)  
 PARAMETER = 200 MB ZONAL WIND  
 91111200 - 92031812  
 COVERAGE = 78%

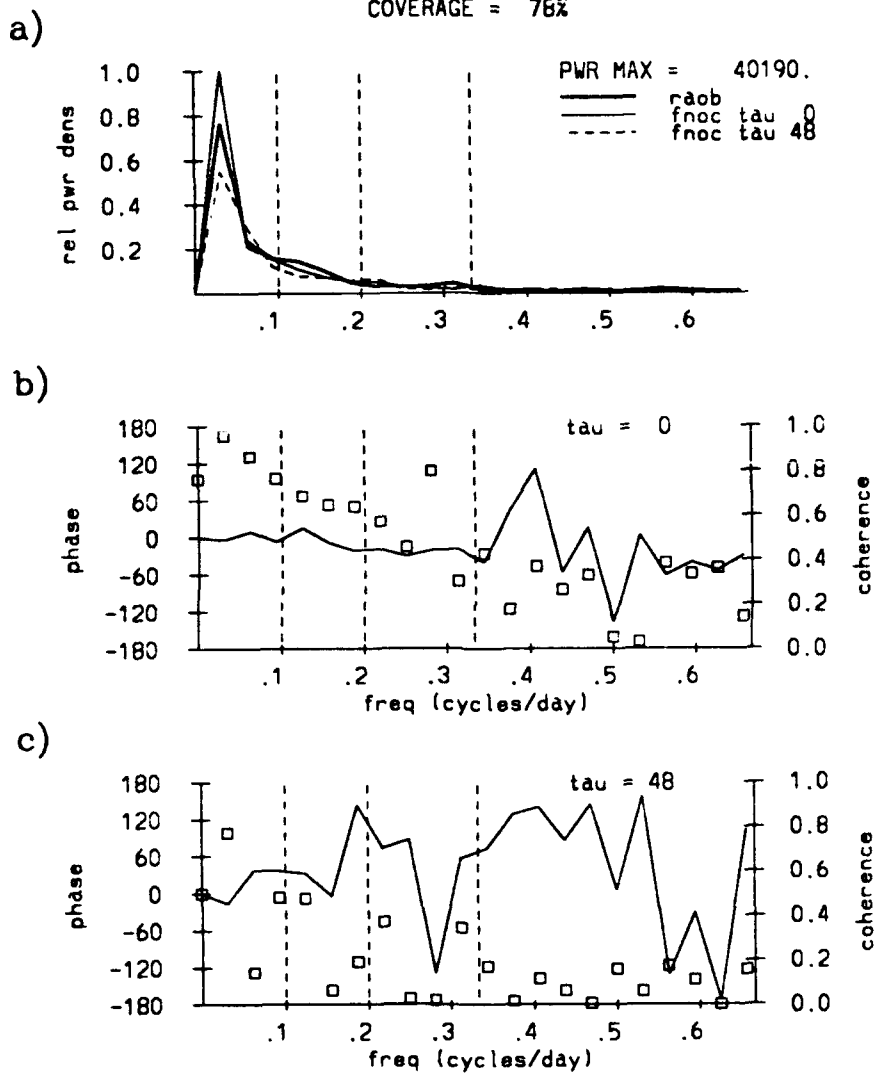


Fig. 24. Same as Fig. 19 except for Koror.

V 850 MB TAU 00  
 LATITUDE = 7.5

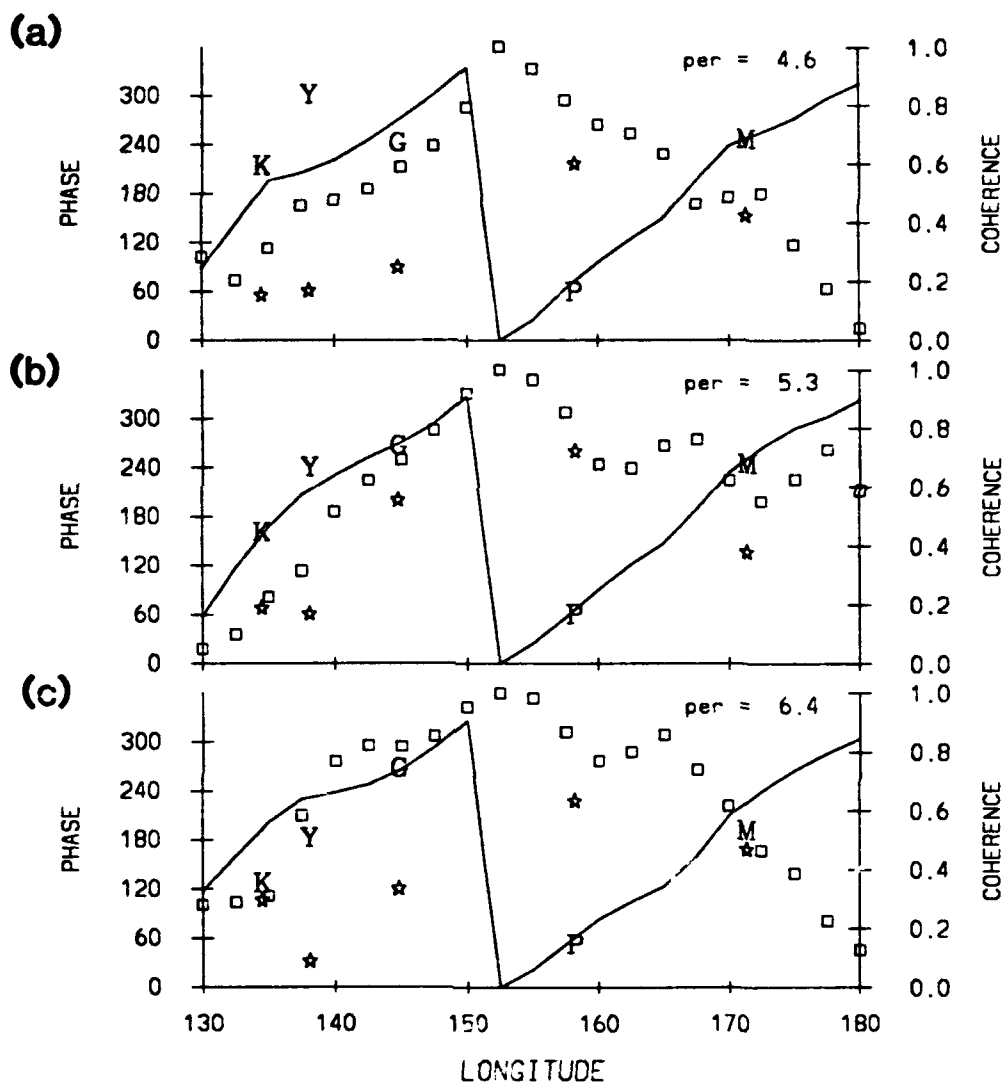


Fig. 25. Phase difference (line) and coherence square (square) of  $\tau_{00} v_{850}$  between Truk as the base series and Majuro (M), Ponape (P), Guam (G), Yap (Y) and Koror (K) for: a) 4.6-day, b) 5.3-day, and c) 6.4-day periods.

V 850 MB TAU 48  
 LATITUDE = 7.5

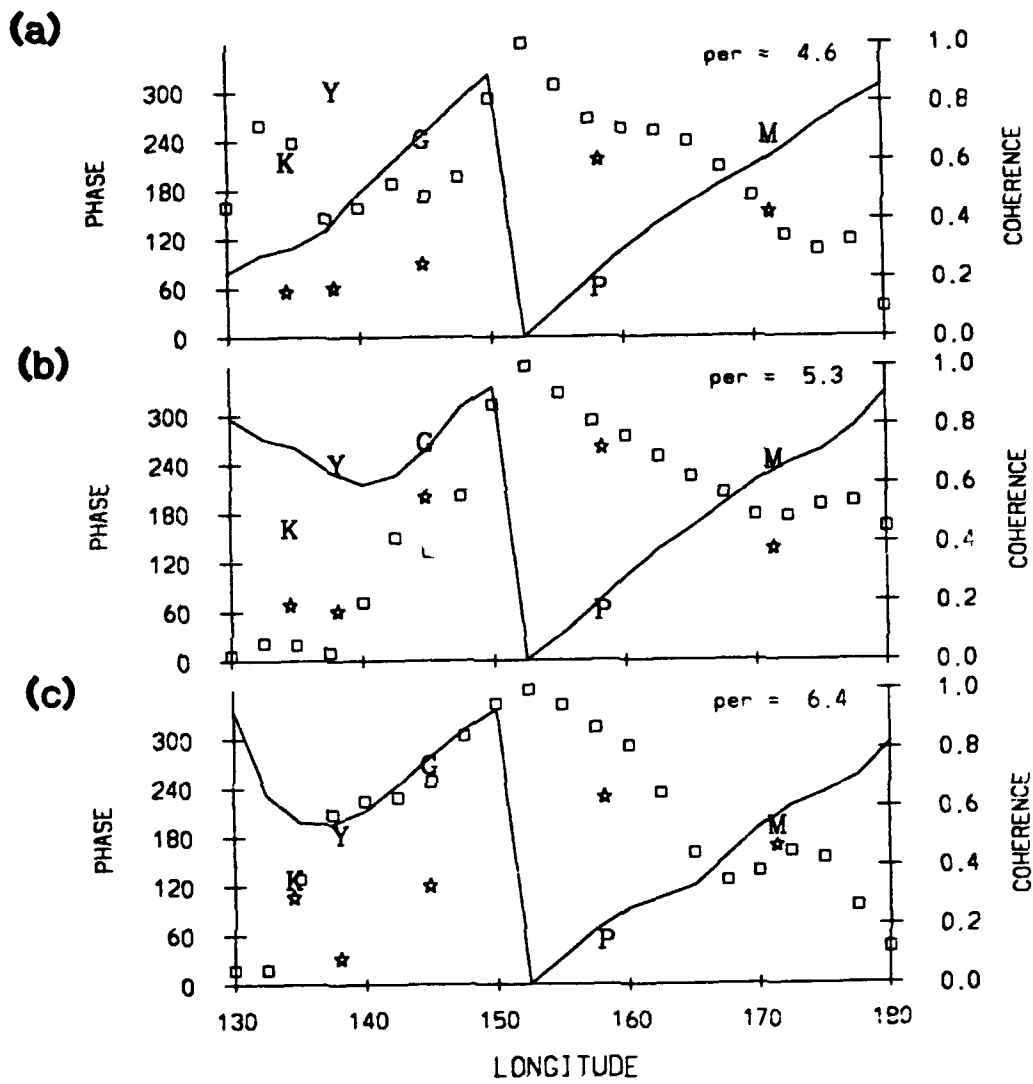


Fig. 26. Same as Fig. 25 except for  $\tau_{48}$  v850.

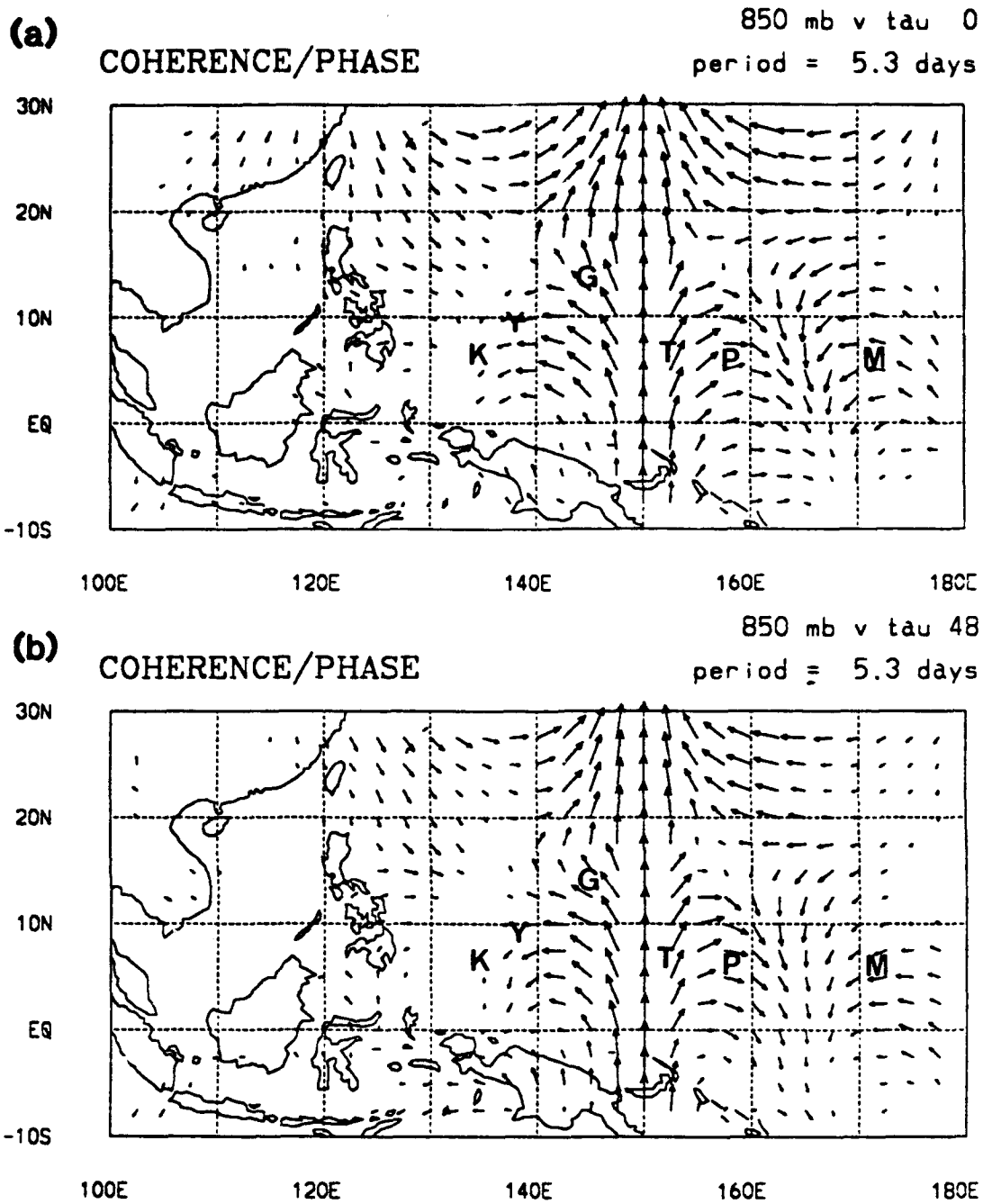
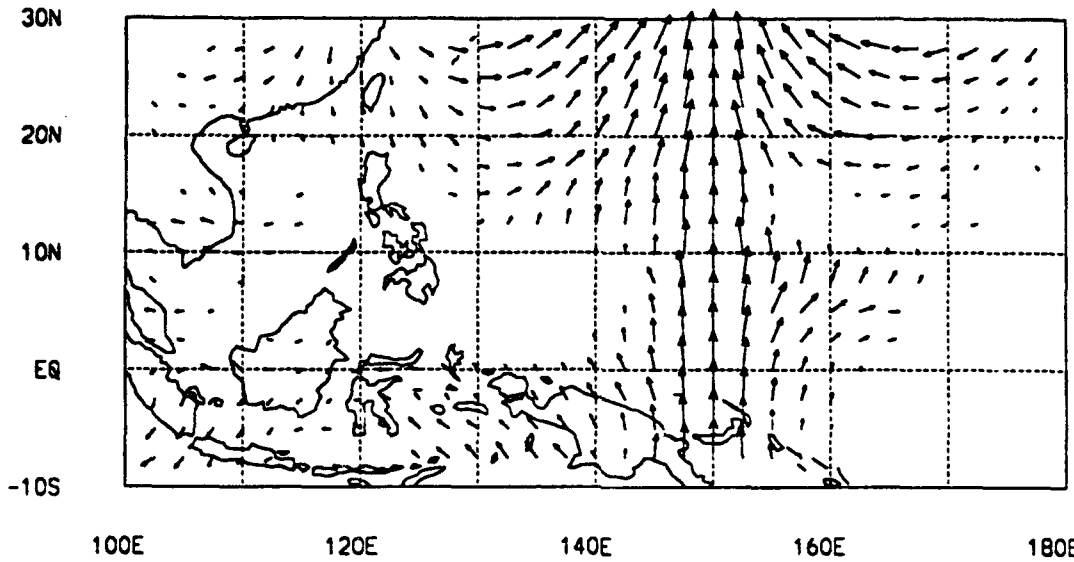


Fig. 27. Inter-longitude cross spectra for the synoptic band (averaged period 5.3 days) for  $v_{850}$  with the  $150^\circ\text{E}$  data as the base series longitude. The phase difference and coherence square between each grid point and the base series at the same latitude are plotted as a vector, with the direction indicating phase difference (northward pointing =  $0^\circ$ , increasing clockwise), and the magnitude indicating coherence square: a)  $\tau_{00}$ , and b)  $\tau_{48}$ . The location of the Caroline Island radiosonde stations are indicated with the first letter of the station name.

(a)

COHERENCE/PHASE

850 mb u tau 0  
period = 5.3 days



(b)

COHERENCE/PHASE

850 mb u tau 48  
period = 5.3 days

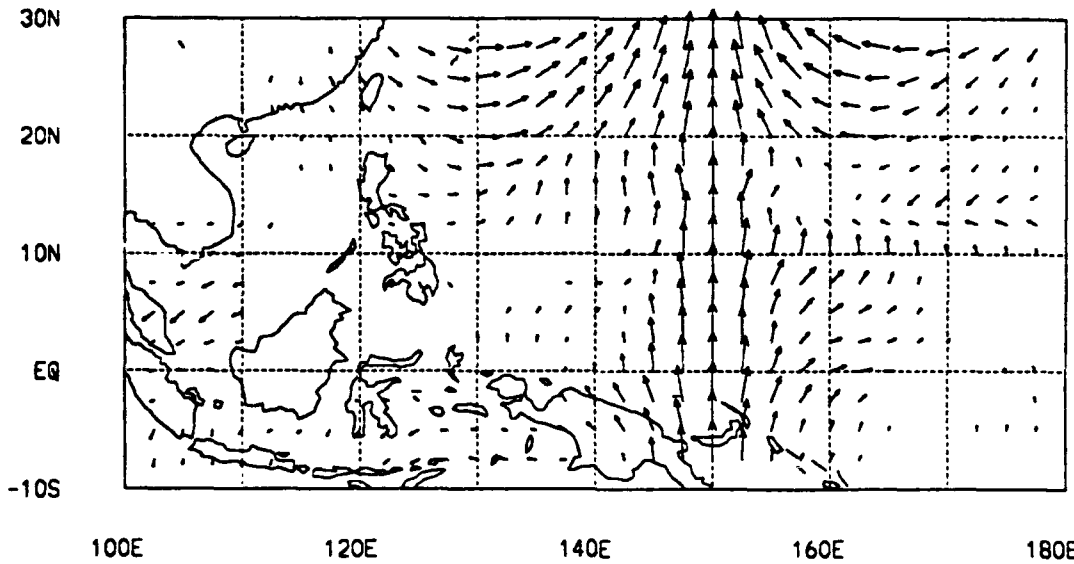


Fig. 28. Inter-longitude cross spectra, same as Fig. 27 except for  $u_{850}$ .



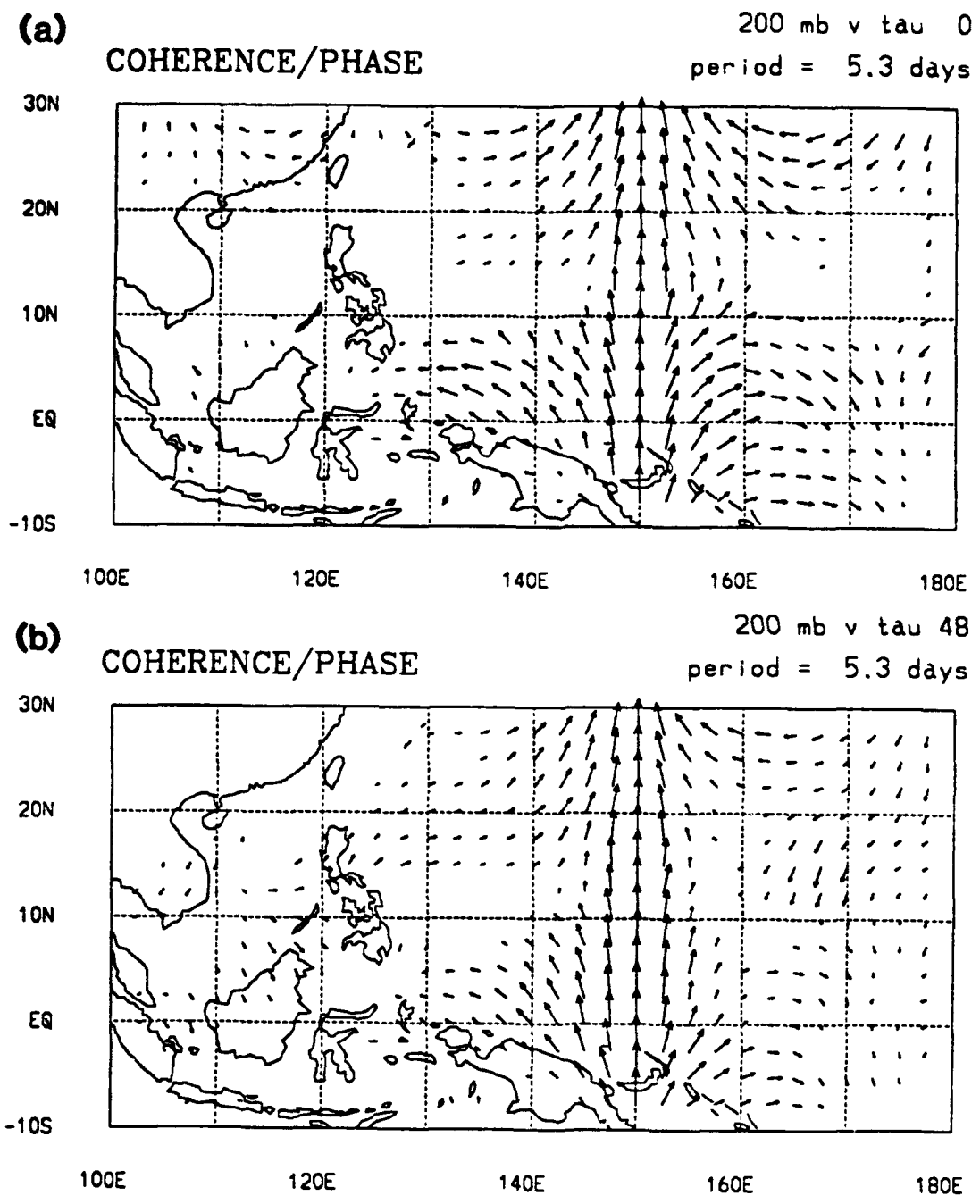
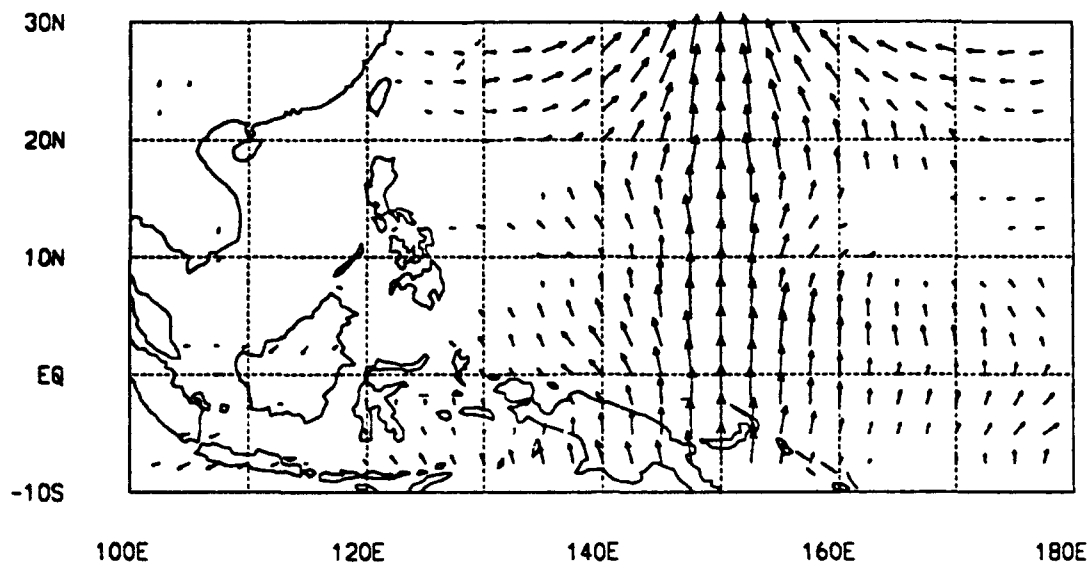


Fig. 29. Inter-longitude cross spectra, same as Fig. 27 except for  $v_{200}$ .

(a) COHERENCE/PHASE 200 mb u tau 0  
period = 5.3 days



(b) COHERENCE/PHASE 200 mb u tau 48  
period = 5.3 days

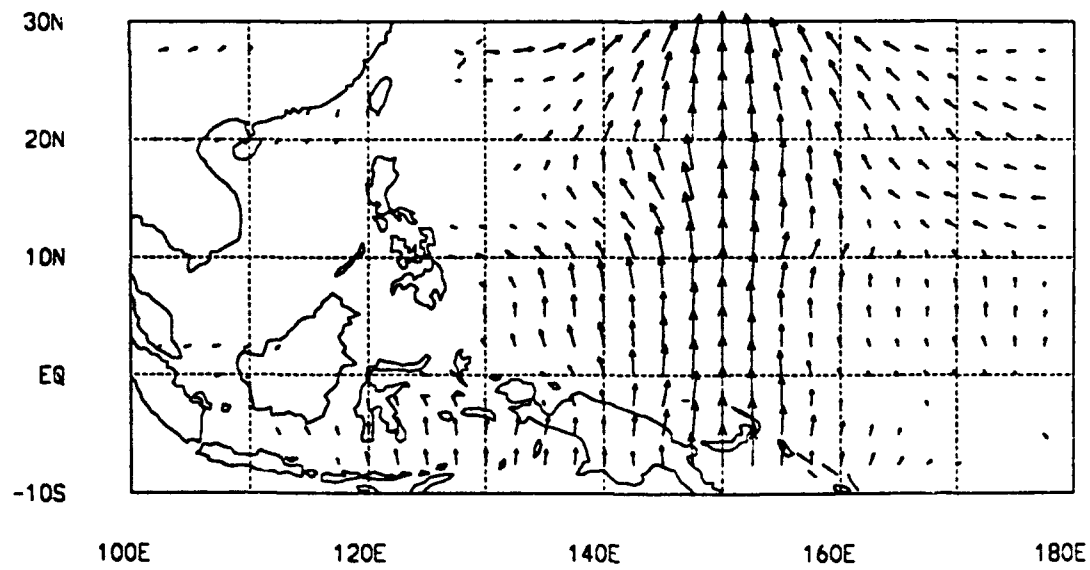
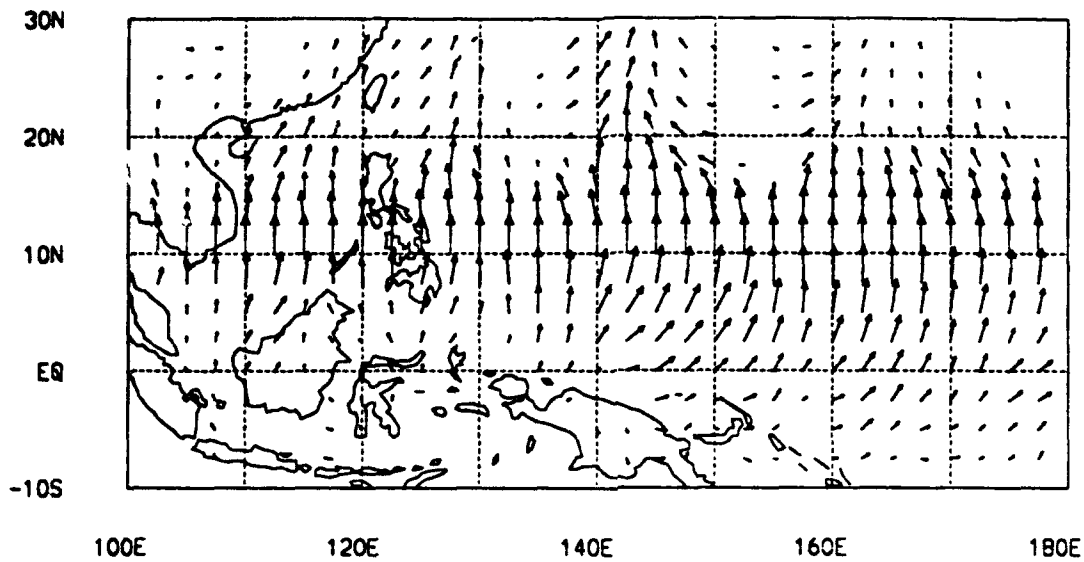


Fig. 30. Inter-longitude cross spectra, same as Fig. 27 except for  $u_{200}$ .

(a)

COHERENCE/PHASE

850 mb v tau 0  
period = 5.3 days



(b)

COHERENCE/PHASE

850 mb v tau 48  
period = 5.3 days

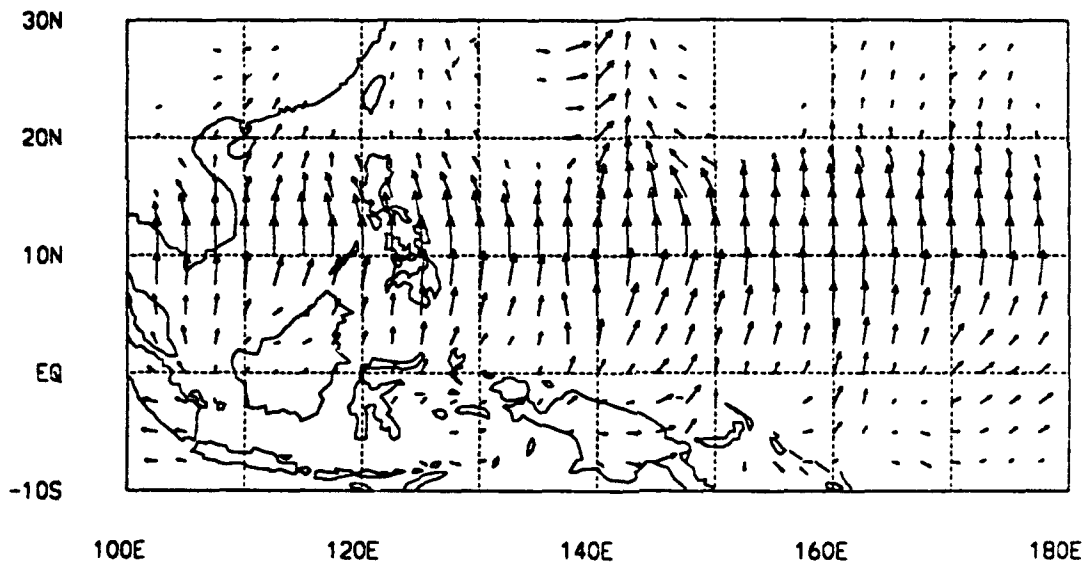


Fig. 31. Inter-latitude cross spectra for the synoptic band (averaged period 5.3 days) for  $v_{850}$  with the  $10^{\circ}\text{N}$  data as the base series latitude. The phase difference and coherence square between each grid point and the base series at the same longitude are plotted as a vector, with the direction indicating phase difference (northward pointing =  $0^{\circ}$ , increasing clockwise), and the magnitude indicating coherence square: a)  $\tau_{00}$ , and b)  $\tau_{48}$ .

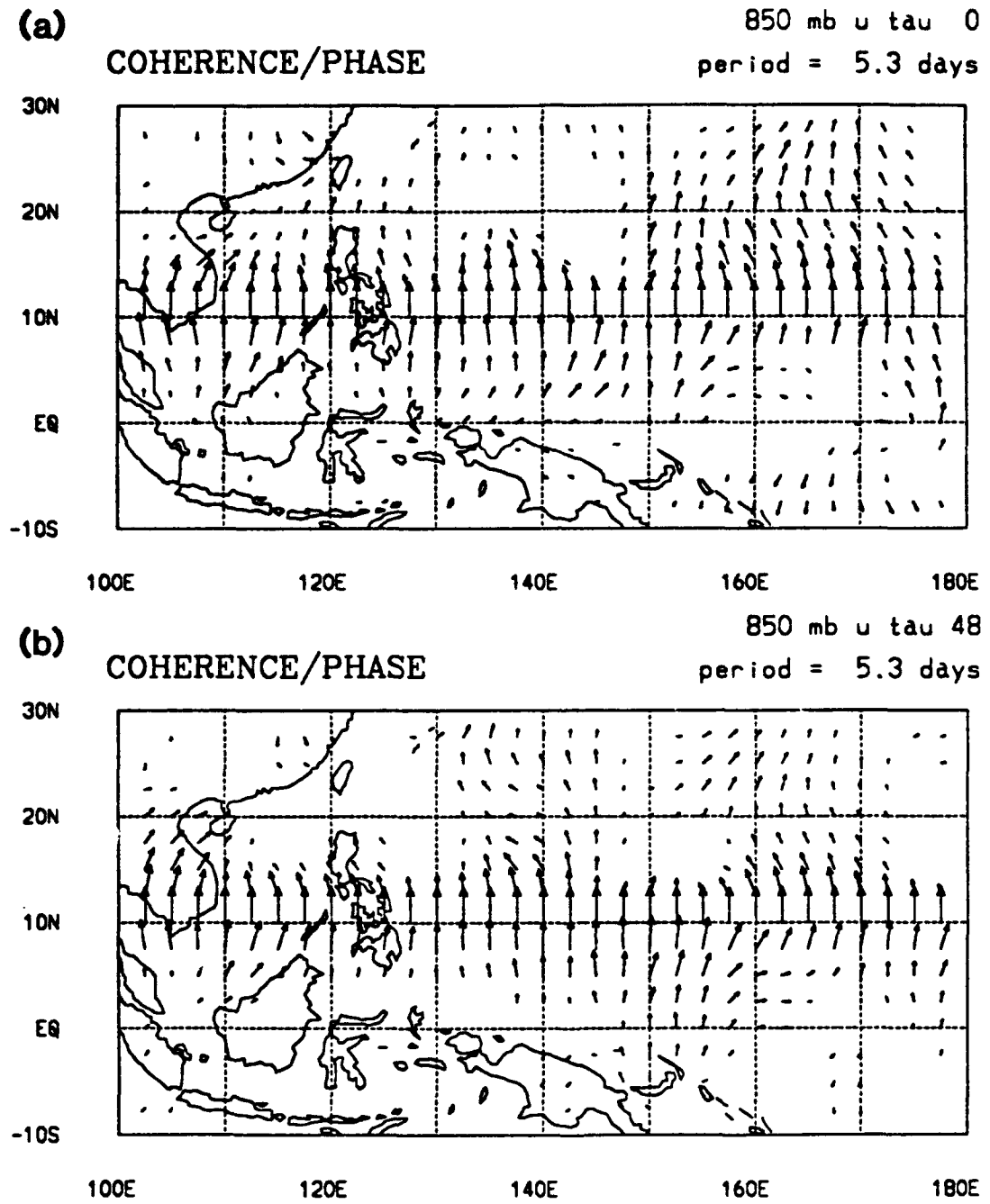
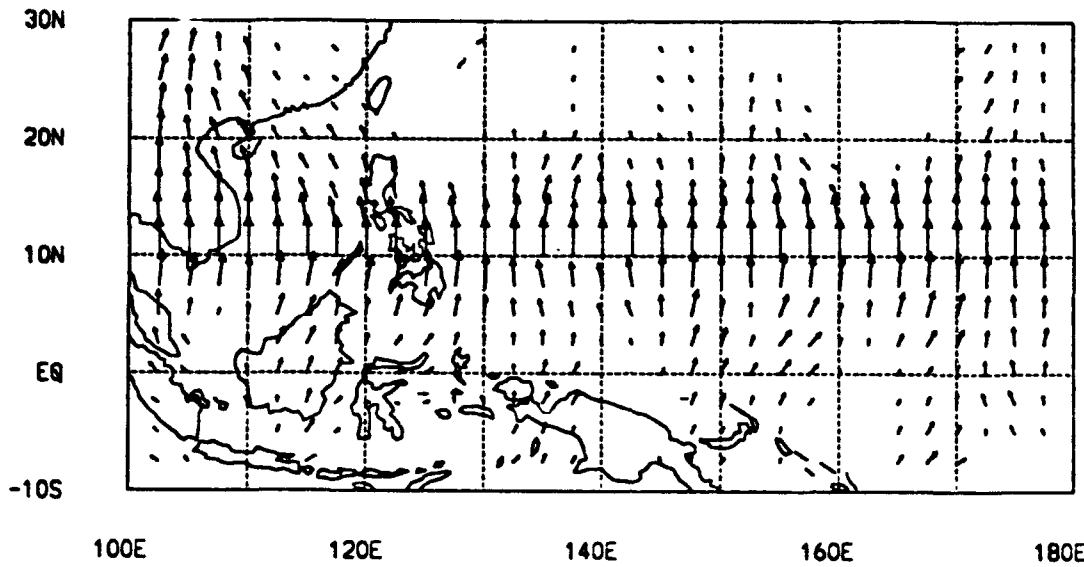


Fig. 32. Inter-latitude cross spectra, same as Fig. 31 except for  $u_{850}$ .

(a) 200 mb v tau 0  
COHERENCE/PHASE period = 5.3 days



(b) 200 mb v tau 48  
COHERENCE/PHASE period = 5.3 days

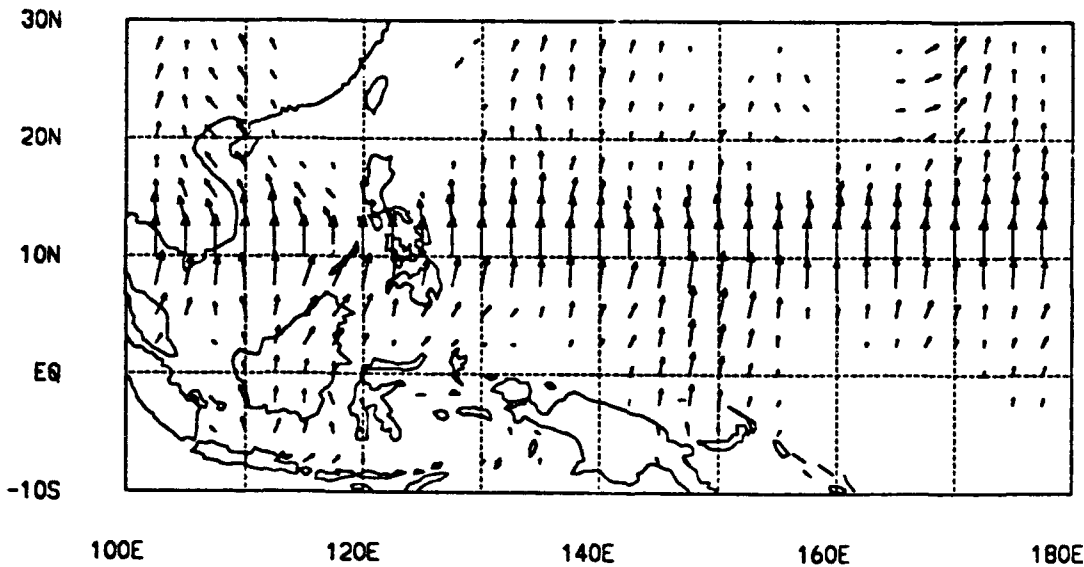
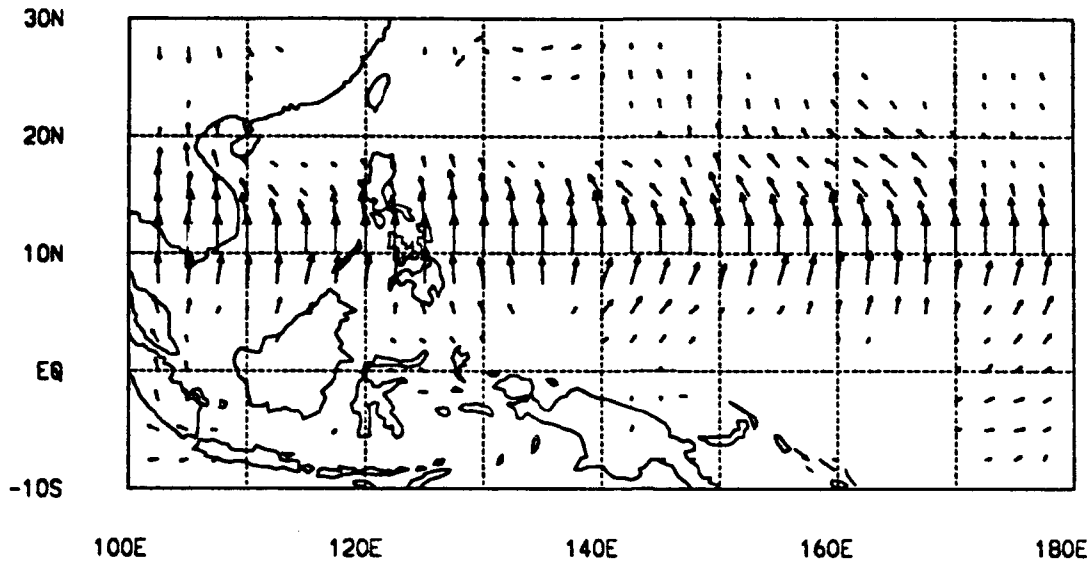


Fig. 33. Inter-latitude cross spectra, same as Fig. 31 except for  $v_{200}$ .

(a) 200 mb u tau 0  
COHERENCE/PHASE period = 5.3 days



(b) 200 mb u tau 48  
COHERENCE/PHASE period = 5.3 days

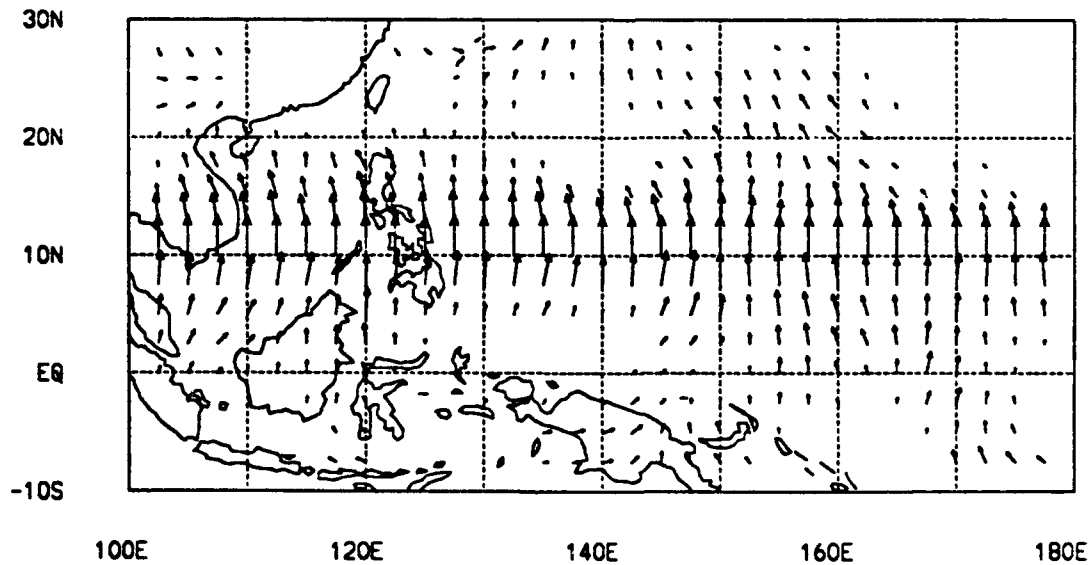


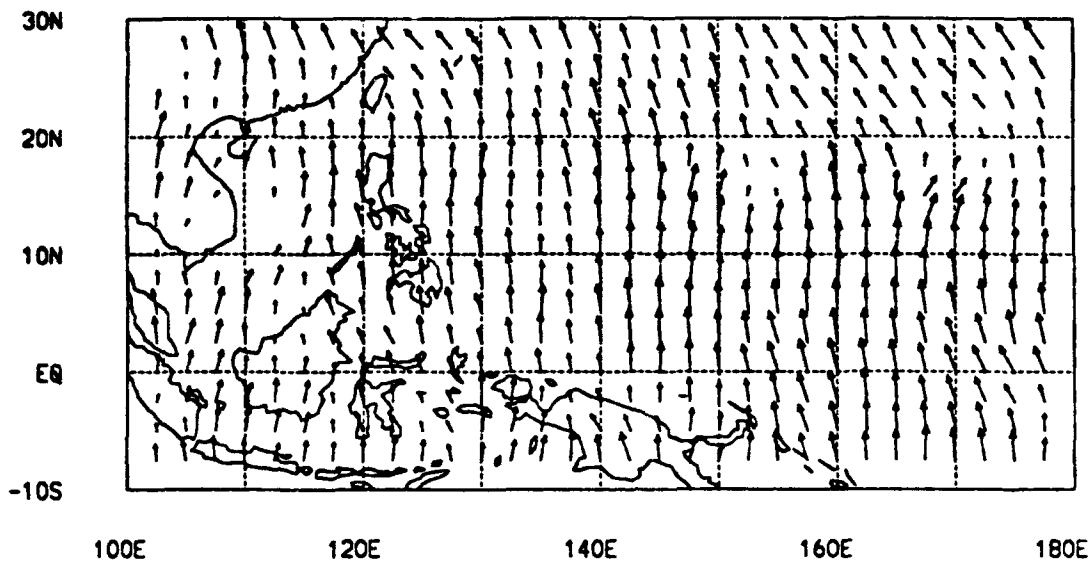
Fig. 34. Inter-latitude cross spectra, same as Fig. 31 except for  $u_{200}$ .

(a)

COHERENCE/PHASE

850 mb v / 700 mb v tau 0

period = 5.3 days



(b)

COHERENCE/PHASE

850 mb v / 700 mb v tau 48

period = 5.3 days

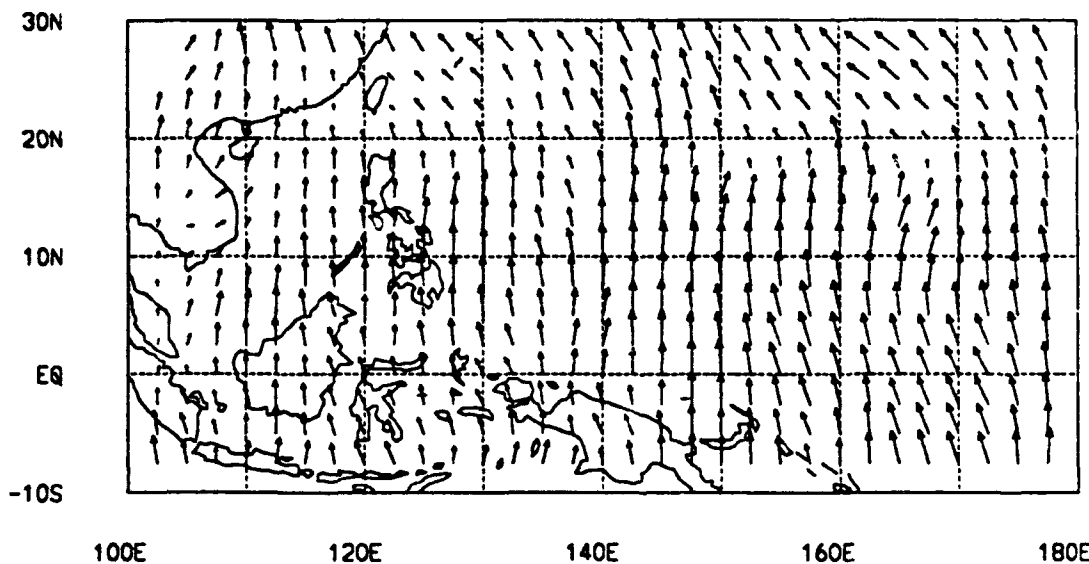


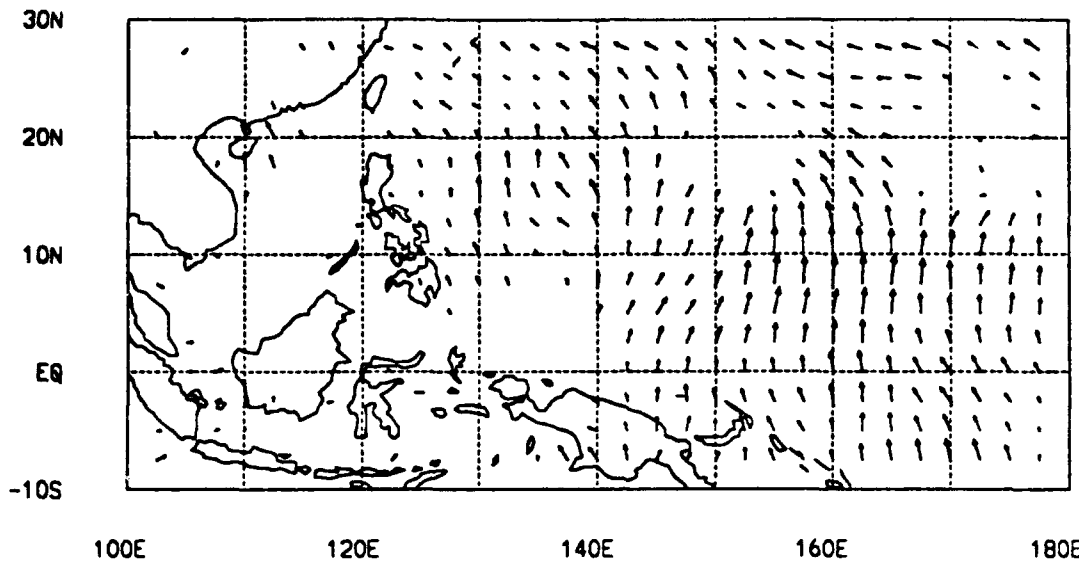
Fig. 35. Inter-level cross spectra for the synoptic band (averaged period 5.3 days) between  $v_{850}$  (base series) -  $v_{700}$ . The phase difference and coherence square between the two series at each grid point are plotted as a vector, with the direction indicating phase difference (northward pointing =  $0^\circ$ , increasing clockwise), and the magnitude indicating coherence square: a)  $\tau_{00}$ , and b)  $\tau_{48}$ .

(a)

COHERENCE/PHASE

850 mb v / 500 mb v tau 0

period = 5.3 days



(b)

COHERENCE/PHASE

850 mb v / 500 mb v tau 48

period = 5.3 days

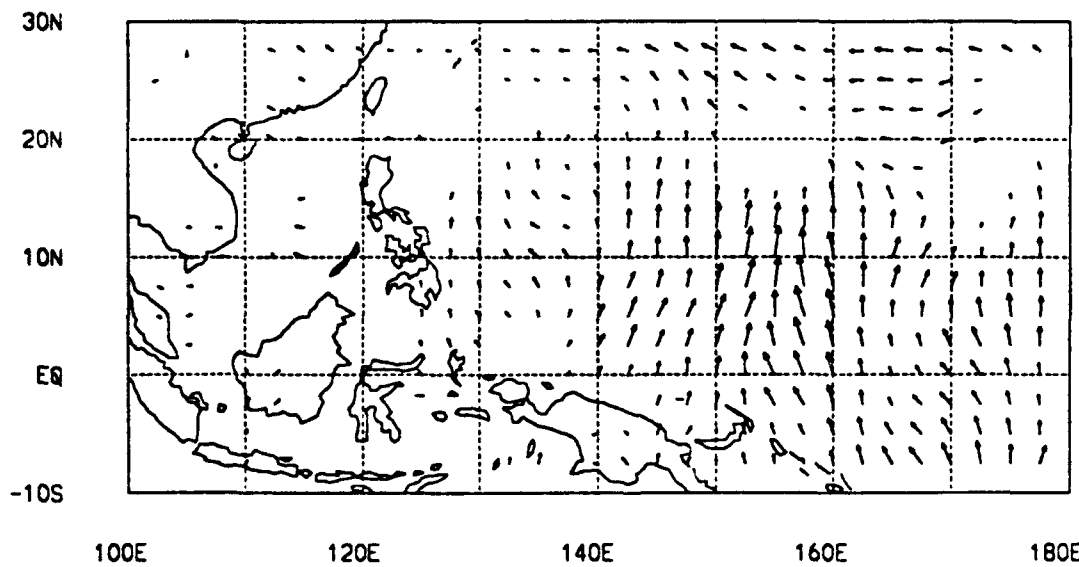


Fig. 36. Inter-level cross spectra, same as Fig. 35 except for  $v_{850} - v_{500}$ .

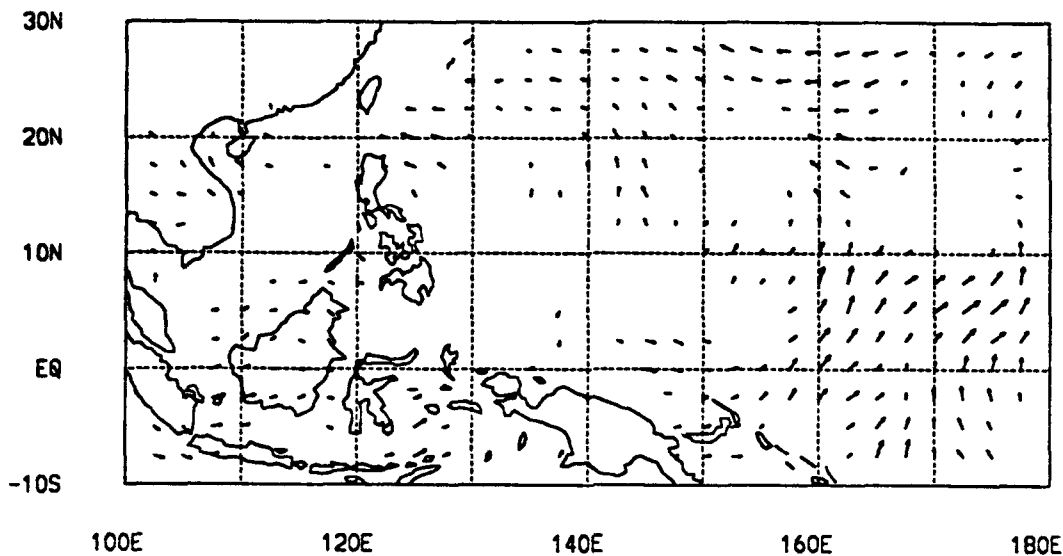


(a)

850 mb v / 300 mb v tau . 0

COHERENCE/PHASE

period = 5.3 days



(b)

850 mb v / 300 mb v tau 48

COHERENCE/PHASE

period = 5.3 days

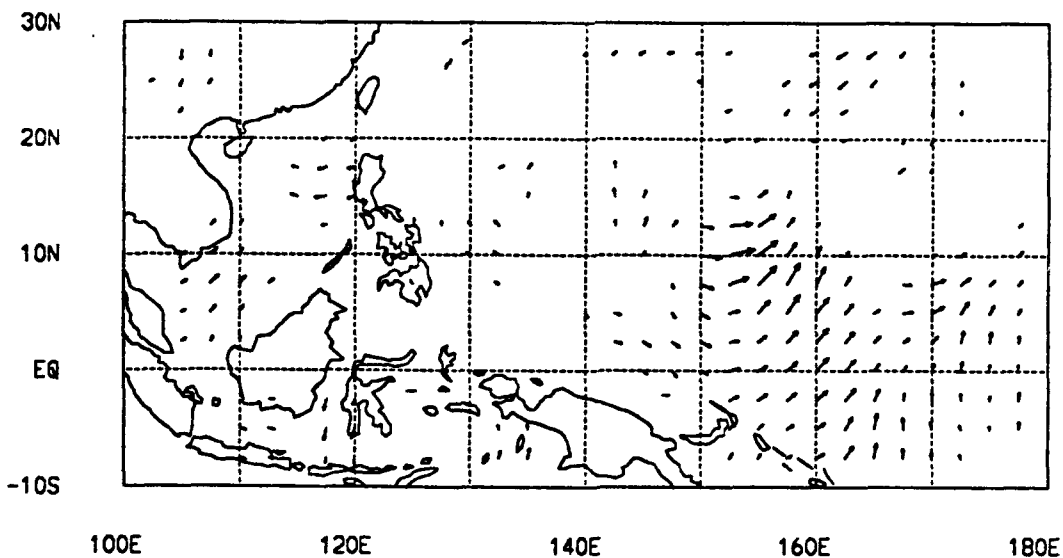
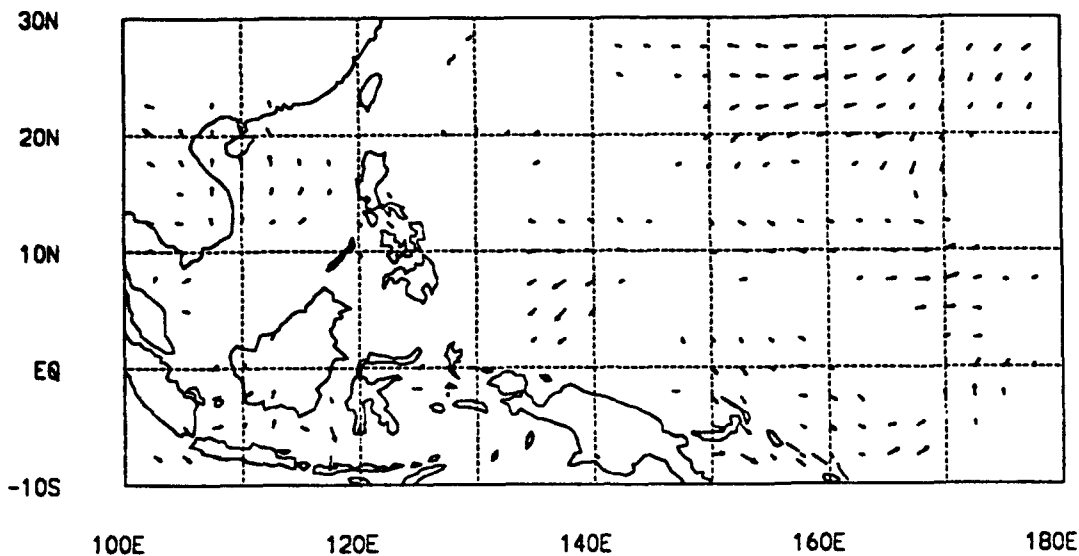


Fig. 37. Inter-level cross spectra, same as Fig. 35 except for  $v_{850} - v_{300}$ .

(a) 850 mb v / 200 mb v tau .0  
COHERENCE/PHASE period = 5.3 days



(b) 850 mb v / 200 mb v tau 48  
COHERENCE/PHASE period = 5.3 days

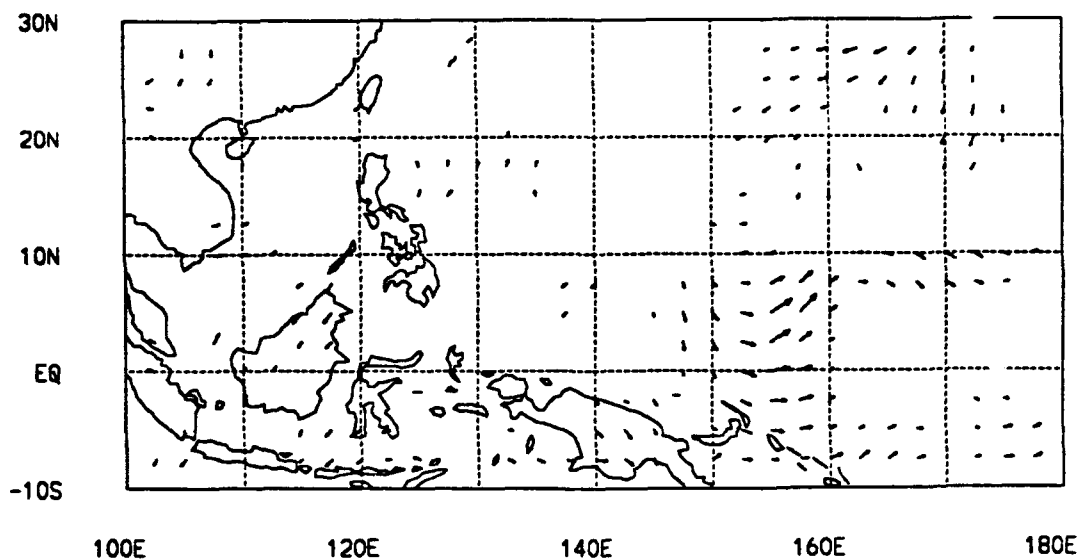


Fig. 38. Inter-level cross spectra, same as Fig. 35 except for  $v_{850} - v_{200}$ .

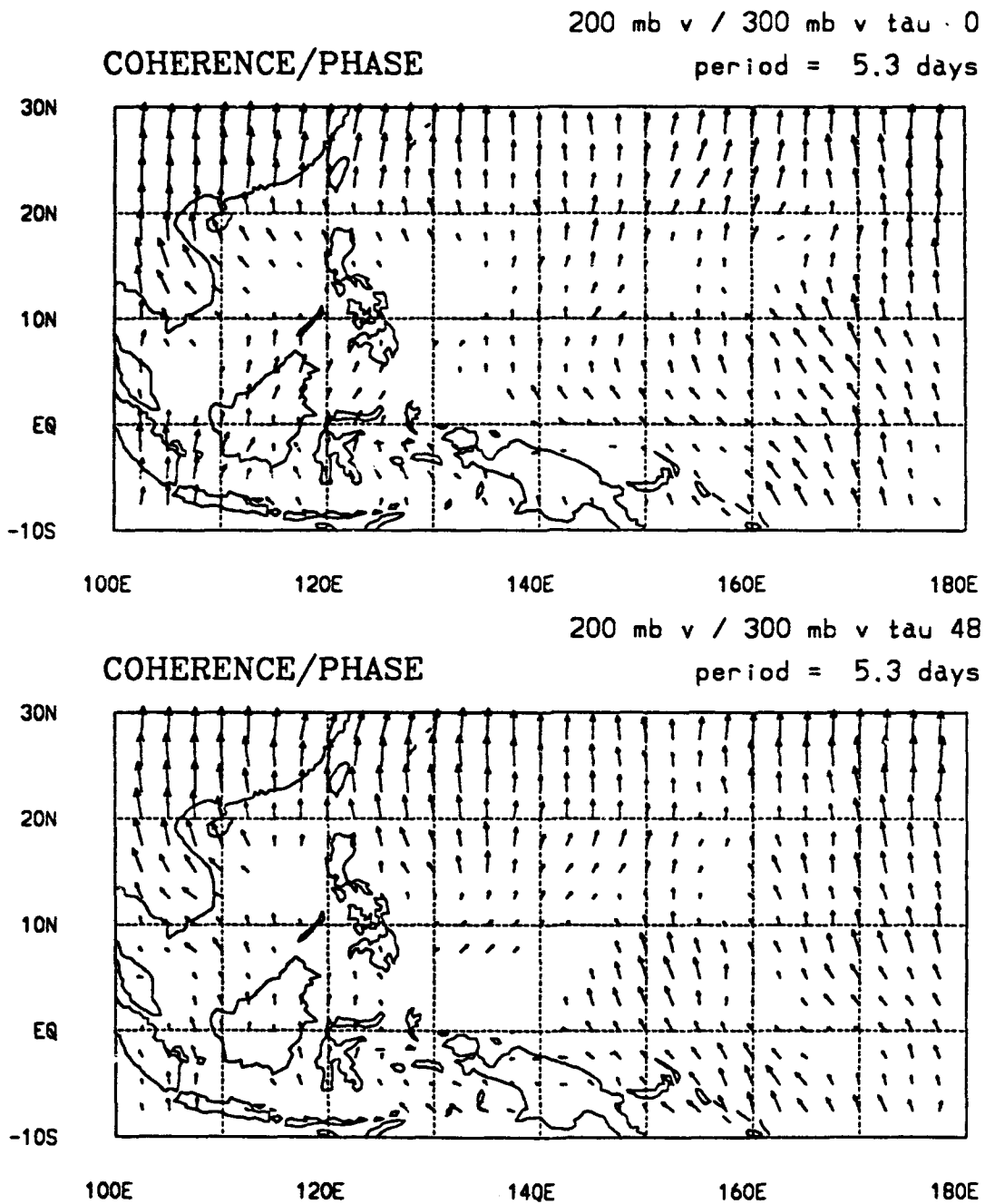


Fig. 39. Inter-level cross spectra, same as Fig. 35 except for  $v_{200}$  (base series) -  $v_{300}$ .

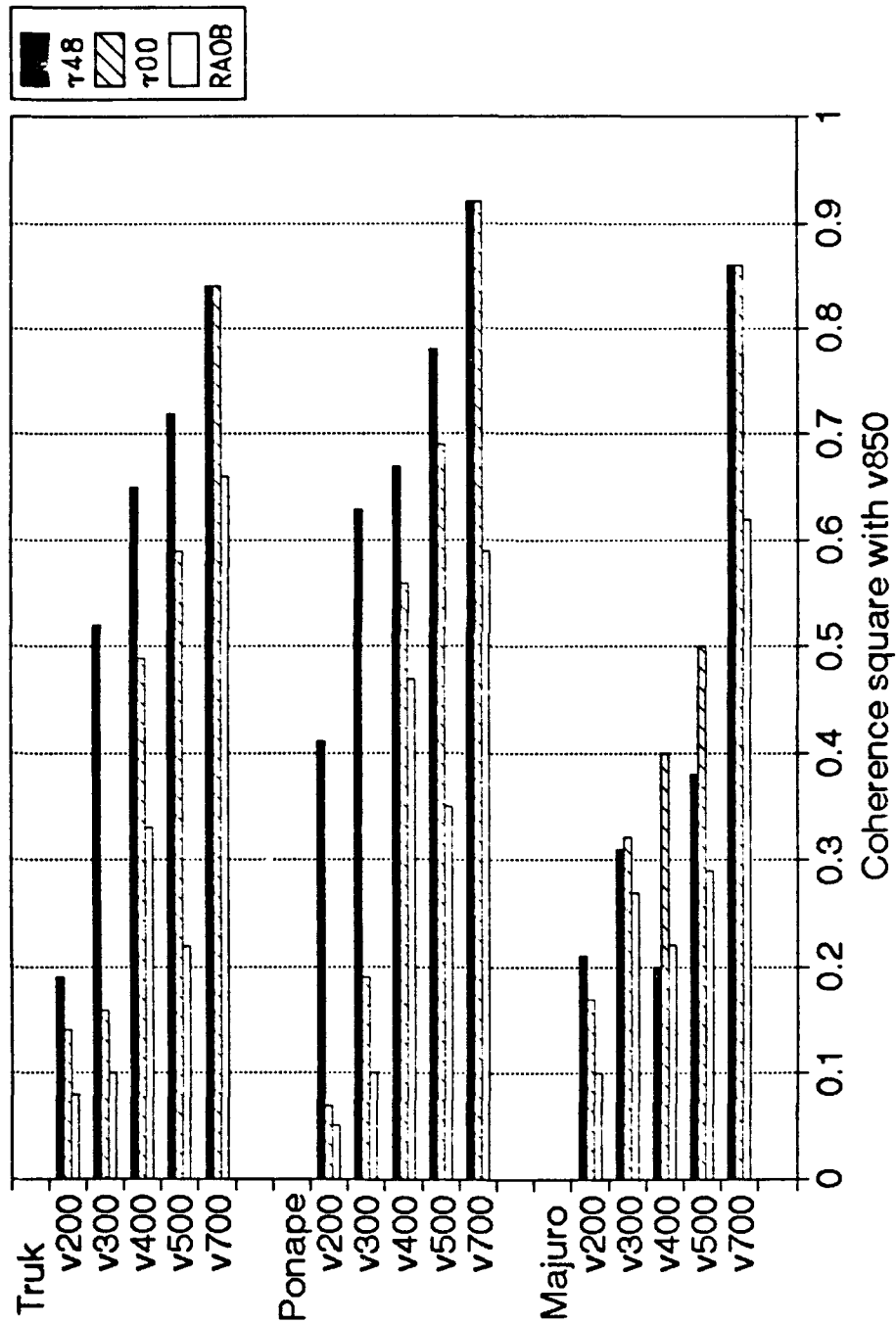


Fig. 40. Comparisons between RAOB, r00 and r48 inter-level coherence squares (v850 as the base series vs. v at other levels) for the 5.3-day synoptic band. See text for details.

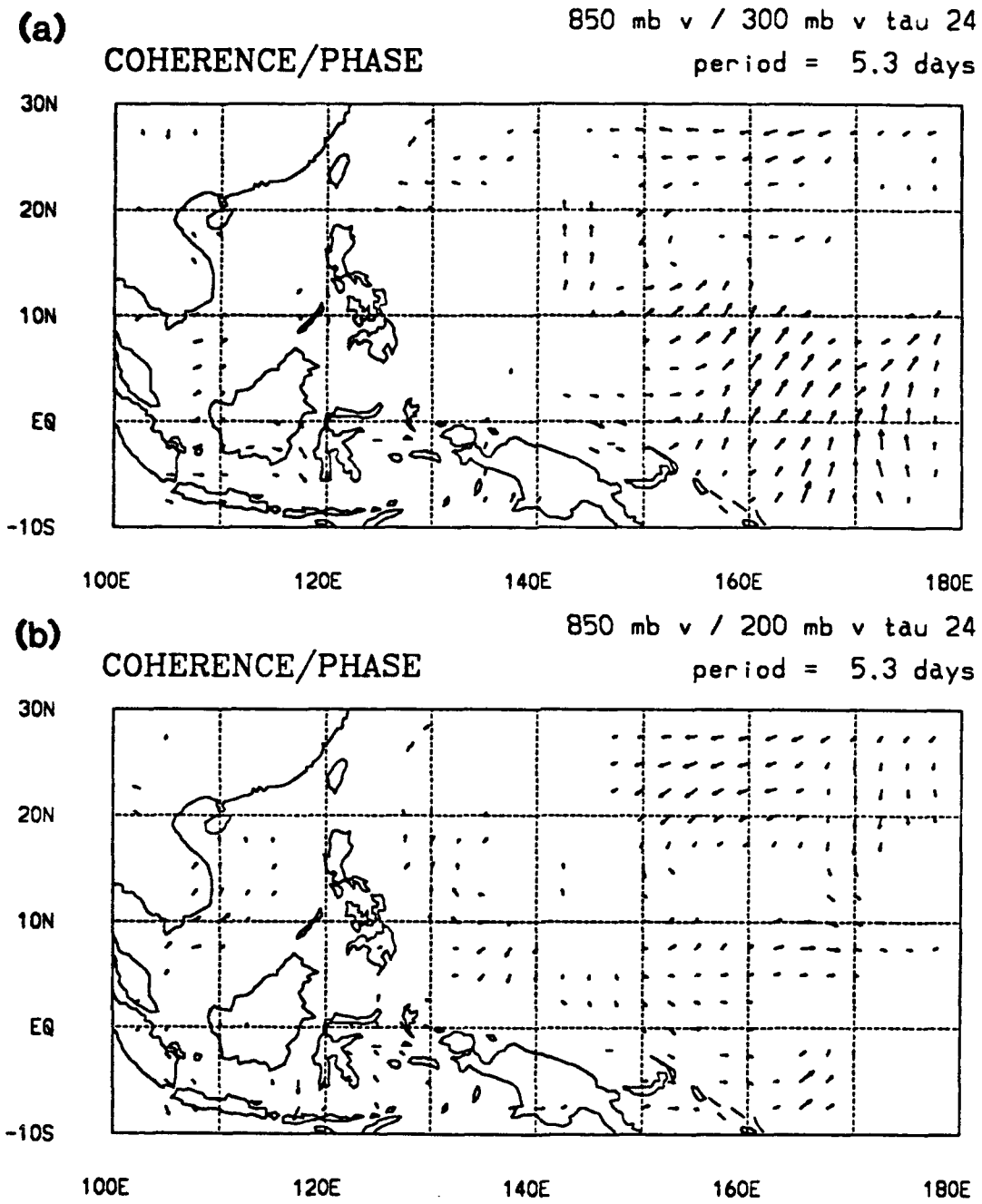


Fig. 41. Inter-level cross spectra, same as Fig. 35 except for  $\tau_{24}$ : a)  $v_{850} - v_{300}$ , and b)  $v_{850} - v_{200}$ .

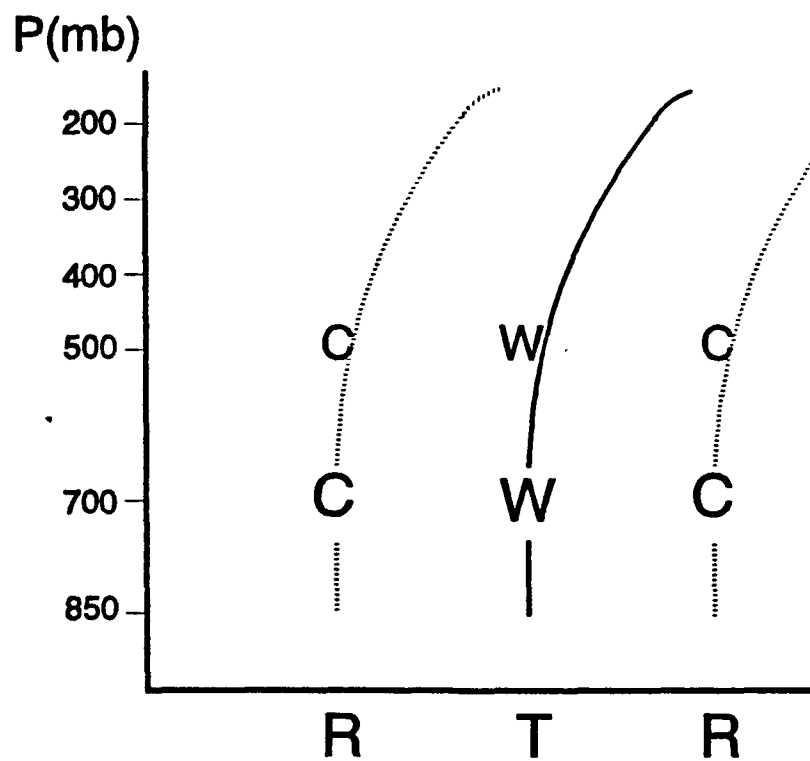
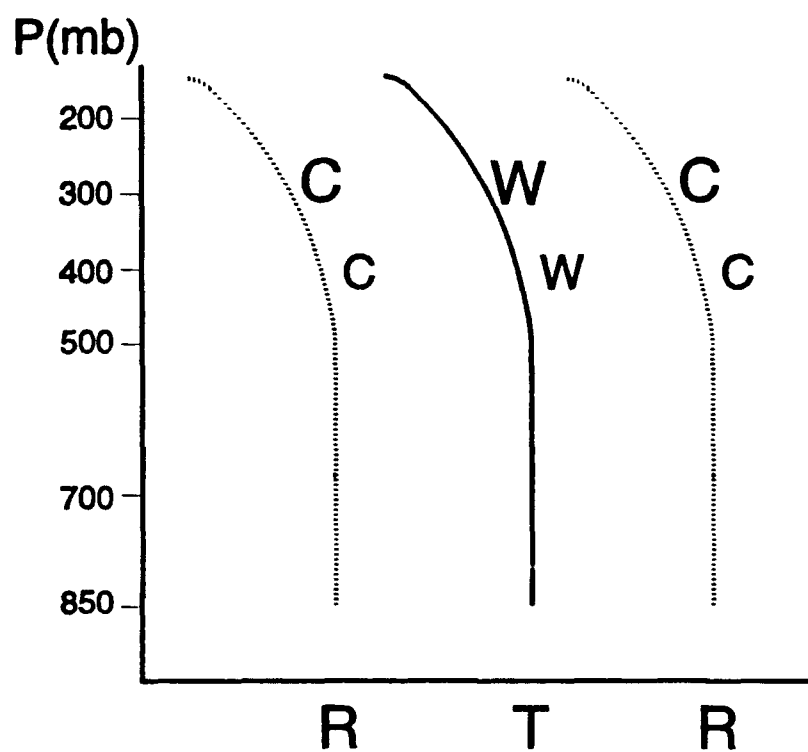
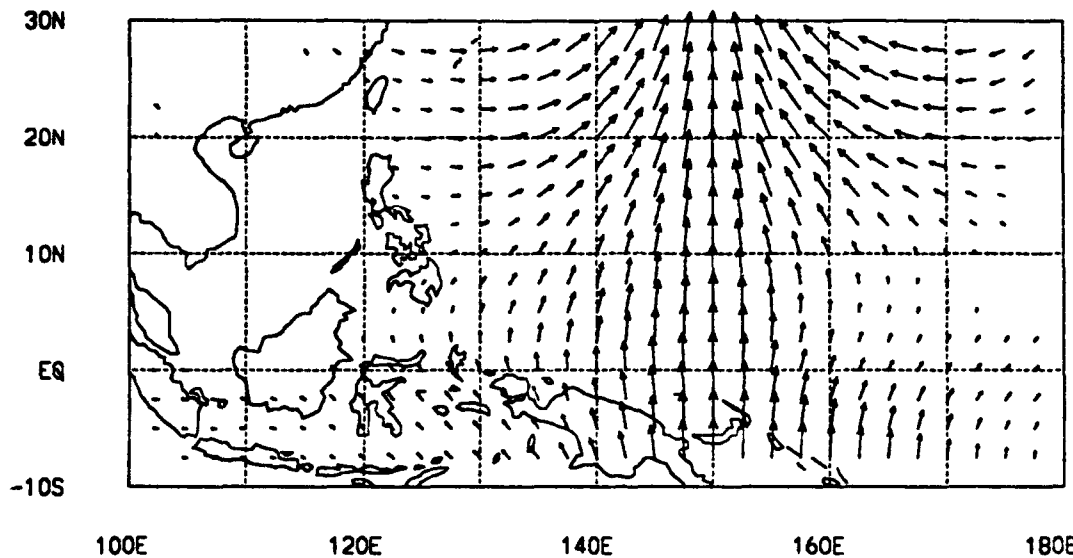


Fig. 42. Schematic diagram for the vertical structure of the 5.3-day synoptic wave at a) eastern stations: Majuro, Ponape and Truk; and b) western stations: Guam, Yap and Koror. R-ridge axis, T-trough axis, W-warm, C-cold.

(a) 850 mb x tau 0  
COHERENCE/PHASE period = 5.3 days



(b) 850 mb x tau 48  
COHERENCE/PHASE period = 5.3 days

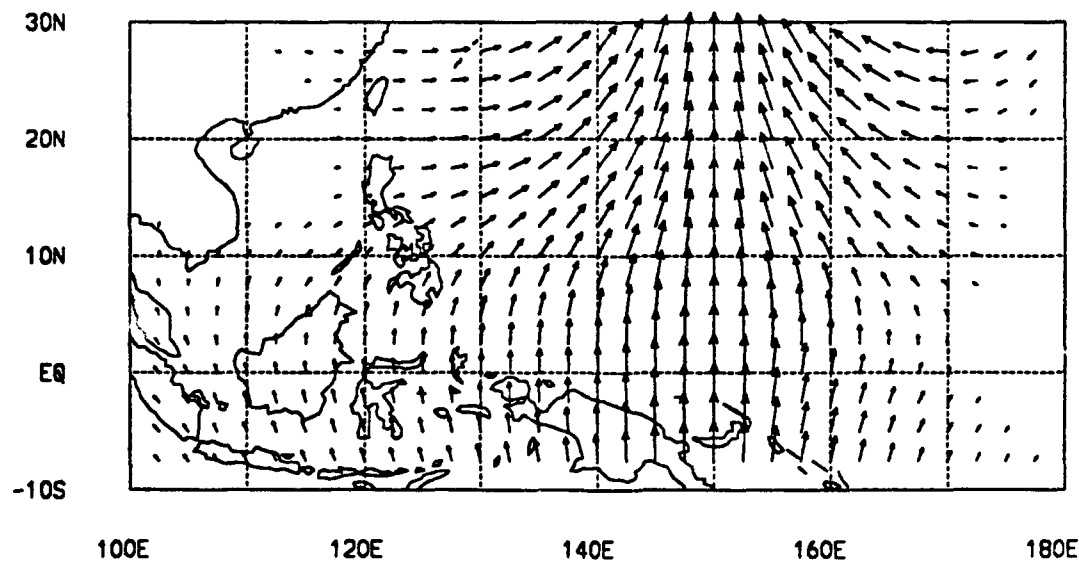
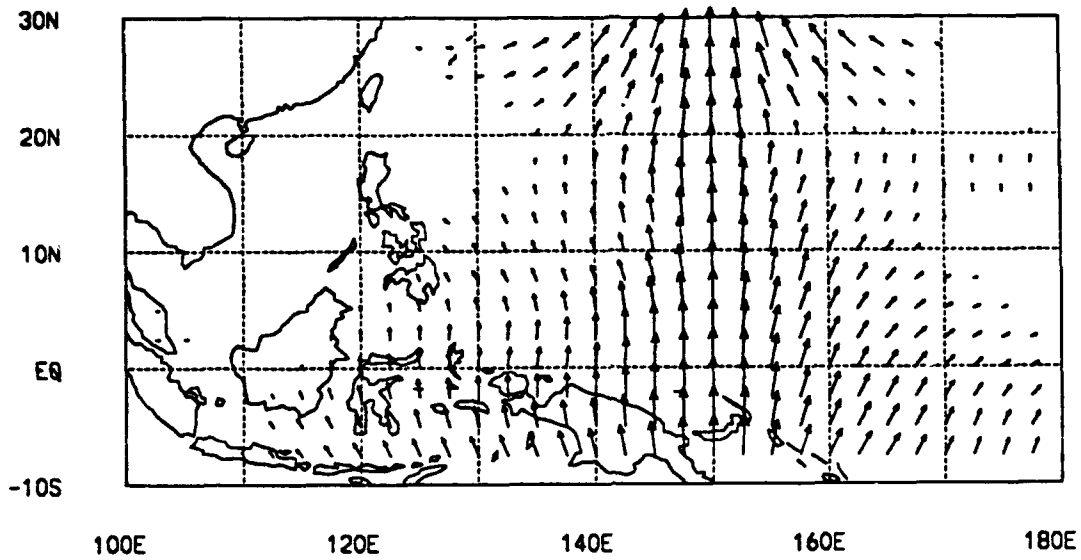


Fig. 43. Inter-longitude cross spectra, same as Fig. 27 except for the velocity potential at 850 hPa.

**(a)** COHERENCE/PHASE 200 mb x tau 0  
period = 5.3 days



**(b)** COHERENCE/PHASE 200 mb x tau 48  
period = 5.3 days

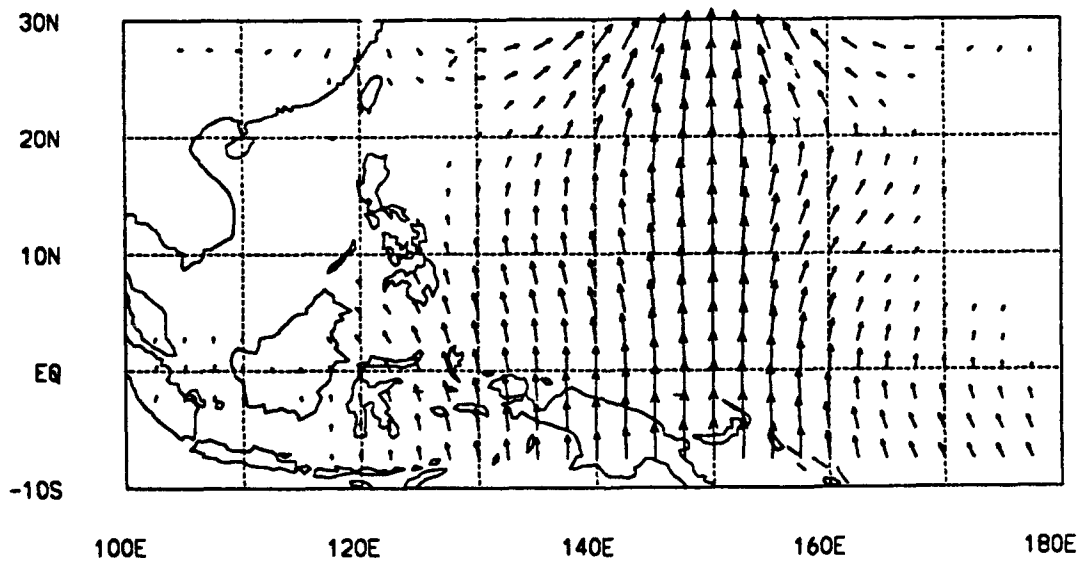


Fig. 44. Inter-longitude cross spectra, same as Fig. 27 except for the velocity potential at 200 hPa.



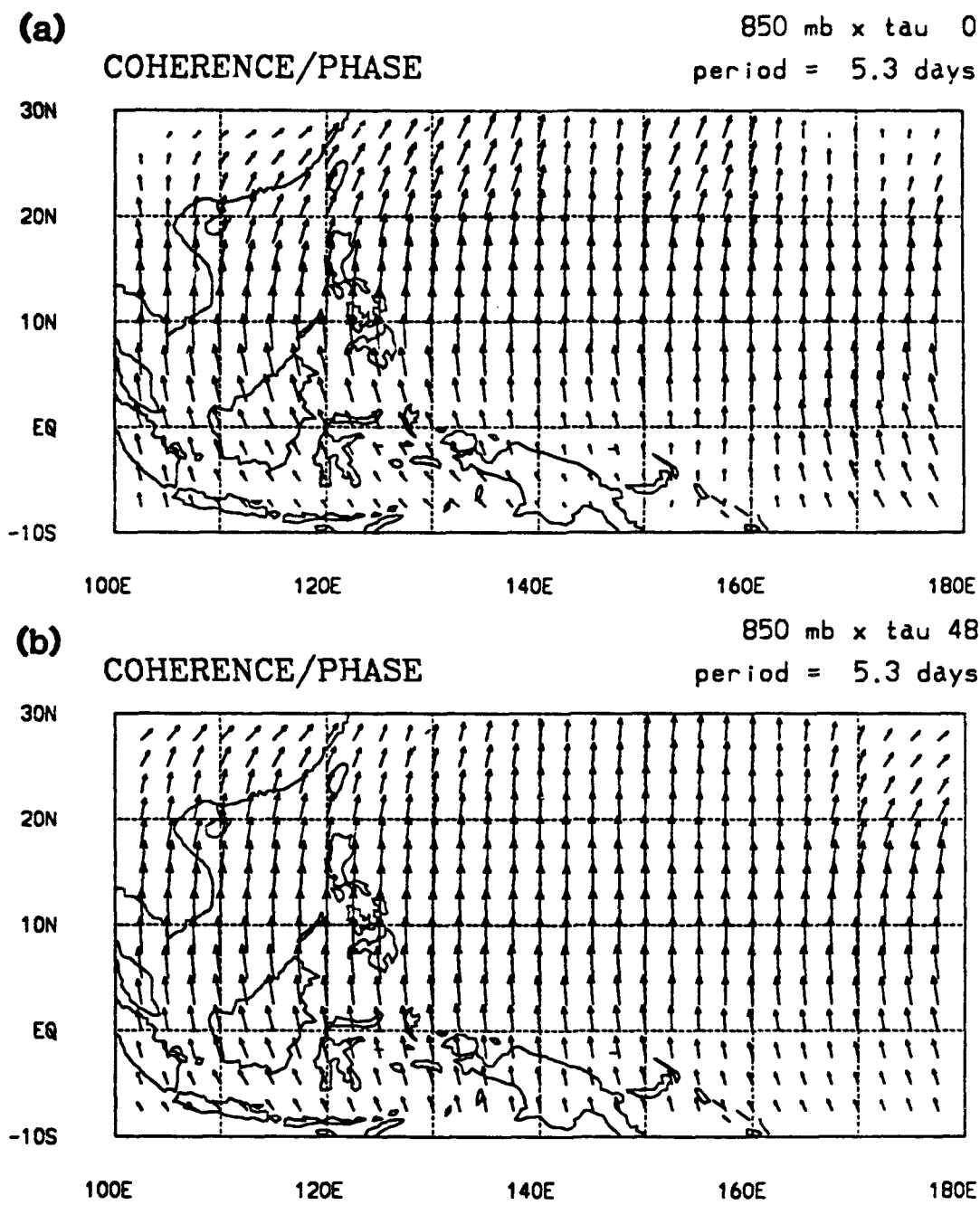
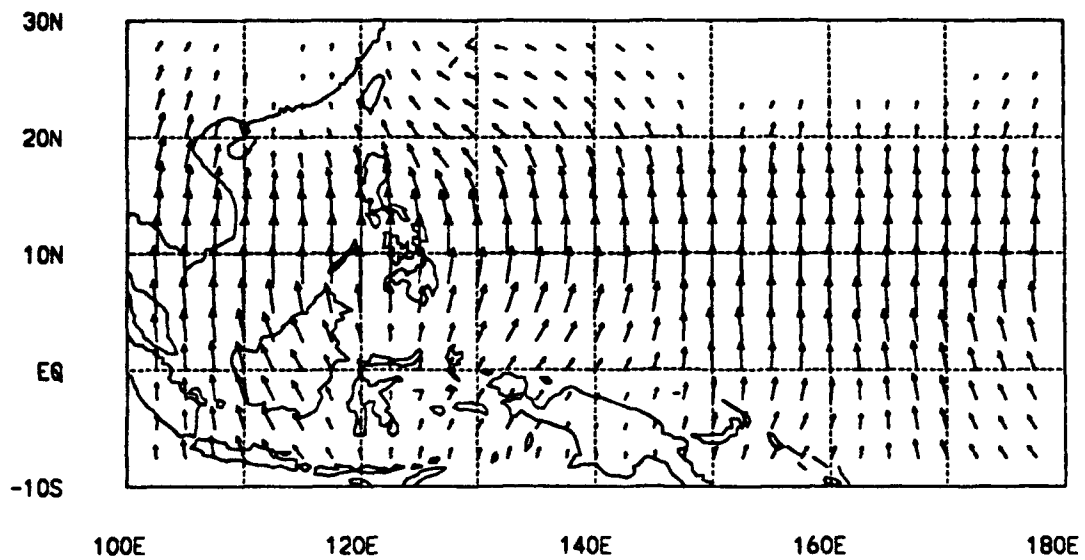


Fig. 45. Inter-latitude cross spectra, same as Fig. 31 except for the velocity potential at 850 hPa.

(a) 200 mb x tau = 0  
COHERENCE/PHASE period = 5.3 days



(b) 200 mb x tau = 48  
COHERENCE/PHASE period = 5.3 days

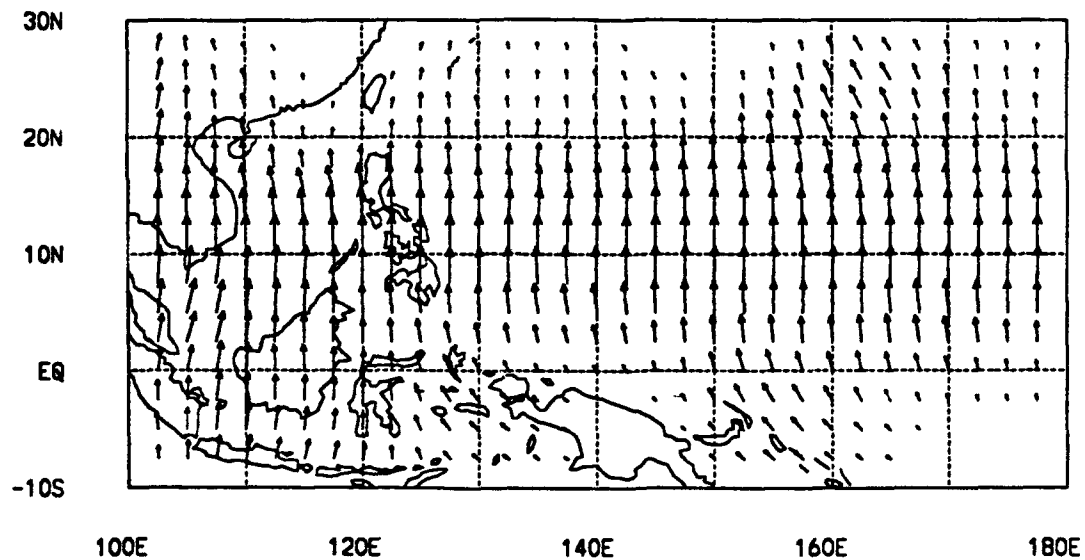


Fig. 46. Inter-latitude cross spectra, same as Fig. 31 except for the velocity potential at 200 hPa.

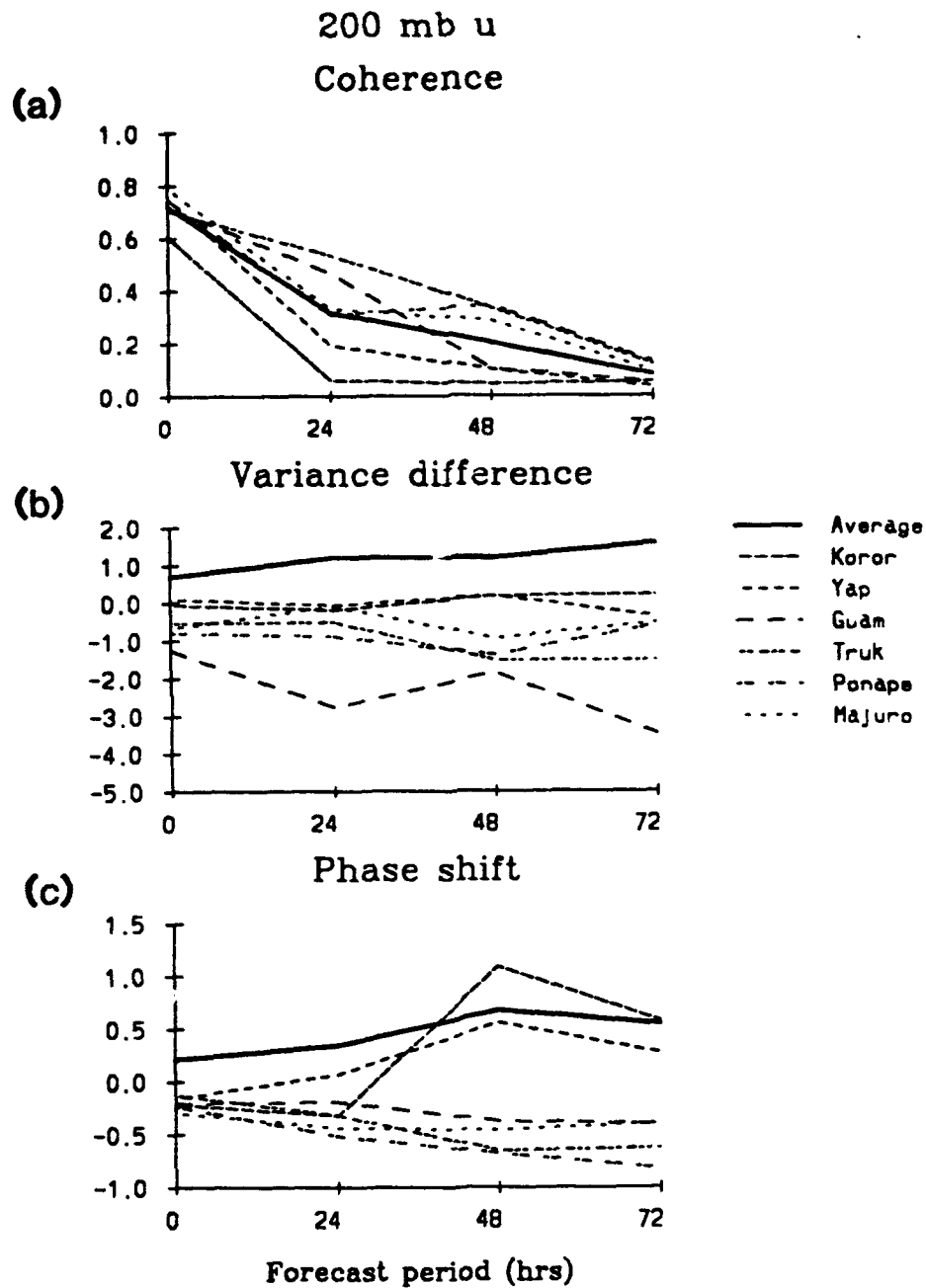


Fig. 47. The coherence square, variance difference and phase shift error scores band between RAOB and model outputs ( $\tau_{00}$ ,  $\tau_{24}$ ,  $\tau_{48}$ ,  $\tau_{72}$ ) for the 5.3-day synoptic band  $u_{200}$  at grid points closest to each of the radiosonde stations. The averages of these points are also plotted.

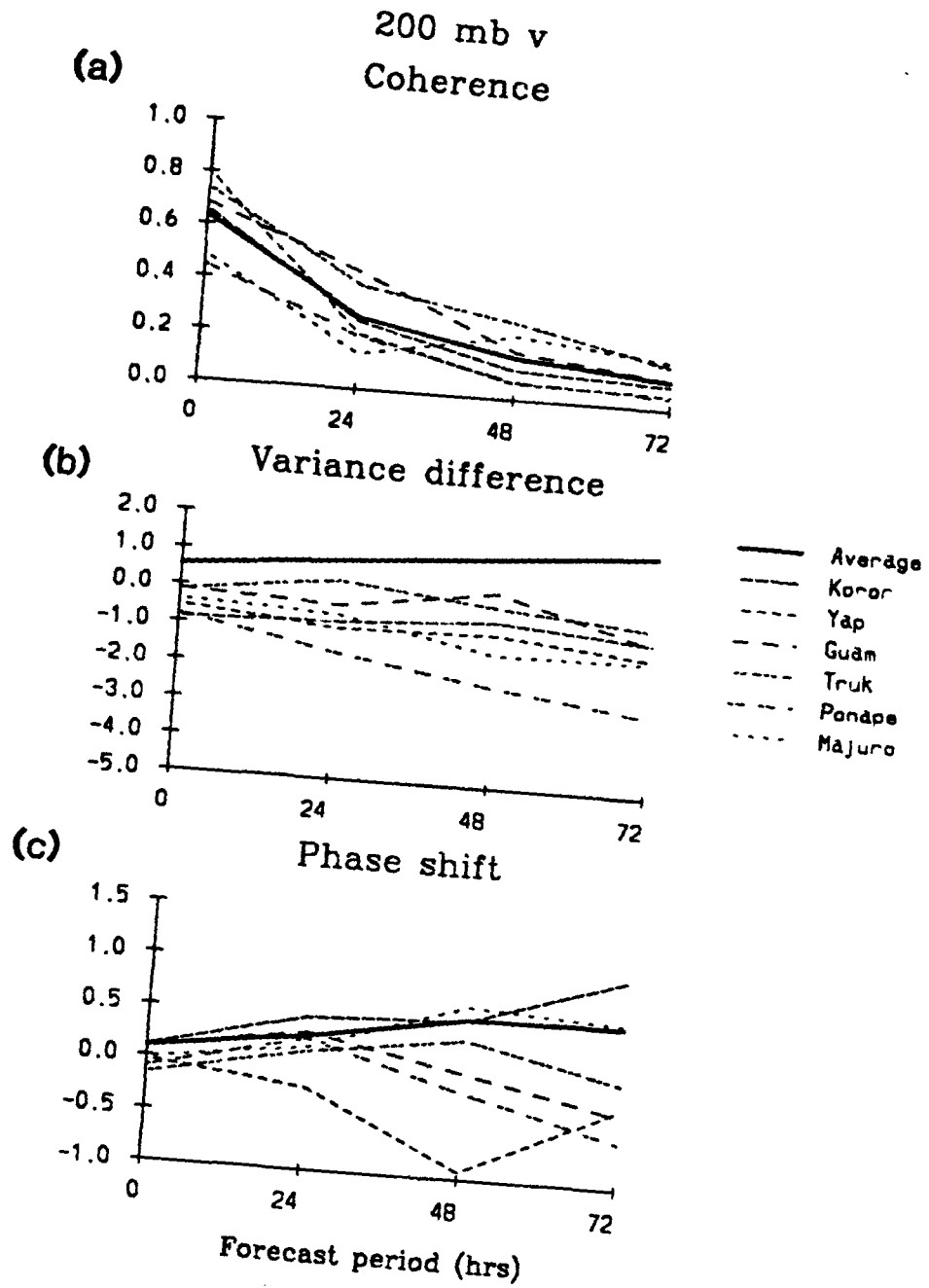


Fig. 48. Same as Fig. 47 except for v<sub>200</sub>.

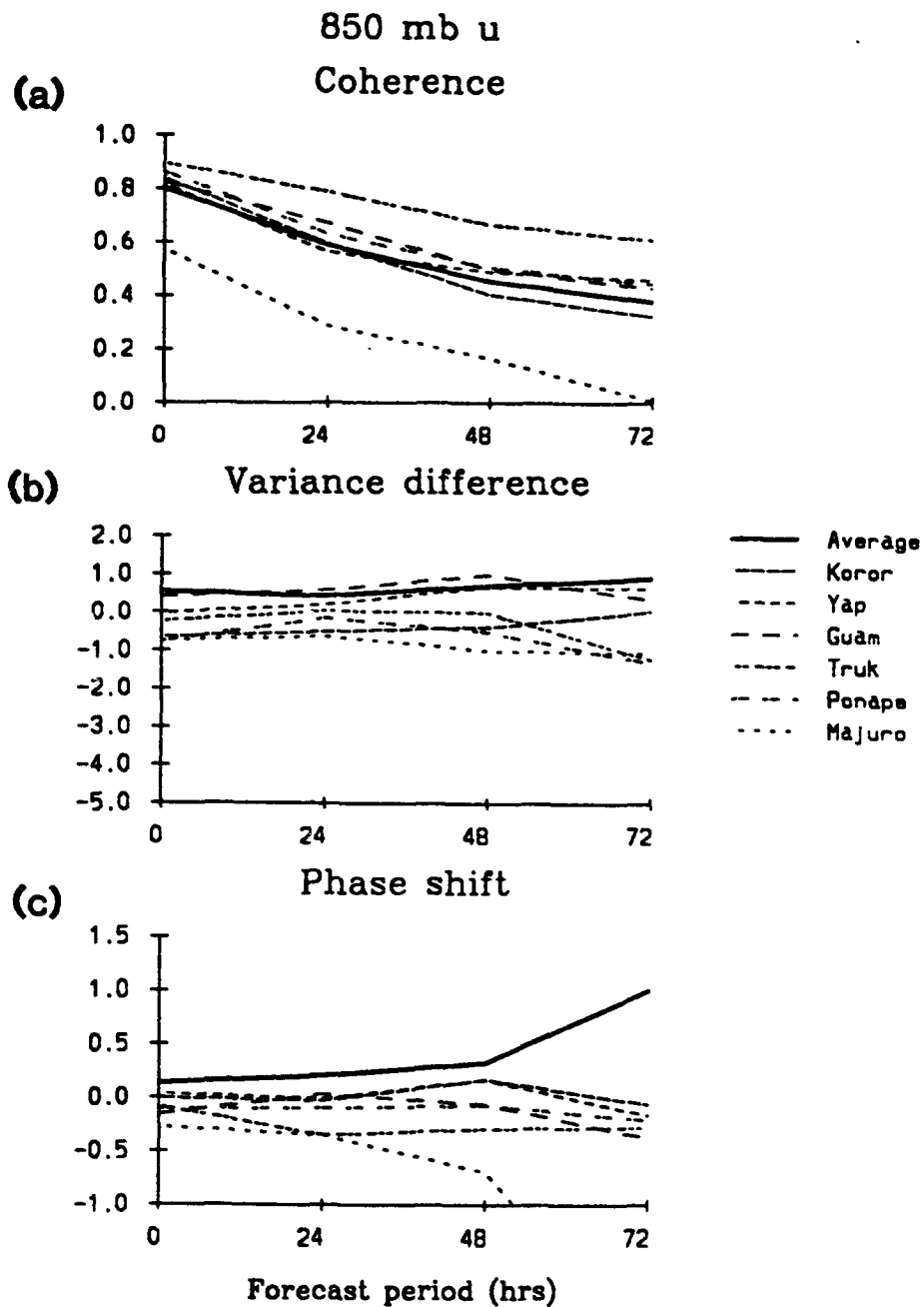


Fig. 49. Same as Fig. 47 except for  $u_{850}$ , and the averages do not include Yap.

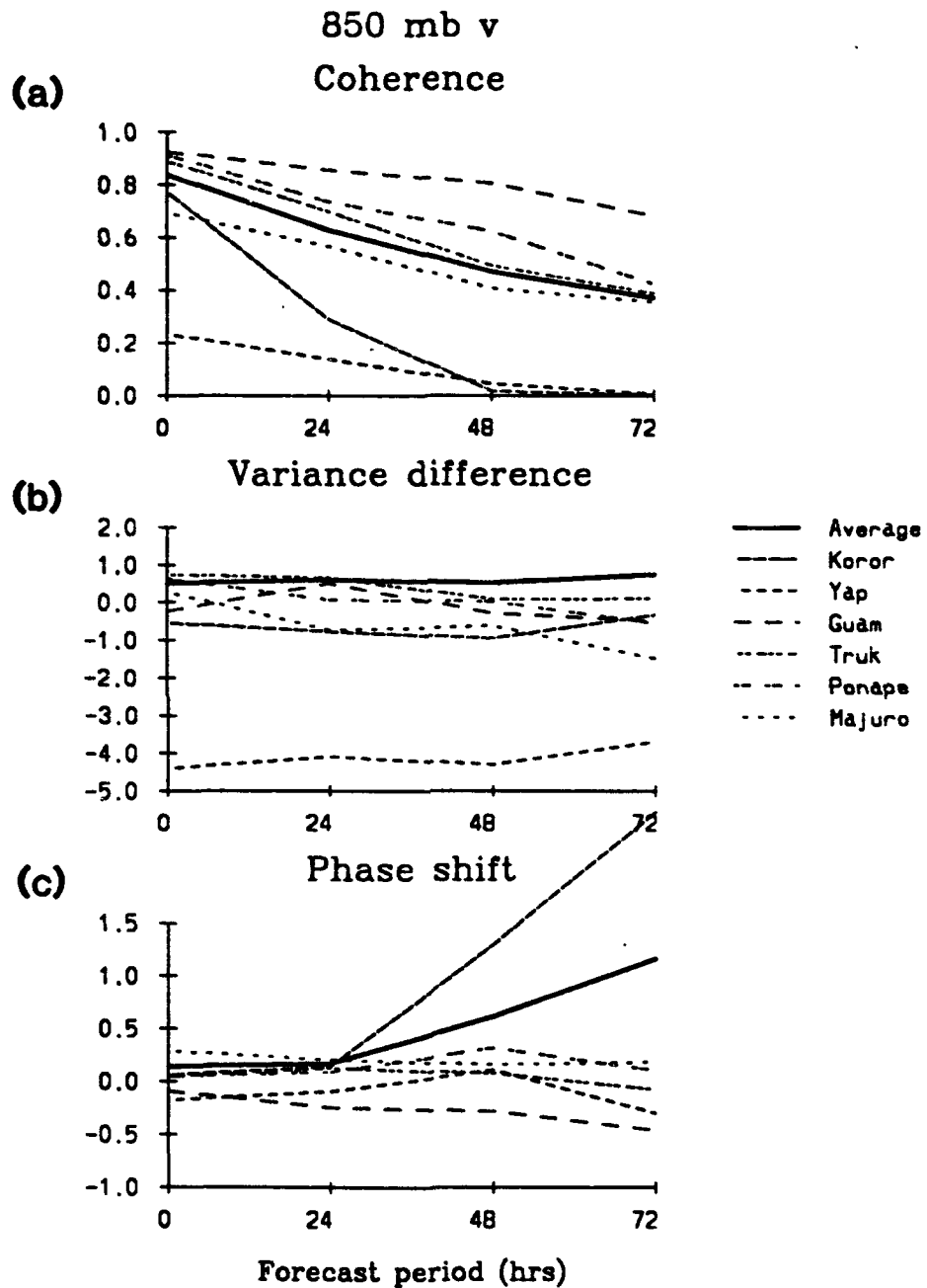


Fig. 50. Same as Fig. 47 except for  $v_{850}$ , and the averages do not include Yap.

Initial Distribution List

Dr. Ron Gelaro Division of Marine Meteorology Naval Research Laboratory Monterey, CA 93943-5502	2
Mr. Leo Clark Fleet Numerical Oceanography Center Monterey, CA 93943-5501	1
Dr. Robert Haney, Chairman Department of Meteorology Naval Postgraduate School (Code MR/Hy) Monterey, CA 93943-5000	1
Dr. C.-P. Chang Department of Meteorology Naval Postgraduate School (Code MR/Cp) Monterey, CA 93943-5000	15
Ms. Liana Zambresky Meteorological Models Division Fleet Numerical Oceanography Center Monterey, CA 93943-5501	10
Dr. John Hovermale Division of Marine Meteorology Naval Research Laboratory Monterey, CA 93943-5502	1
Commanding Officer Fleet Numerical Oceanography Center Monterey, CA 93943-5501	1
Library Department of Meteorology Naval Postgraduate School (Code 0142) Monterey, CA 93943-5000	2
Dean of Research Department of Meteorology Naval Postgraduate School (Code 08) Monterey, CA 93943-5000	1
Defense Technical Information Center Cameron Station Alexandria, VA 22304-6145	2